The Report committee for HASAN JAVED KHAN

Certifies that this is the approved version of the following report:

Improved permeability estimation of formation damage

through imaged core flooding experiments

APPROVED BY
SUPERVISING COMMITTEE:

Co-supervisor: _____

Maša Prodanović

Co-supervisor: _____

David DiCarlo

Improved permeability estimation of formation damage through imaged core flooding experiments

by

Hasan Javed Khan, BE

Report

Presented to the Faculty of the Graduate School

of the University of Texas at Austin

in Partial Fulfillment

of the Requirements

for the Degree of

Master of Science in Engineering

The University of Texas at Austin

May 2016

Dedication

To my parents, without whom nothing is possible

Acknowledgements

Abstract

Improved permeability estimation of formation damage through imaged core flooding experiments

by

Hasan Javed Khan, MSE

The University of Texas at Austin, 2016

Co-Supervisors: Maša Prodanović and David DiCarlo

The infiltration of fines into a reservoir during drilling or water reinjection and the accompanying production decline or loss of injectivity, are long-standing problems in the petroleum industry. An experimental study of suspension flow into sintered glass bead plugs has been conducted, measuring the changes in permeability and porosity over the course of injection. Glass bead suspensions of bi-disperse combinations of particle sizes, total injection concentrations and fluid flow rate are flooded through the core, while keeping the total invaded particle volume constant. The resulting changes in permeability and porosity are quantified using pressure transducers and a CT scanner, respectively. Effects of particle size, total injection concentration and fluid flow rate are discussed and conclusions are made.

Keywords: filtration; CT scan; bi-disperse particle; glass bead;

Table of Contents

Table of Figures

List of Tables

Chapter 1: Report Overview

1.1. Introduction

The infiltration of fines into a reservoir during drilling or water reinjection and the accompanying production decline or loss of injectivity, are long-standing problems in the petroleum industry. An estimated \$140 billion/year is lost by the industry due to formation damage (Byrne, 2012).

Formation damage starts from the spudding of the well, continues during completing the well and is present until production is complete. Different forms of damage are present during the lifetime of a well. Drilling mud and fines infiltration are the prominent problems during the drilling phase; completion fluid, cementation and perforation debris are concerns during the completion phase; sands and fines migration is the major cause of worry during the production phase; while wettability changes pose a danger during the Enhanced Oil Recovery (EOR) phase.

Each cause of formation damage poses a unique challenge and has to be uniquely tackled. A common problem with most of these issues is the entrainment of solids during flow in the porous media (Figure 1 - 1). This problem is common in chemical engineering and many natural science disciplines, and has been studied extensively. While we have come a long way from Iwasaki (1937), a pioneer in this field with his work related to filtration of bacteria in sand pits, a lot is still unknown.

Figure 1 - 1: Invasion of mud solids on Ketton limestone. Grain to fine ratio is 125:1. (Reproduced from Bailey et al., 1999)

1.2. Research objective

Formation damage is the impairment of reservoir rock, caused by wellbore fluids used during drilling and completions phases of a well operation, that results in a loss of permeability and porosity of the formation rock hence hindering producibility of hydrocarbons. Mechanical filtration is a subset of formation damage and is the most commonly cause of loss of production for a well.

Filtration is an old problem studied in hydrology and colloidal chemistry. Literature survey shows models and historic data readily available for mono-disperse (unimodal) injection suspensions.

Fluids in the petroleum industry, especially during the drilling phase, have a large spectrum of particle sizes included in the fluid. Mono-disperse deposition models are not the way to proceed in these cases as combination of different sizes of particles can have a significantly different effect compared to a single sized particle. The process of bridging holds more significance for these cases. Not much literature, specifically in the form of data sets, are available quantifying 3D distribution and entrapment of particles for a bi-disperse suspension. This is the gap we fill with this report.

The aim of this work is to identify and quantify the effects of different parameters controlling filtration during flow in porous media. The three parameters have been studied: particle size, fluid flow rate and total injection concentration.

An experiment is set up which measures the real-time changes is permeability and end-time changes in porosity using pressure transducers and a medical computed tomography (CT) scanner respectively. Pressure measurements gives a quantification of formation damage in different zones, while CT scanning is used to identify formation damage in different spatial locations. Multiple parameters have been varied, from concentration of injection fluid to flowrate of the fluid; and resulting changes in permeability and porosity profile are noted. Conclusions are drawn on the effect each parameter has on formation damage, and if they influence each other.

Chapter 2: Literature Review

2.1. Definition

Formation damage is defined by Bennion (1999) as "*any process that causes a reduction in the natural inherent productivity of an oil or gas producing formation, or a reduction in the injectivity of a water or gas injection well.*"

2.2. Classification of formation damage

Formation damage can be classified according to the damage mechanism causing it (Patel and Singh, 2016):

- Chemical – interactions between fluids and/or rock; changes in wettability
- Thermal – changes in temperature
- Mechanical – physical interaction of the formation and residue and/or fluid
- Biological – caused by living organisms, like bacteria

Bennion (1999) outlines the mechanisms of formation damage in order of significance (Figure 2 - 1). Bennion and Thomas (1994) summarize the seven most common mechanisms of formation damage in horizontal and vertical wells.

1. Fluid-fluid incompatibility – e.g. reaction of invaded mud filtrate with in-situ fluids
2. Rock-fluid incompatibility – e.g. clay swelling due to reaction with mud filtrate
3. Solids invasion – e.g. infiltration by solids from mud
4. Phase trapping / blocking – e.g. invasion and entrapment of high oil / water saturation in a near wellbore region
5. Chemical adsorption / wettability alteration – e.g. change of wettability due to fluid/rock interaction
6. Fines migration – e.g. sand movement
7. Biological activity – e.g. aerobic and anaerobic bacteria can be introduced by drilling whose by-products (e.g. polysaccharide polymer slimes) can occlude porosity and reduce permeability

The work presented here is focused on the formation damage caused by fines migration.
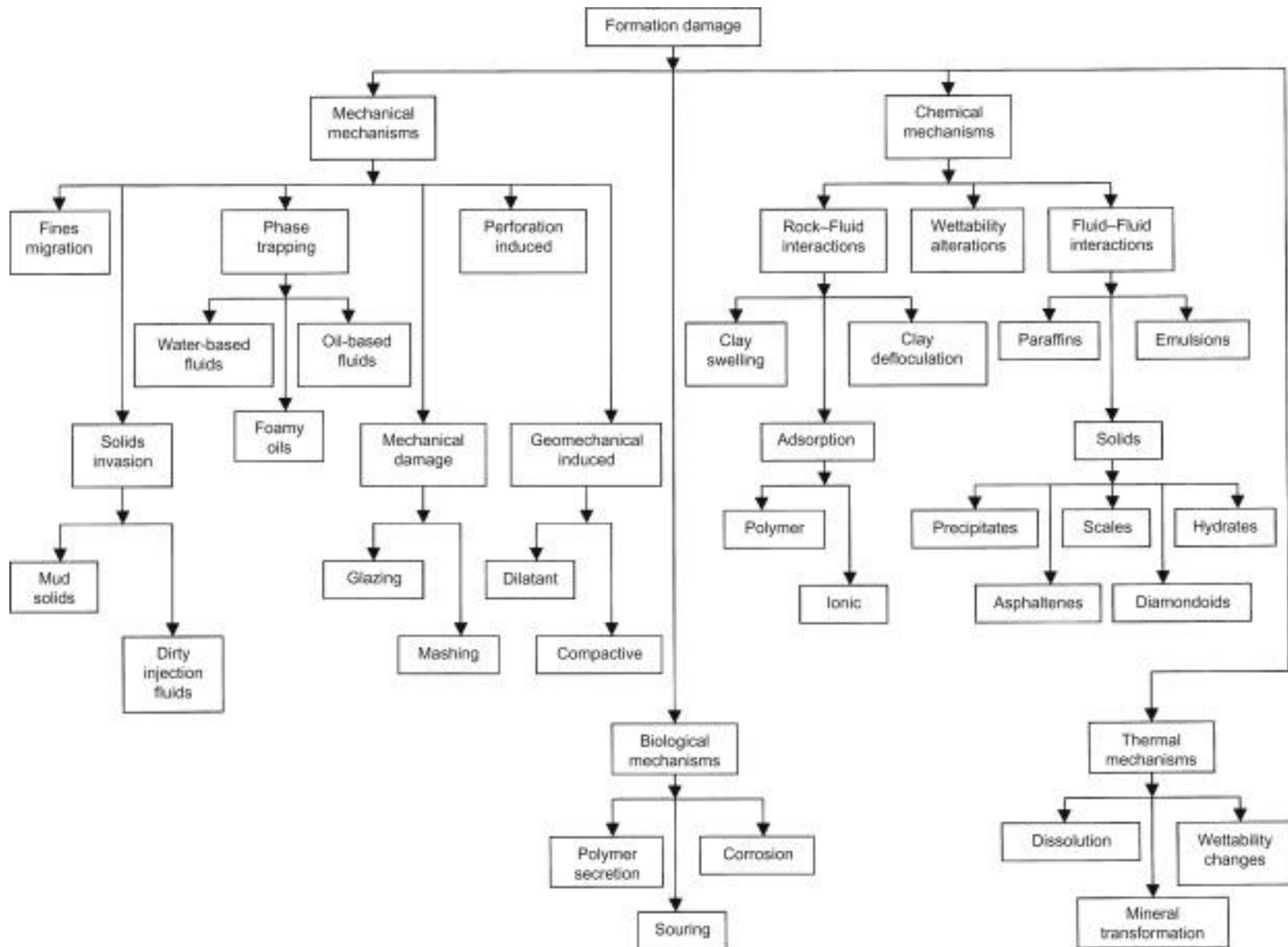
Figure 2 - 1: Formation damage mechanisms (reproduced from Bennion, 1999)

4

2.3. What are fines?

Standard fines are very small particles, usually less than 63µm in diameter as defined the ISO 14688-1:2002 standard. These are present in all naturally occurring porous materials (Gruesbeck, 1982). They can consist of many minerals in varying proportion; from silts and clays to quartz to amorphous minerals (Muecke, 1979) (Figure 2 - 2). Even though not present in high proportion, Illite and Kaolinite are the most common migrating clays (Figure 2 - 3).

2.4. Formation damage by fines migration

Formation damage is a result of forming an internal filter cake in the near wellbore region, and an external filter cake at the rock face due to fines migration or the entrapment of solids present in the drilling mud or injection fluids
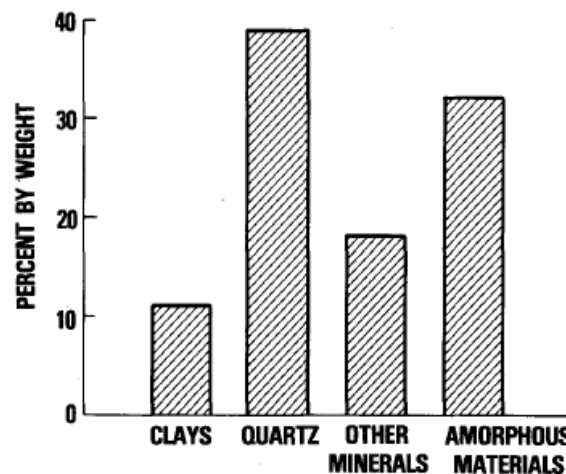
Figure 2 - 2: Average mineralogical content of fine particles present in five US Gulf coast formations (reproduced from Muecke, 1979)

Fines are colloidal size particles, and most of the historic research in the filtration has been done in hydrology and colloid transport disciplines. The first law for filtration, proposed by Iwasaki (1937), was also done in the field of hydrology where he tried to quantify rate of filtration of bacteria in a water bed. The following sections discuss the mechanisms and models for filtration, which are heavily influenced by hydrology.

5

	Well A	Well B	Well C	Well D	Well E
Clays					
Montmorillonite	5.5	13.4	2.2	1.4	—
Illite	6.2	9.1	3.0	1.7	—
Kaolinite	0.8	4.2	1.3	0.7	—
Chlorite	3.9	—	—	—	—
Quartz	36.7	24.0	47.3	17.0	68.3
Other Minerals					
Feldspar	8.6	5.7	9.1	5.4	11.4
Muscovite	1.6	—	1.6	1.0	—
Sodium chloride	1.1	1.3	7.8	5.0	1.5
Calcite	—	1.6	—	—	1.5
Dolomite	—	—	1.8	2.8	—
Barite	—	—	—	22.1	—
Amorphous Materials	35.6	40.7	25.9	42.9	17.3
Total	100.0	100.0	100.0	100.0	100.0

*Passed 400 mesh screen.

Figure 2 - 3: Results of X-ray analysis of formation fines, wt % (reproduced from Muecke, 1979)

2.5. Retention mechanisms

Herzig et al. (1970) distinguishes four retention sites: surface sites, crevice sites, constriction sites and cavern sites (Figure 2 - 4) and four retention forces: fluid pressure, surface forces, friction forces and chemical forces that contribute to retention of smaller particles. These combine to make the particle capture processes: sedimentation – gravity forces push the particle onto the filter bed; inertia – particles move away from streamlines due to weight; and direct interception – head on collision with the bed.

Surface sites.   Crevice sites.   Constriction sites.   Cavern sites.
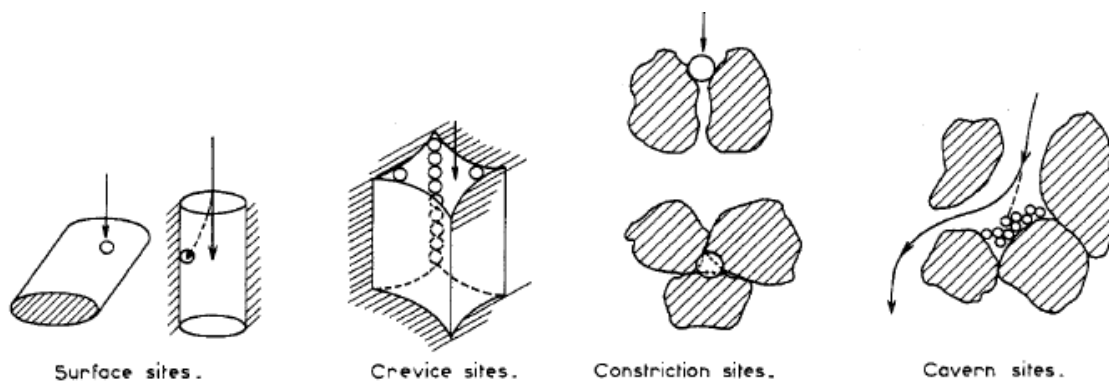
Figure 2 - 4: Retention sites (reproduced from Herzig et al., 1970)

The two most significant retention mechanisms present in the literature are described in the following sections.

2.5.1. Straining

Straining takes place by the process of size exclusion. If the size of the invading particle is larger than the size of the pore space, it gets stuck. According to Delachambre (1966), this happens in the constriction and crevice sites by the process of inertial capture and direct interception. Sakthivadivel (1966) suggests that the resulting deposits continually reduce the free passage and ultimately plug off the entry to these passages.

2.5.2. Surface deposition

Surface deposition happens when the particles get close to the surface and forces such as electrostatic and Van der Waals become significant. This happens predominantly for smaller-sized particles. Further, surface roughness is thought to contribute significantly to particle capture on the grain surface (Sharma et al., 1993). Direct interception is seen as the mode of the interaction between the smaller particles and the filter bed (Ives, 1965 & O'Melia and Stumm, 1967).
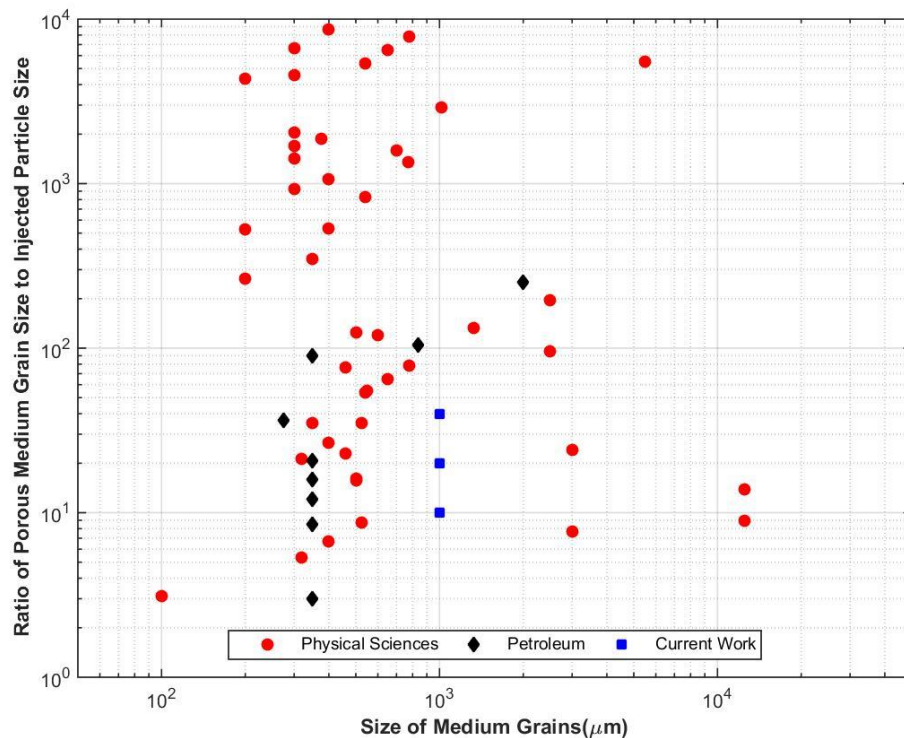
Figure 2 - 5: Comparison of experiments done in petroleum engineering and physical sciences literature (Herzig et al 1970, Gruesbeck and Collins 1982, Hertjes and Lerk 1967 & Muecke 1979). Comparison data can be found in Table A - 1.

2.6. Experiments in literature

Deep bed filtration is a long studied subject in different aspects of engineering and physical sciences. Iwasaki (1937) studied the effects of pollution in sand filter beds and the different penetration depths of suspended particle. Maroudas and Eisenklam (1965) studied the effect of dilute solutions on particle deposition in granular media.

Figure 2 - 5 shows a comparison of the size of injected particles and porous medium grains that have been referenced in the natural sciences and petroleum engineering literature (Table A - 1 in appendix). A comprehensive variety of sizes and types of injected particles and filtration medium are found throughout the literature. For example, Heertjes and Lerk (1967) used $Fe(OH)_2$ and glass spheres as the injected particle and medium, while Ives (1966) used Chlorella and sand for his experiments.

A lack of experiments in the literature can be seen towards the higher ends of sand-size grains. This study focuses on that region.

2.7. Numerical models

Historically, many models have been developed to explain the deposition mechanism. These range from the parallel pathway model, discussed by Gruesbeck and Collins (1982), to macro- and microscopic models discussed by Bailey et al. (2000) to population balance model by Sharma and Yortsos (1987). Civan (1992) has reviewed the fundamentals of the famous models present in the literature.

2.7.1. Deep bed filtration (DBF) model

Iwasaki (1937) was the pioneer in field of filtration models and suggested the following for filtration of bacteria in sand beds:

$$\lambda = \lambda_o (1 + b\sigma) \qquad \text{(Equation 2.1)}$$

where λ = filtration coefficient; b = empirical fitting parameter and σ = retention. Ives (1962) considered the tortuosity and specific surface to decrease with increasing interstitial velocity, proposing:

$$\lambda = \lambda_o \left(1 + b_1\sigma - \frac{b_1' \sigma^2}{\phi_{bed} - \sigma}\right)$$ .... (Equation 2.2)

where b_1 and b'_1 are constants.

Bailey et al. (2000) assumed the liquids and solid particles to be incompressible and suggested:

$$\frac{\delta(\phi c)}{\delta t} + u_{fluid}\frac{\delta c}{\delta z} = T_{rw}^p$$ .... (Equation 2.3a)

$$\frac{\delta \sigma}{\delta t} = T_{wr}^p$$ .... (Equation 2.3b)

where ϕ is the porosity, c is the suspension concentration, u is the fluid velocity, T_{rw}^p is the rate of transfer of particles from the rock and fluid phase and T_{wr}^p is the rate of transfer of particles from the fluid to rock phase. $T_{rw}^p = -T_{wr}^p$
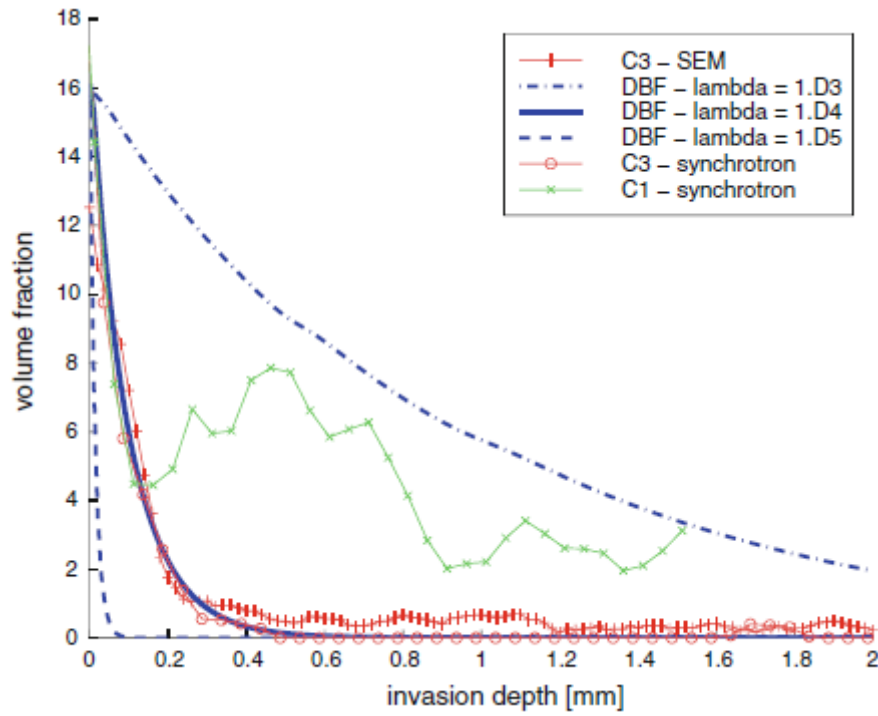
Figure 2 - 6: Comparison of synchrotron EDD-T and SEM-EDS analysis and DBF model profiling of solids invasion (Reproduced from Boek et al, 2011)

$$T_{wr}^p = u_w c \lambda F(\sigma)$$ .... (Equation 2.4a)

where λ is the filtration co-efficient and $F(\sigma)$ captures the clogging efficiency of the filter with increasing time. Bailey et al. (2000) assume it to increase linearly and propose

$$F(\sigma) = 1 + \sigma \quad \dots\dots\dots\dots\dots\dots\dots\dots\dots\dots\dots\dots\dots\dots\dots\dots\dots\dots\dots\dots \text{(Equation 2.4b)}$$

Bailey et al. (2000) and Boek et al. (2011) validated their model using core flood experiments followed by energy-dispersive x-ray diffraction tomography using a synchrotron source (synchrotron EDD-T) and scanning electron microscopy energy dispersive spectroscopy (SEM-EDS) profiling (Figure 2 - 6).

Different authors suggest different size ratio cut-offs based on their work on particle removal by straining and surface deposition. Herzig et al. (1970) claims that straining is dominant for suspended particles larger than 30 μm (particle-grain ratio of ~1:33) while Abrams (1972) and Barkman and Davidson (1979) propose that particles less than one-third and greater than one-seventh the pore diameter form internal filter cake. Van Oort et al. (1993) further modified the range to one-third to one-fourteenth of the pore diameter for low velocities (< 2 cm/min).

Based on Herzig et al. (1970) calculation that retention of particles larger than 30μm are trivially affected by electrochemical surface force, Khan et al (2016) decoupled the DBF equation for multi-modal particle injection. They assumed the retention of the large and small sized particles to be captured only by straining and surface deposition respectively and hence assumed the mechanisms to be completely independent.

2.7.2. Parallel pathway model

Gruesbeck and Collins (1982) proposed a parallel pathway model which assumes fluid pathways to have two parallel tracks. The first has a small pore size and plug-type deposits of fine occurs by size exclusion. The other track has a larger pore size and only surface deposition takes place (Figure 2 - 7). The fines are loosely deposited and can be re-entrained at a different position. Particle exchange between these pathways is not allowed and same particle concentration is assumed in both tracks.

Civan (1995) and Civan and Nguyen (2005) later modified the model and validated with experimental data from Gruesbeck and Collins (1982).
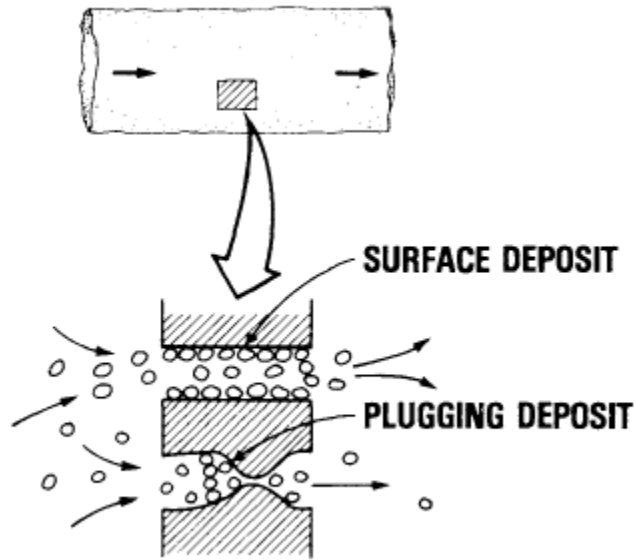
Figure 2 - 7: Parallel pathway model of fines entrainment and deposition (Reproduced from Gruesbeck and Collins, 1982)

2.8. Force analysis

Surface forces can have a significant effect on the basic physics involved. Herzig et al (1970) provide a detailed study about the significance of different forces.

2.8.1. Inertial forces

These are the forces that resist a change in velocity. The centrifugal inertial force which moves the particles away from the streamline is:

$$F_{inertial} = \pi \frac{d^3}{3} (\rho_s - \rho_l) \frac{u^2}{\phi^2 d_g}$$ …………………………………………..……. (Equation 2.5)

where d is the particle diameter, ρ_s is the solid density, ρ_l is the fluid density, u is the fluid velocity, ϕ is the grain bed porosity and d_g is the grain diameter.
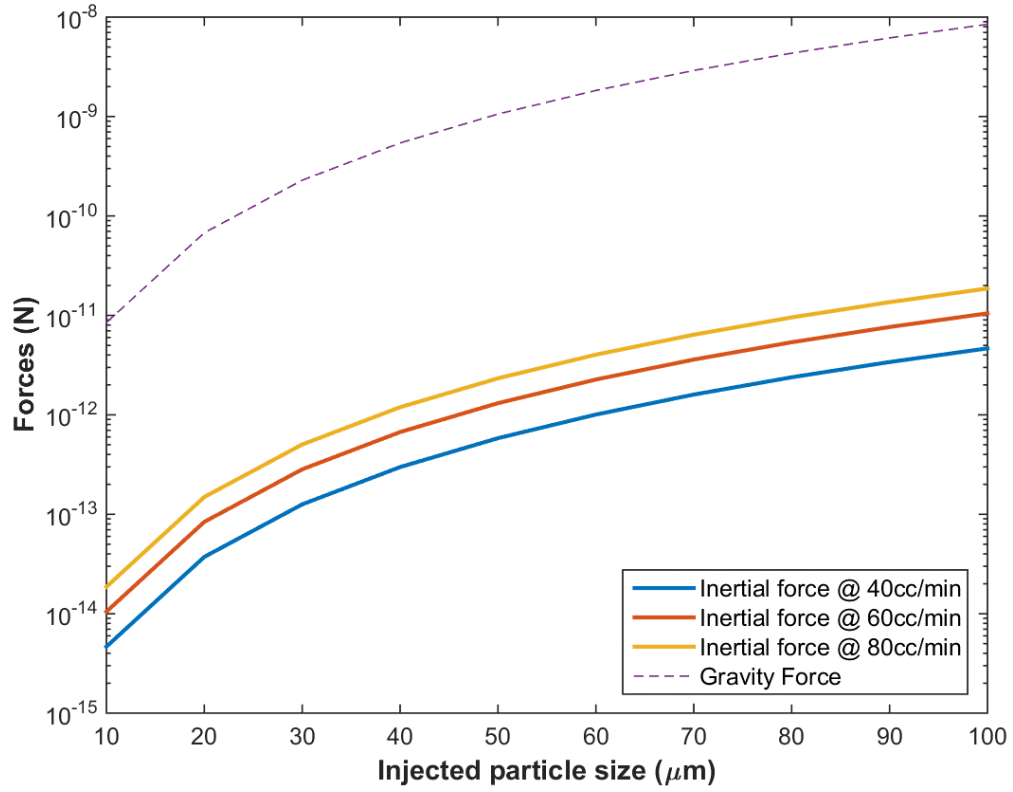
Figure 2 - 8: Comparison of inertial and gravity forces
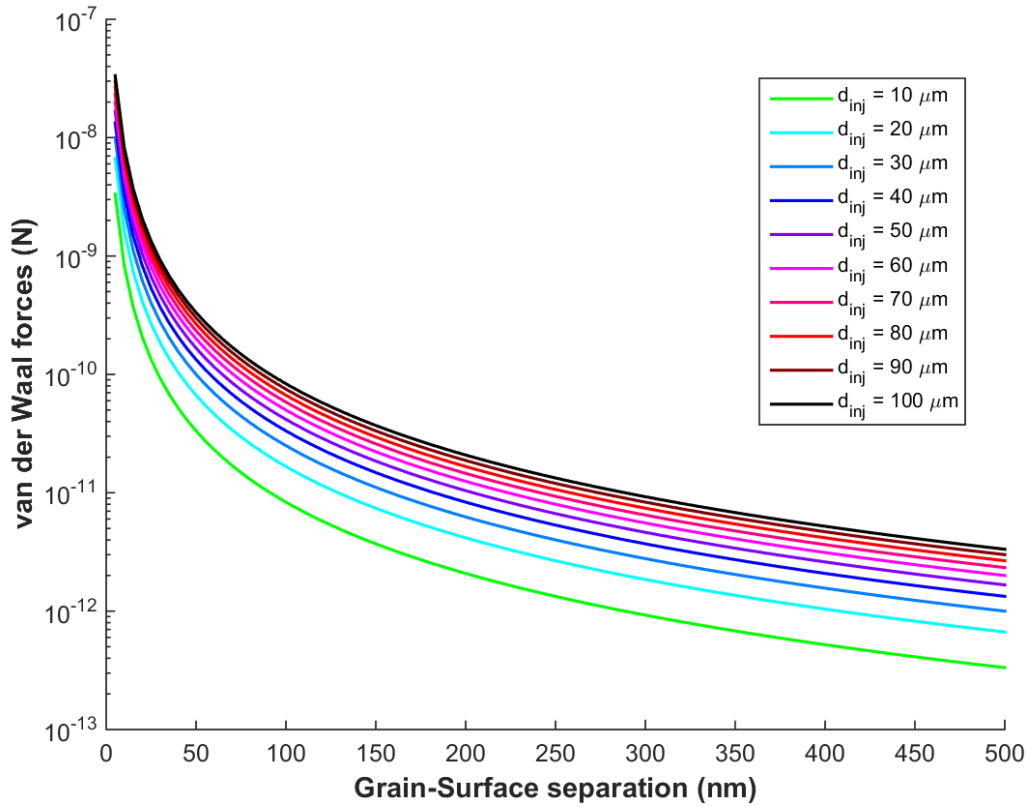
Figure 2 - 9: van der Waals force for 10 - 100 micron injected grain and 1 - 500 nm grain-surface separation

2.8.2. Gravity forces

It is the force that pulls the particles towards the earth due to the gravity force. It is defined as:

$$F_{gravity} = \frac{\pi d^3}{6} (\rho_s - \rho_l) \, g \quad \text{... (Equation 2.6)}$$

where g is gravitational acceleration and d is the diameter of the suspended particles.

Figure 2 - 8 shows a comparison of the gravity and inertial forces over the injected size of particles. The inertial force is consistently 2 to 3 orders of magnitude smaller than the gravity force, hence would not play an important role in the filtration.

2.8.3. van der Waals forces

Van der Waals forces are the weak attractive forces that are present near the surface of the particle. These can be quantified by:

$$F_g = \frac{h_H d}{12 r^2} \quad \text{... (Equation 2.7)}$$

Figure 2 - 9 shows the van der Waals forces for the injected size range from 10 to 100 microns and from a few nanometers to half a micron. It can be observed that the van der Waals force drops drastically after the first few nanometers.

Figure 2 - 10 shows the grain-surface separation required for the van der Waals force to be equal to the gravity forces. From the two figures it can be deduced that gravity plays a prominent role when the particle size is larger (on the order of tens of microns) while van der Waals surface play a prominent role in smaller sized particles.
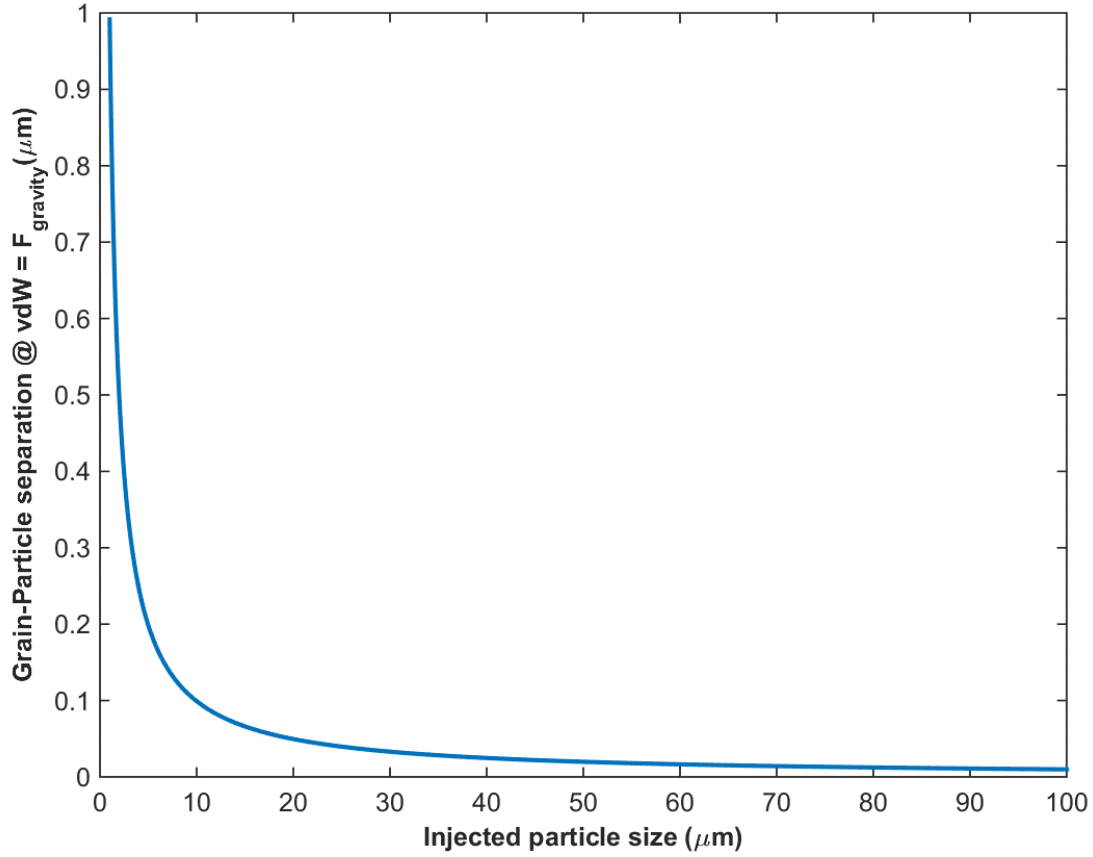
Figure 2 - 10: Grain-surface separation (in microns) when van der Waals forces are equal to gravity forces

2.9. Discussion

In the work presented here, I attempt to fill in the gaps found in the literature. The size of the grain was chosen as 1 mm, on the upper echelons of the sand sized particles, while the injecting particles were chosen as 25, 50 and 100 µm. These sizes cover the two extremes of the deposition processes as discussed in the literature, and also considers the transition zone between surface deposition and straining processes. Figure 2 - 5 shows the proposed study in comparison with the literature.

The other matter of importance was the type of materials used for the filter medium and injected phase. The literature has a wide medley of material used in experiments. These range from anthracite, sand, calcium carbonate to glass for the filter medium and $Fe(OH)_2$, algae, pollen to quartz powder for the injected phase. A few qualities that were desired in the material were:

1. Considering this work to be a stepping stone for further work on this topic, the material had to have negligible to low surface forces, so that its effect could be easily neglected during the analysis.
2. The experiments were to be repeatable and hence the material had to be such that the filter medium could be replicated with ease.
3. The injected phase had to be homogeneous and uniform in size.

Rezai et al (2014) used glass beads in their vapor extraction (VAPEX) experiments to recover bitumen from vuggy porous media. Further literature review came up with the following properties of the glass beads:

1. Low surface forces are present in glass, and hence that factor can be effectively neglected during the analysis process.
2. Glass beads have a high sphericity, hence reducing the effect of surface forces further.
3. The glass beads are mostly uniform.
4. It is easier to compare the experiments with the simulations as the pore network models can be easily established.
5. The experiments are easily replicated.

The following section discuss the literature surveyed with reference to the fabrication of glass bead cores and signal processing used for improving the quality of the pressure signal.

Chapter 3: Materials and methods

This chapter presents the details of the experimental materials and methods that are used in the study. The goal is to infiltrate bead packs with fines and measure the permeability damage using pressure measurements and porosity damage using x-ray imaging technique.

3.1. Materials

De-ionized water is used as the fluid phase for all experiments.

The glass beads used in all experiments have been manufactured by Mo-Sci Specialty Products LLC. These are solid soda lime glass beads consisting of 65-75% silica. Table 3 - 1 shows the basic physical properties of the glass bead. Detailed data sheet can be found in the Figure A - 1 in the appendix.

Table 3 - 1: Physical properties of soda-lime glass bead

Specific gravity	2.5
pH in water @ 25 °C	7.8
Softening temperature	650 °C
Refraction index	1.51

Four different sizes of glass beads have been used, which are summarized in Table 3 - 2.

Table 3 - 2: Size distribution of glass beads (Mo-Sci corporation)

Part Number	Sieve Mesh Size	Size Range (µm)	Average Size (µm)
GL0191SB/800-1200	16 – 20	800 – 1200	1000
GL0191B4/75-106	140 – 170	90 – 106	100
GL0191B4/38-53	270 – 400	38 – 53	50
GL0191B4/13-45	325 – 400	13 – 45	25

3.2. Equipment

To achieve the necessary measurements, different equipment has been used for the experiment and its analysis. These are detailed below and are all located in the Petroleum and Geosystems Engineering (PGE) department at The University of Texas at Austin.

3.2.1. Helium porosimeter

A Core Lab PORG-200 helium porosimeter (Figure 3 - 1) is available in the petrophysics lab in PGE department. This is a non-destructive method determine the porosity of a core.
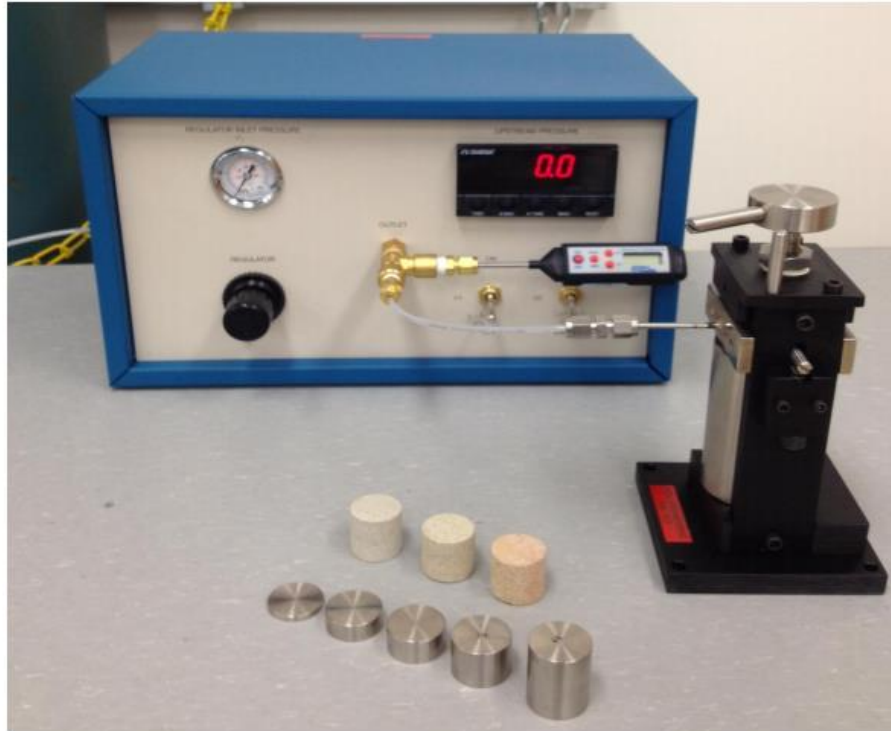
Figure 3 - 1: Core Labs PORG-200 Helium porosimeter

The core barrel is initially filled completely with the metal blanks of known dimensions. Helium is pressurized (80 psig) into a reference volume (10 cc) in the body of the terminal, which is then isolated. The mixing valve between the reference volume and the core barrel is opened allowing the gas to occupy any space left in the core barrel. System is allowed to stabilize before noting down the final pressure.

The same process is repeated by removing one blank at a time. This allows to generate a standard curve (Figure 3 - 2) which helps in removing the effect of dead volume in the experiment. The same experiment is then repeated with the core and blanks (to fill the space completely) and the pressure is noted.

A simple arithmetic calculation results in the pore volume, which can then be converted to porosity using the initial dimensions of the core.

$$V_{pore} = \frac{\frac{P_1}{P_2} - c}{m}$$ ………………………………………………………...……… (Equation 3.1)

where c is the y-intercept and m is the gradient of the standard curve.
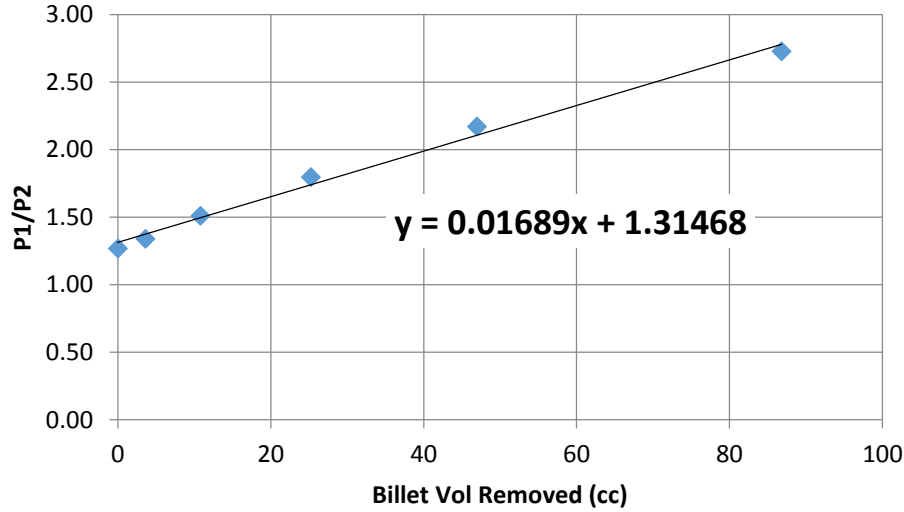
Figure 3 - 2: Sample standard curve

3.2.2. Computed Tomography (CT) imaging

An in-house multiple energy modified medical scanner from Universal Systems (Universal Systems HD-350E) is available in PGE department and was used for CT experiments. The scanner has the ability to scan in the horizontal as well as the vertical direction.

The scanner is used to measure the change in porosity of the core resulting from the core flooding experiment. An initial scan is taken with the core engulfed in deionized water. A final scan is taken after the core flooding experiment (Figure 3 - 3). The change in porosity can be calculated by a simple mixing formula:

$$\phi_{reduction} = \frac{(CT\ Number)_{after} - (CT\ Number)_{before}}{(CT\ Number)_{glass} - (CT\ Number)_{DI\ water}}$$ …………………………….….. (Equation 3.2)

The CT numbers for the fluids and glass have been measured by the author (Table 3 - 3).

Air	-1000
DI Water	25
Glass bead	2500
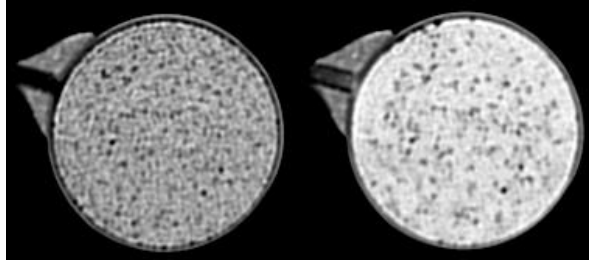
Figure 3 - 3: CT scan 6 mm from top: (left) before and (right) after core flooding

Since these CT numbers are already known and the core is initially completely flooded with deionized water, the initial scan can reinforce our value of initial porosity measured from the helium porosimeter.

3.2.3. Furnaces for sintering

Figure 3 - 4: Thermolyne FB1415M benchtop muffle furnace (present in PGE department)

The sintering was done in two different furnaces, based on the size of the core. The smaller sized cores (~3") were sintered in a Thermolyne FB1415M (Cole-Palmer) benchtop muffle furnace (Figure 3 - 4) available in PGE department. It is a manually operated digitally controlled furnace that can reach a maximum temperature of 1200 °C. The inner height of the furnace is 4.25" and hence a larger core could not be made in this.

For the larger core (~11"), a vacuum furnace, located in ETC building at UT Austin, was used from the Materials Science and Engineering department. The furnace can reach a maximum temperature of 2000 °C and take a core size of up to 12" in height.

3.2.4. Omega pressure transducer

Omega PX409 differential pressure transducers have been used in the experiment to determine the differential pressure across different points of the core. These are wet/dry transducers having a range of $0 - 1$ psi with an accuracy of 0.001 psi. The output is a voltage of $0 - 5$ Vdc which is digitized using a National Instrument DAQ-2400. The result is a voltage plot over time.

3.2.5. Flooding experiment set up

Figure 3 - 5 shows the schematics for the core flood experiments. The top most part is a fluid reservoir that contains a suspension of the injection phase glass beads in deionized water. The suspension is maintained by a Talboys Model 138 Heavy Duty mixer operating at 7000 to 8000 rpm. The propeller of the mixer is maintained a few centimeters above the base of the reservoir so that it can effectively keep all the particles in suspension.

A 1/8" OD x 3/32" ID tubing carries the suspension from the fluid reservoir to the core holder, which houses the core. Fabrication of the core holder and placing the core inside is discussed in detail in the next section.

Pressure taps are connected to the core holder which go to the pressure transducers. The pressure transducers are fixed on a mount and connected to the data acquisition (DAQ) system which is then connected to a data logger.

A Masterflex L/S 16 tubing (3.1 mm ID) goes from the core holder, through the Masterflex L/S digital drive positive displacement pump to the waste bin. This pump controls the rate of flow of

the fluid throughout the experiment. It has a flowrate dependent upon drive RPM and tubing size, and ranges from 0.001 to 3400 cc/min. Since the pump efficiency can significantly affect the outcome of the experiment, the author on multiple occasions empirically found the drive rpm for a specific flow rate.
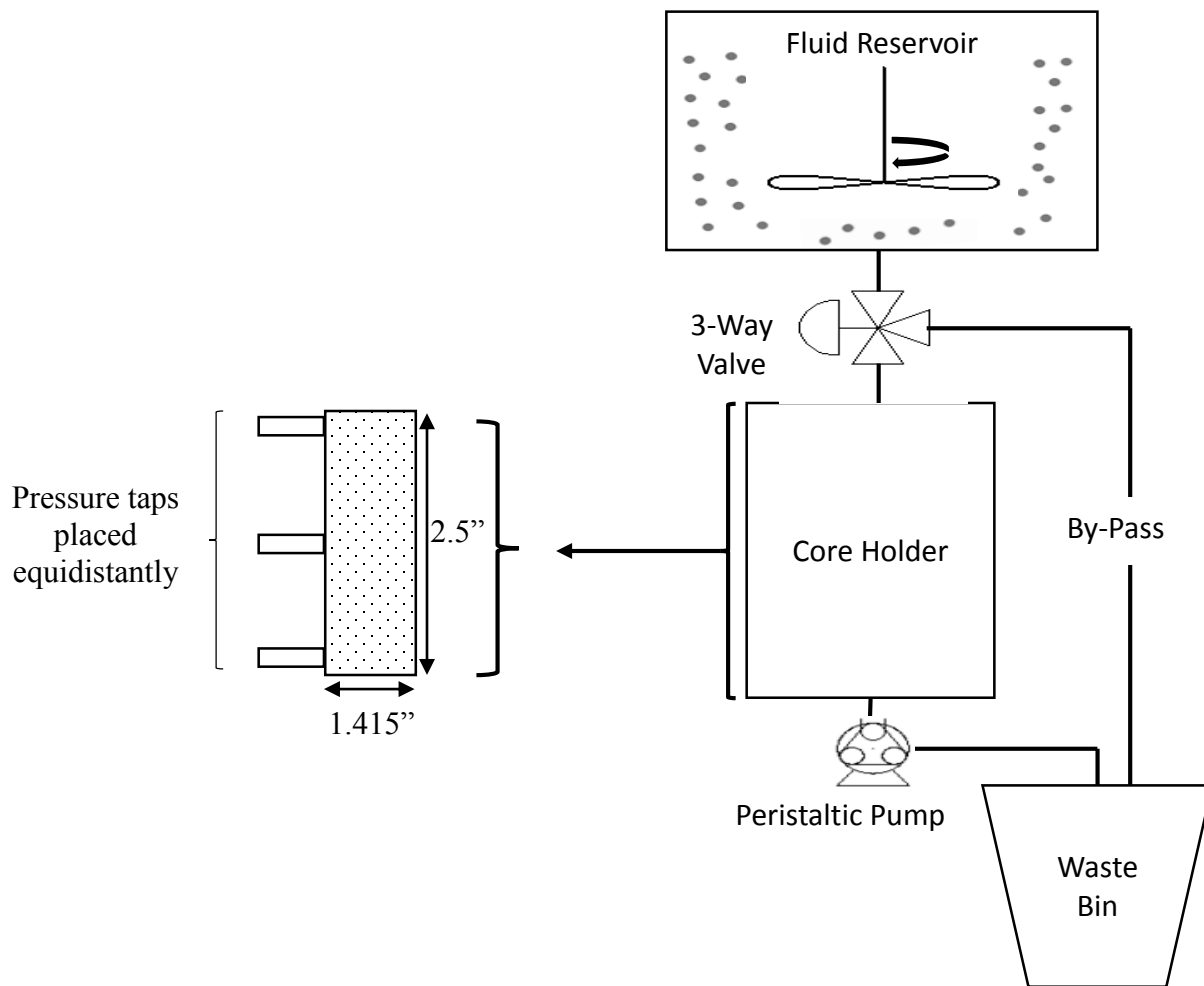
Figure 3 - 5: Core flooding experimental set up schematics

A by-pass line runs from the 3-way valve below the fluid reservoir to the waste bin. This line is used for initially flooding the core with deionized water and for flushing the lines. The 3-way valve isolates the fluid reservoir from the system and is needed when changing the core.

Figure 3 - 7 shows the experimental set up in place.

3.3. Core fabrication

3.3.1. Sintering of glass beads

Wong et al. (1984) sintered glass beads together to make artificial rock for permeability and conductivity experiments. Glass beads having average diameter of 50, 100 and 200 µm were cleaned and washed, and then exposed to different temperatures in a furnace. This yielded different porosities and permeabilities. Micrographs were taken of the sintered packs after completion. Porosity was determined by measuring the dry weight, wet weight and buoyancy in water. The accuracy of the porosity measurement was determined to be 1 porosity unit.
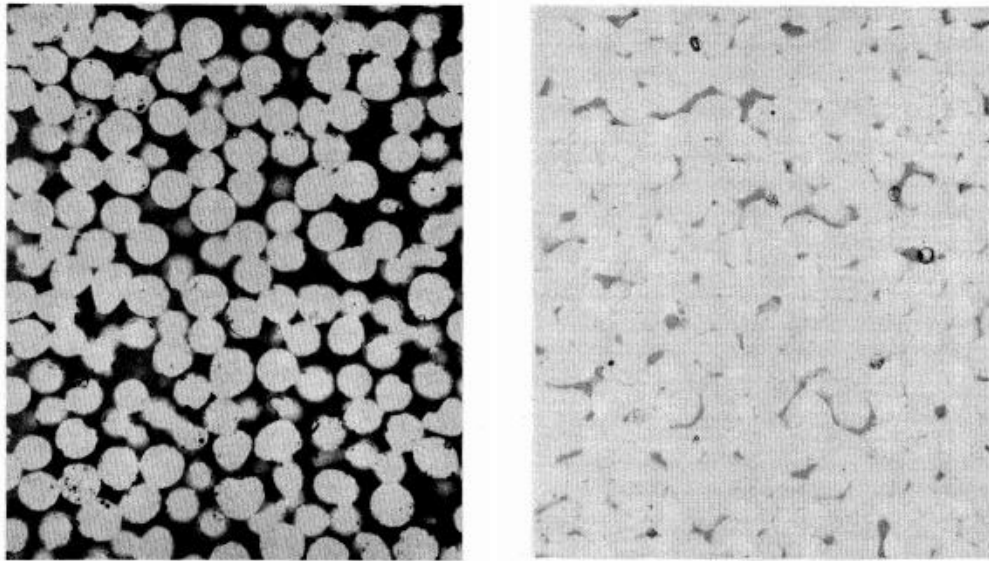
Figure 3 - 6: Micrographs of two fused glass-bead samples with different porosities: 0.315 (left) and 0.061 (right) (Reproduced from Wong et al, 1984)

Rezai et al (2014) sintered glass beads for a VAPEX study. They empirically deduced that different bead sizes gave different porosity (ranging from 37.1% to 20.5%) and permeability values (784 to 18 Darcy), even when exposed to the same temperature profile. They also created vuggy samples by using a secondary medium, wood in their case, which could be burned later to empty up the pore space.
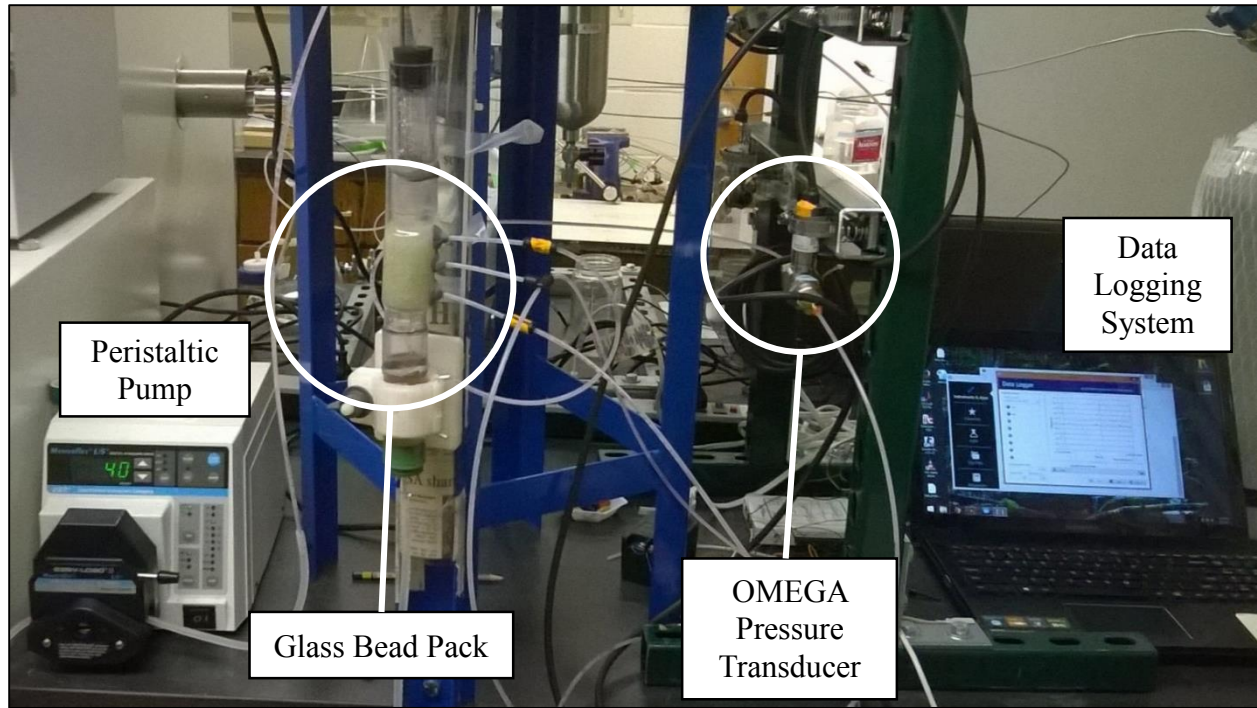
Figure 3 - 7: Experimental set up

3.3.2. Motivation for sintering the glass beads

The initial experiments were conducted in an unconsolidated loosely packed glass bead column. A few problems were faced while conducting those experiments:

1. The experiments were done in a different lab and the core was then moved to the CT lab for scanning. This transportation would occasionally move the beads and the injected particles from their original place. Hence the results from CT were not reliable.

2. Backflow experiment was the method to simulate a clean-up operation in the wellbore. This was not possible with an unconsolidated pack as the filter medium also began to move with the incoming fluid. This changed the porosity and the porosity distribution.

3. Horizontal flow experiments were the last step on the experimental side. They could not be done with an unconsolidated pack as the gravity would cause the filter to loose shape. Meshes were applied at the boundaries to try to maintain the shape of the pack, but that just filtered out the injected particles.

Rezai et al (2014) created sintered glass bead models for their experiment. A similar approach was used to make sintered glass bead pack. It was a process of trial-and-error, and a successful

core was created after multiple attempts. The success of the core was based on achieving significant mechanical strength to sustain flow and to recoup the high porosity that was present in the unconsolidated bead pack.

3.3.3. Sintering process

Glass bead were placed in a cylindrical graphite crucible (Figure 3 - 8), shaken to settle down the beads and then placed in the furnace. The temperature profile was followed, manually for the muffle furnace and automatically for the vacuum furnace. After cooling down, the bead pack was taken out of the furnace and run in a helium porosimeter setup to determine the porosity (as detailed above). A CT scan was also taken of the core to further reinforce the porosity value.

Figure 3 - 8: Galloni 3013 graphite crucible (2.285" OD x 1.415" ID x 3.05" DP)

Core 1

The initial temperature profile (Figure 3 - 9) was loosely based on the profile used by Rezai et al (2014) and a lab guideline by Daniel Breitenstein (ETH Zurich). The maximum temperature was 700 °C and was maintained for 2 hours.

The resultant core (Figure 3 - 10) was a consolidated bead pack that had a high mechanical strength. The beads were solidly in place and did not budge even if scraped with fingernails. The porosity was measured as 26%. This core was considered unsuccessful as we aimed at a higher porosity value.
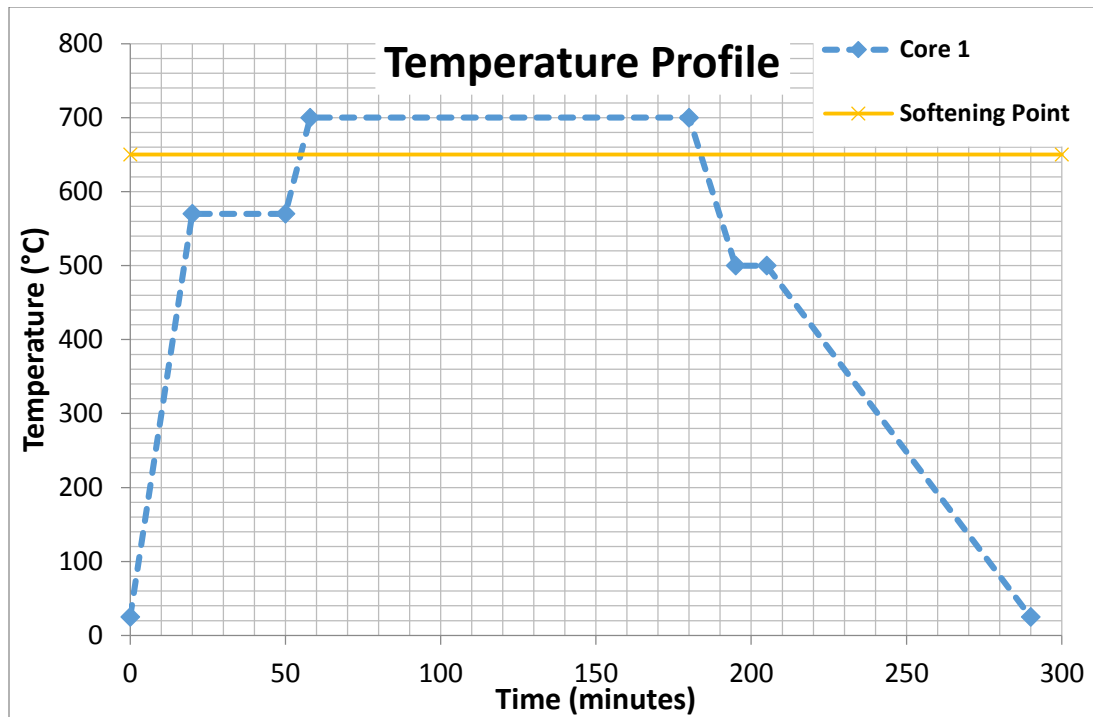
Figure 3 - 9: Initial temperature profile (Core 1)

Figure 3 - 10: First attempt at sintering yielding high mechanical strength with low porosity (Core 1)

Core 2

Based on the results of the first core, the maximum temperature of the core was increased to 725 °C while the exposure time was drastically reduced to 15 minutes. Figure 3 - 11 shows the temperature profile used for the second attempt.

The resultant core (Figure 3 - 12) was an unconsolidated bead pack that had a very poor mechanical strength. The pack started to disintegrate when touched and the beads began to fall off. The porosity was measured as 43%.

This temperature profile was deemed unsuccessful because of the low mechanical strength of the core.
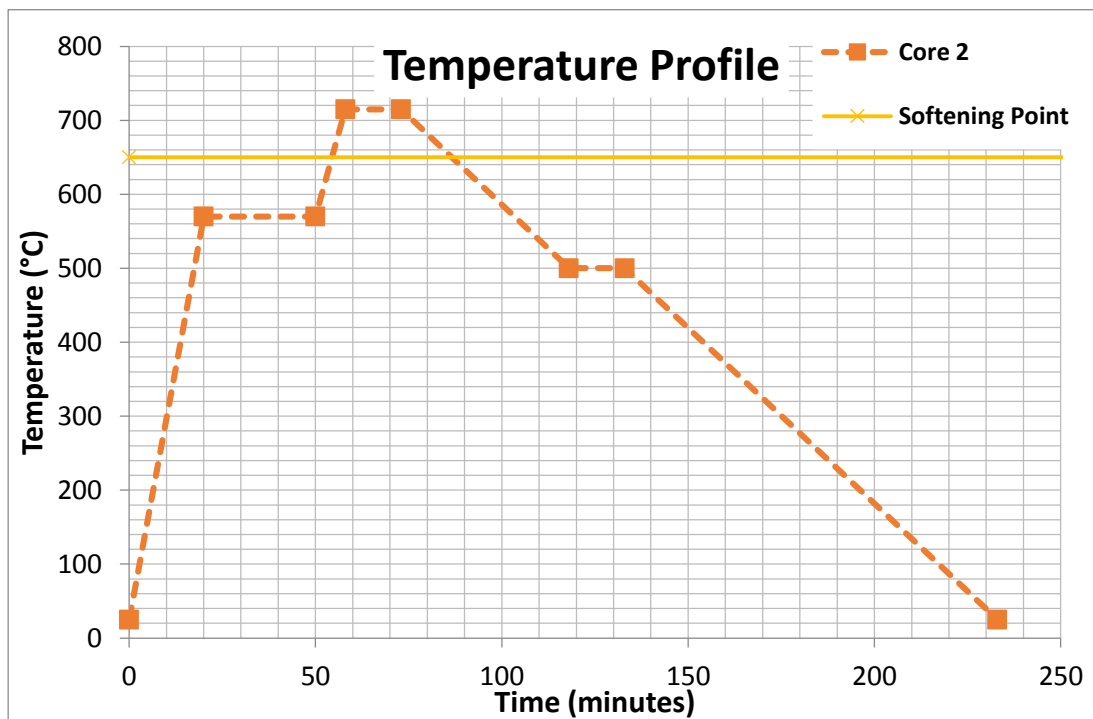
Figure 3 - 11: Improved temperature profile (Core 2)

Figure 3 - 12: Unconsolidated bead pack with high porosity (Core 2)

Core 3

Taking note of the condition of Core 2, only the exposure time at the peak temperature was changed to 25 minutes. Figure 3 - 13 shows the updated temperature profile that was used for the third attempt.
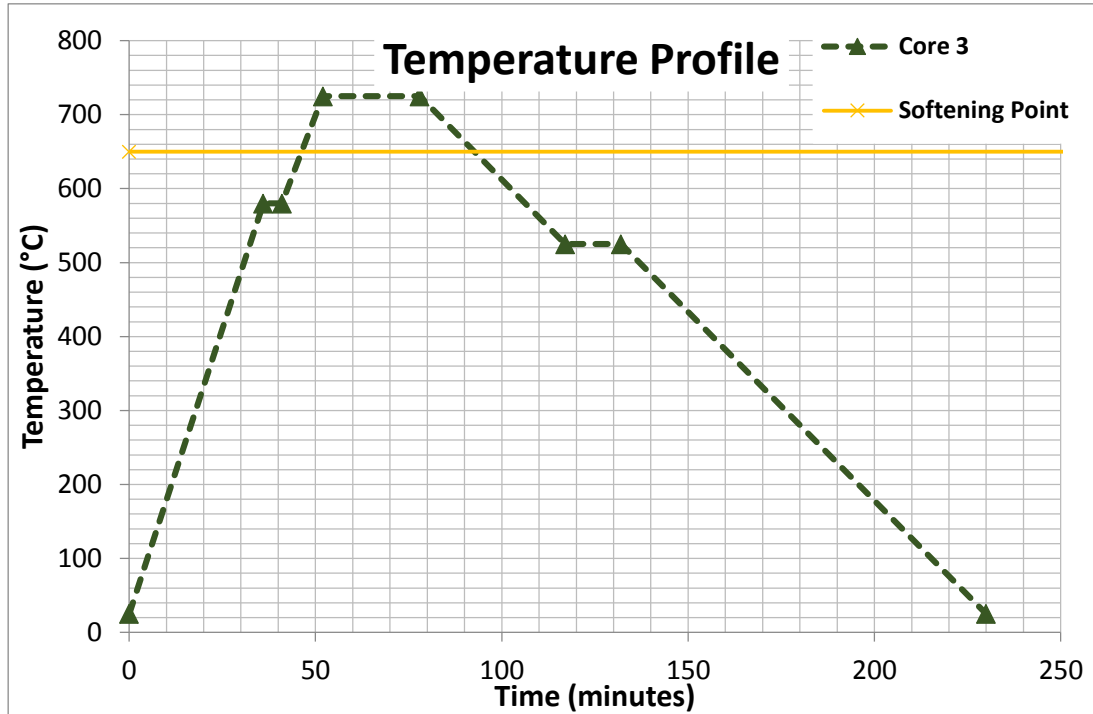
Figure 3 - 13: Further improved temperature profile (Core 3)

Figure 3 - 14: Consolidated bead pack with good mechanical strength and high porosity (Core 3)

The resultant core (Figure 3 - 14) was a consolidated bead pack with a high porosity of 42%. The core had enough strength that it would not disintegrate while handling. This fit the criterion required for a successful core and hence the temperature profile was approved.

The temperature profile was repeated to make a few more cores and the porosity was measured for all of them using a helium porosimeter. An average value of 42%, with a very small variation, was observed. Hence the process was considered repeatable and all the cores made for the flooding experiments followed the same temperature profile.

A micro-CT scan of the core was taken to take a closer look at the features of the sintered core. The in-house CT machine has a resolution of 100 µm while the micro-CT has a resolution of 10 µm.

Figure 3 - 15 shows a detailed view 7 mm inside the core. Even after the sintering process, the glass beads have a high sphericity. This works in our favour as it reduces any surface forces that might come due to a non-spherical shape.
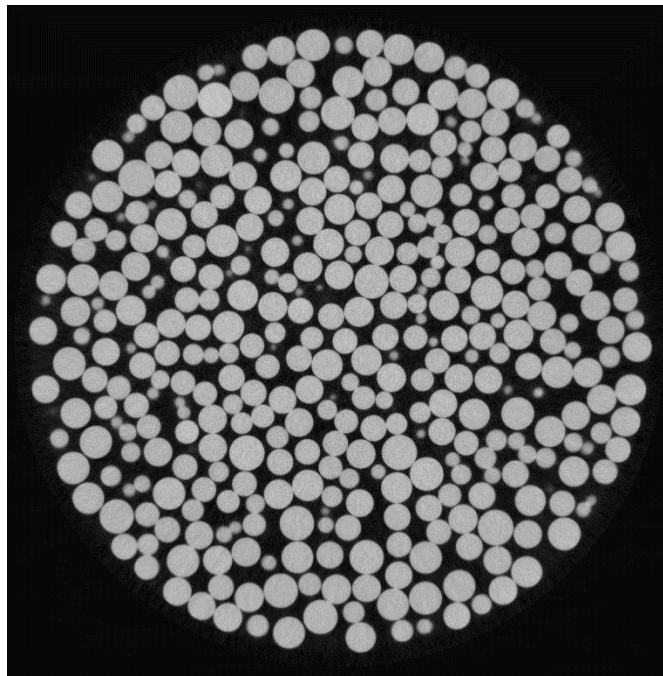
Figure 3 - 15: Micro-CT of sample core, 7 mm from top (Khan, 2016)

3.3.4. Fabricating the core holder

A clear heat shrink tubing (1" ID after shrink) has been applied on the core. Three pressure taps have been made using 1/8" OD x 3/32" ID tubing that are place equidistantly from one another (Figure 3 - 5). An observation window is left at the top of the core to observe the thickness of the filter cake that develops during each core flood (Figure 3 - 16). The core holder is then placed on a hanging metal frame that keeps the core in place during the flow experiment, transportation between the two labs and during the CT scan.
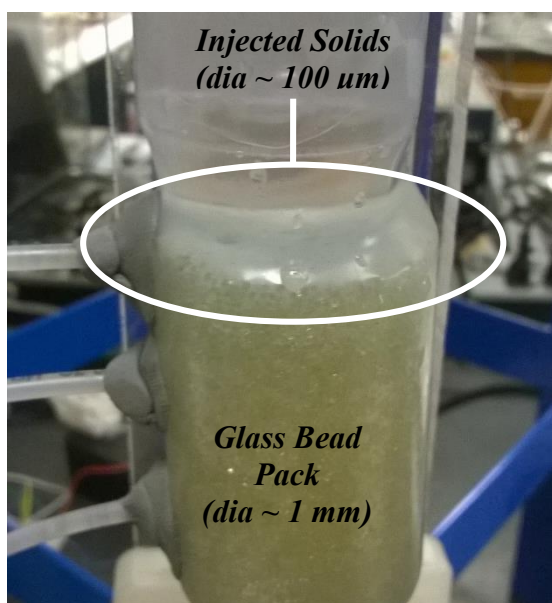
Figure 3 - 16: Filter cake seen through the observation space on top of core

3.4. Experimental procedures

3.4.1. Preparation of the core

The experiments were performed on a soda-lime glass bead pack with a bead size of 1 mm. Glass beads were sintered to form a solid rigid core using the process described above. Porosity was measured using the helium porosimeter. Each 1.415" × 2.5" DP glass bead core was set in heat shrink tubing with 3 pressure taps placed equidistantly. The core was flooded with deionized water and an initial CT scan was taken. A flow experiment with only water was conducted using different flow rates. An initial estimate of the permeability of the core was calculated from that. The core was then mounted on the stand as in Figure 3 - 7.

3.4.2. Flow experiments

The core holder was set vertically with flow in the top-down direction. The top of the core holder was connected to the reservoir with a glass bead suspension in deionized water (Figure 3 - 5). A set (Table 3 - 4) of bimodal concentrations were flooded through the core at 40, 60 and 80 cc/min. For making a comparison between different cases, the total particle volume injected in each experiment was kept constant. Hence the flow time for each case was different.

Table 3 - 4: Flow experiments for bimodal cases

Reference Name	Flow rate [cc/min]	Conc. [vol %]	Size 1 [μm]	Size 2 [μm]	Reference Name	Flow rate [cc/min]	Conc. [vol %]	Size 1 [μm]	Size 2 [μm]
R4005	40	0.5	25	50	F6020	60	2	50	100
R6005	60	0.5	25	50	F4020	40	2	50	100
R4010	40	1	25	50	F4010	40	1	50	100
R6010	60	1	25	50	F6010	60	1	50	100
R4020	40	2	25	50	F6005	60	0.5	50	100
R6020	60	2	25	50	F4005	40	0.5	50	100
B6020	60	2	25	100	B4010	40	1	25	100
B8020	80	2	25	100	B6010	60	1	25	100

The effluent for each experiment was collected and filtered through an 11-μm filter paper. The residue was then dried in a convection oven before being measured using an analytical mass balance. The filter cake thickness is also measured through the observation window.

3.4.3. Computed tomography imaging

Computed tomography (CT) was selected as an imaging technique for the formation damage experiments due to its ability to provide 3D damage information in a non- destructive manner.

The CT experiments were done in the in-house modified medical scanner in PGE department. The vertical scanning mode was utilized for all these experiments.

Before the core flood, the core is set in the core holder and an initial CT scan is taken. The parameters set for scanning are shown in Table 3 - 5.

Table 3 - 5: CT scan parameters

Parameter	Value
Scan time	3 sec
Scan thickness	3 mm
Scan point distance	3 mm
Voltage	100 keV
Current	200 mA

After the flooding experiment, the core is again brought to the CT lab where another scan is taken at exactly the same positions. The output from the scanner is processed using MATLAB code (Appendix B) which results in a CT number for each slice. The initial and final scans are overlain on each other and a difference in CT number is calculated.

3.4.4. Final core processing

After all the experiments are complete, the heat-shrink tubing is removed. Any filter cake present on the core is brushed off, collected and weighed. The core, which now contains the filter medium and the deposited injected particles, is then air dried and weighed. A mass balance is performed on all the mass collected to double-check the measured values.

3.5. Digital signal processing

Digital signal processing is the numerical manipulation of sampled discrete-time signal, with the intention to measure, filter and/or compress continuous analog signals (Stranneby, 2004). It is used to improve the quality of experimental data, helping in making a sound analysis. Digital

signal processing has been used to reduce mechanical background noise and clean out the input pressure signals.

3.5.1. Digital filters

A z-transform is a mathematical transformation that converts a discrete-time signal into a complex frequency domain.

A digital filter can be viewed as a linear transfer function expressed in the z-domain as (Barr and Chan, 1986):

$$H(z) = \frac{Y(z)}{X(z)} \quad \text{.. (Equation 3.3)}$$

where Y(z) is the z-transform of the filtered output, X(z) is the z-transform of the input signal and H(z) is the z-transfer function.
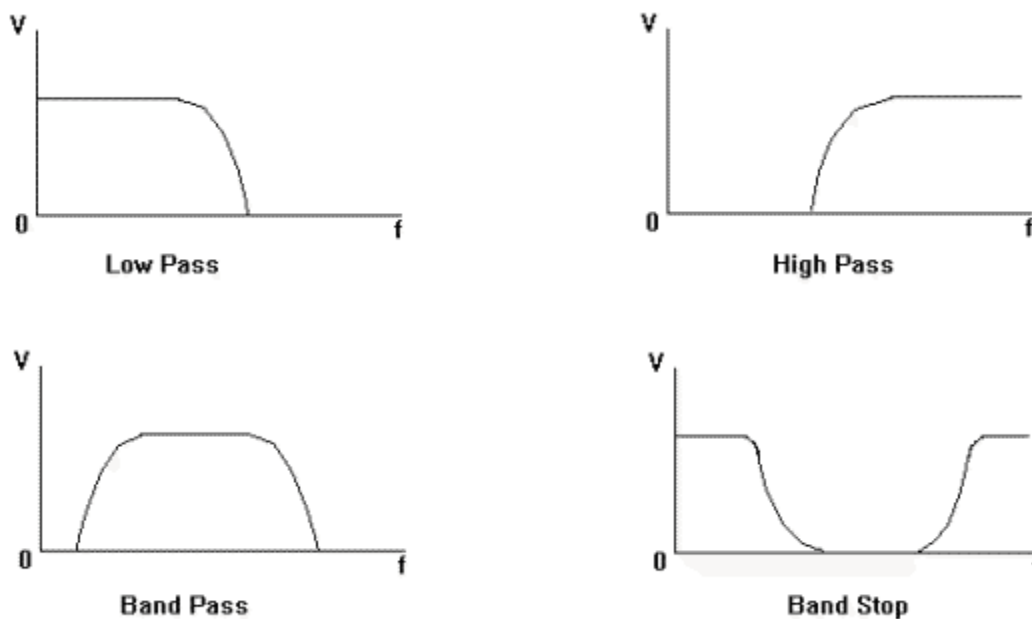
Figure 3 - 17: Types of filter

A filter can be low pass, high pass, band pass or a band stop filter (Figure 3 - 17). A low pass filter allows signal in the frequencies lower than the cut-off frequency to pass. A high pass filter allows signals higher than the cut-off frequency to pass. A band pass filter allows signal between the two cut-off frequencies to pass, a band stop filter allows signal between the two cut-off frequencies to stop.

3.5.2. Infinite impulse response (IIR) filters

These are recursive digital filters that require both the input value and the past outputs. M-order filters take the general form of:

$$Y(z) = \frac{\sum_{k=0}^{M} a_k z^{-k}}{1 + \sum_{k=1}^{M} b_k z^{-k}} \; X(z)$$ …………….…………………..…………………. (Equation 3.4)

Where a_k and b_k are the filter coefficients and M is the filter order. For the cases under study, a low pass filter has been selected with a normalized cut-off frequency is 1×10^{-4}. The constants for such a filter are calculated as:

Table 3 - 6: Filter coefficient parameters for a 4th order Butterworth filter with a normalized cut-off frequency of 0.0001.

k	a_k	b_k (x 10^{-14})
1	1	0.0652
2	-3.992	0.2609
3	5.9975	0.3914
4	-3.9975	02609
5	0.9992	0.0652

Butterworth filters are an example of an IIR filter.

3.5.3. Fourier transform

Fourier transform is a decomposition of a signal in time or space to frequency domain. For non-periodic or transient signals, the Fourier transform is defined as:

33

$$F[x(t)] = X(\omega) = \int_{-\infty}^{\infty} x(t)e^{-jwt}\,dt$$

It can be used to find the frequencies that are present in any signal.

3.5.4. Fast Fourier transform

Fast Fourier transform (FFT) is a computation technique that computes the discrete Fourier transform (DFT) by taking advantage of the repetitive nature of the $[e^{-j2\pi/N}]$ term. DFT takes N^2 operations for calculation while FFT takes $N \log_2 (N)$ operations for the calculation. For a 1024 term signal, the FFT is a 100 times faster than a DFT.

Digital filters and the FFT can be combined to improve the quality of the signal before making any conclusions.

3.5.5. Post-processing
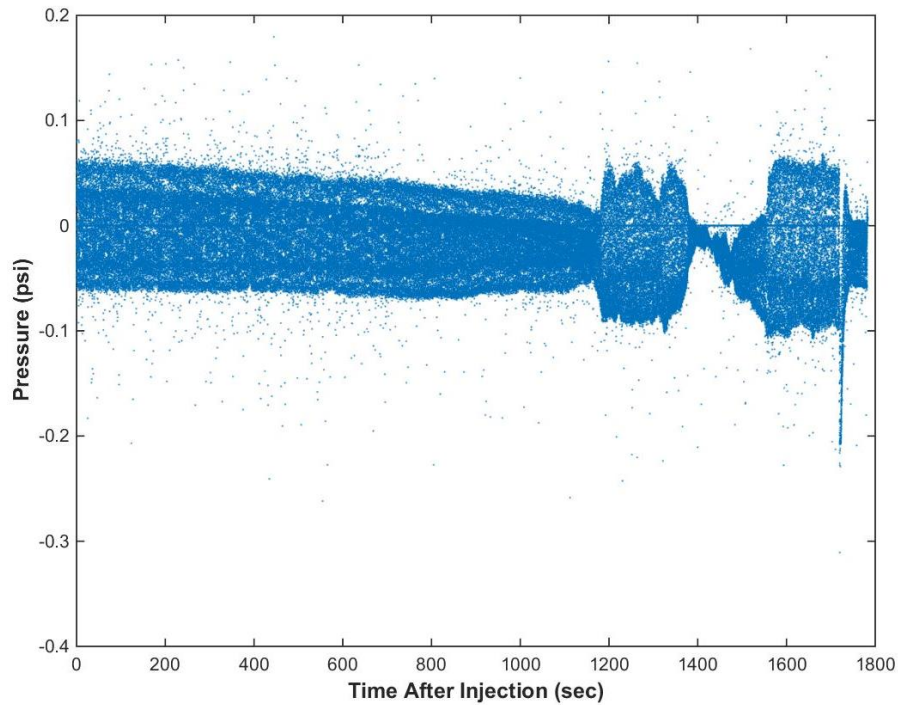
Figure 3 - 18: Voltage plot against time for F4020 (q = 40 cc/min and total injection concentration = 2%)

The voltage plot generated from the pressure transducers contains a lot of inherent electrical and mechanical noise. A sample plot from experiment F4020 is shown in Figure 3 - 18.

The data is cleaned up using a digital 4th order low pass Butterworth filter (Figure 3 - 19).
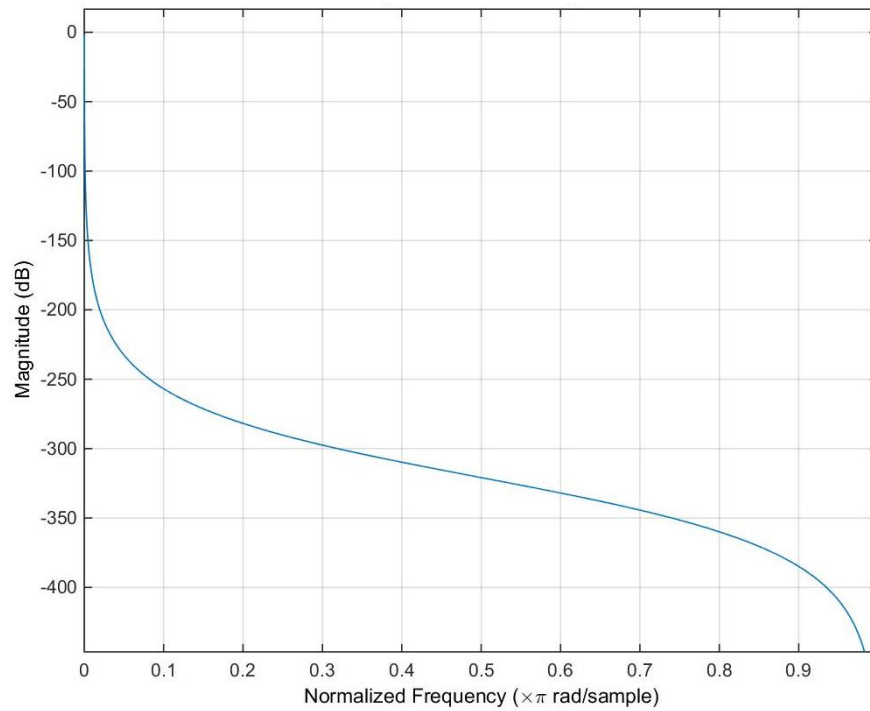
Figure 3 - 19: 4th order Butterworth filter visualization
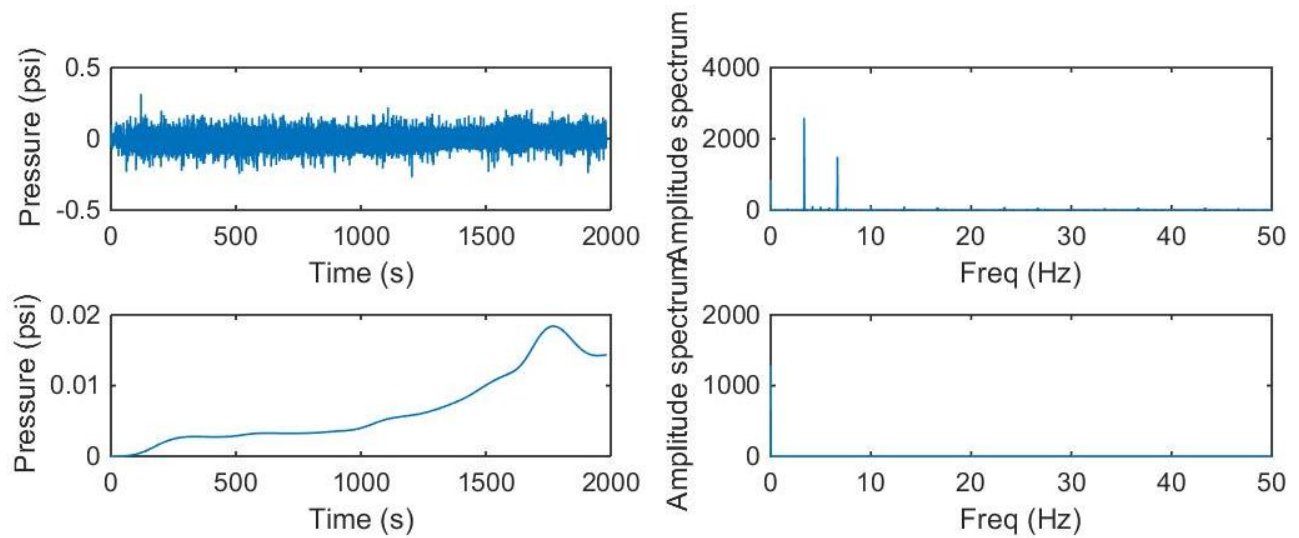
Figure 3 - 20: Clockwise from top-left: Input signal; Input signal in frequency domain; filtered signal in frequency domain; and filtered signal in time domain.

The cut-off frequency is uniquely set for each experiment based on the response in the frequency spectrum. Figure 3 - 20 shows the unfiltered original signal and the filtered signal after application of the 4th order low pass Butterworth filter. A clear trend can be observed.

Chapter 4: Results and Discussion

A set of bimodal size particles at different concentrations were flooded through the core at varying flow rates. Porosity measurements were taken before and after the flow experiment and porosity value was estimated. Pressure measurements at three points along the core were measured over time (Figure 3 - 5). A voltage plot over time was generated from the pressure transducers, which was converted to pressure. The data was then filtered to remove the effect of mechanical and flow vibrations and get the pure signal for each case (Figure 4 - 13).

The cases are summarized in Table 3 - 4 above.

This section has two parts and details the results obtained from the experiments. The first part covers the results obtained from the porosity measurement while the second part goes over the outcome from the flow experiment. Three parameters (fluid flow rate, injected particle concentration and injected particle size) were changed for the experiments. The subsections are arranged to look at the effect on the porosity and permeability by each of these three parameters.

4.1. Porosity measurements

4.1.1. Overview

As detailed in the previous chapter, a CT scan of the core is taken before and after the flow experiment. The scans are processed through a MATLAB code (Appendix B) which results in a CT number for each slice. The initial and final scans are overlain and a difference in the CT numbers is calculated. This CT number is then converted into a change in porosity value using the formula:

$$\phi_{reduction} = \frac{(CT\ Number)_{after} - (CT\ Number)_{before}}{(CT\ Number)_{glass} - (CT\ Number)_{DI\ water}} \quad \ldots\ldots\ldots\ldots\ldots\ldots\ldots\ldots\ldots\ldots\ldots\ (Equation\ 4.1)$$

Figure 4 - 1 shows the CT number results of an initial and final scan of the core. As shown in Table 3 - 5 in the chapter above, the thickness of the scans is 3 mm and the distance between each scan point is 3 mm. The first scan is taken after manually positioning the top of the core, and hence can contain some part of the surrounding fluid, water in this case. This results in a much lower CT number value for the topmost scan.
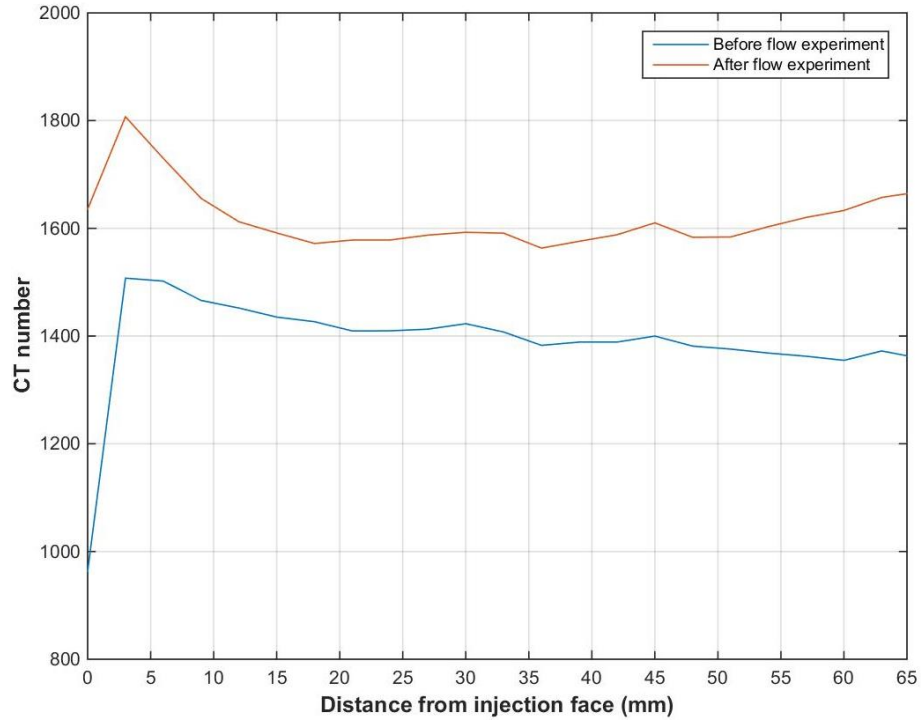
Figure 4 - 1: Before and after CT scans for F4020 (q = 40 cc/min and total injection concentration of 2%)

Figure 4 - 2 shows CT scans for the two topmost sections. The first scan shows the effects of the boundary fluid and the tapered top of the core while the second scan (right) shows the image from inside the core. This highlights how the boundary affect can alter the results. Similarly the last scan has a high uncertainty because of the boundary effect, and has hence been neglected in the study. For all cases in this study, the first scan has been neglected from the quantification but included in the figures for the sake of completeness.
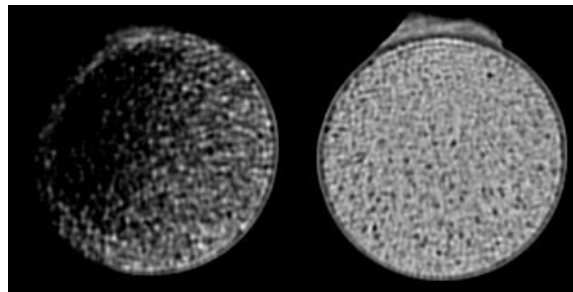
Figure 4 - 2: CT scan from top: (left) at boundary and (right) 3 mm inside the core for F4020 (q = 40 cc/min and total injection concentration of 2%)
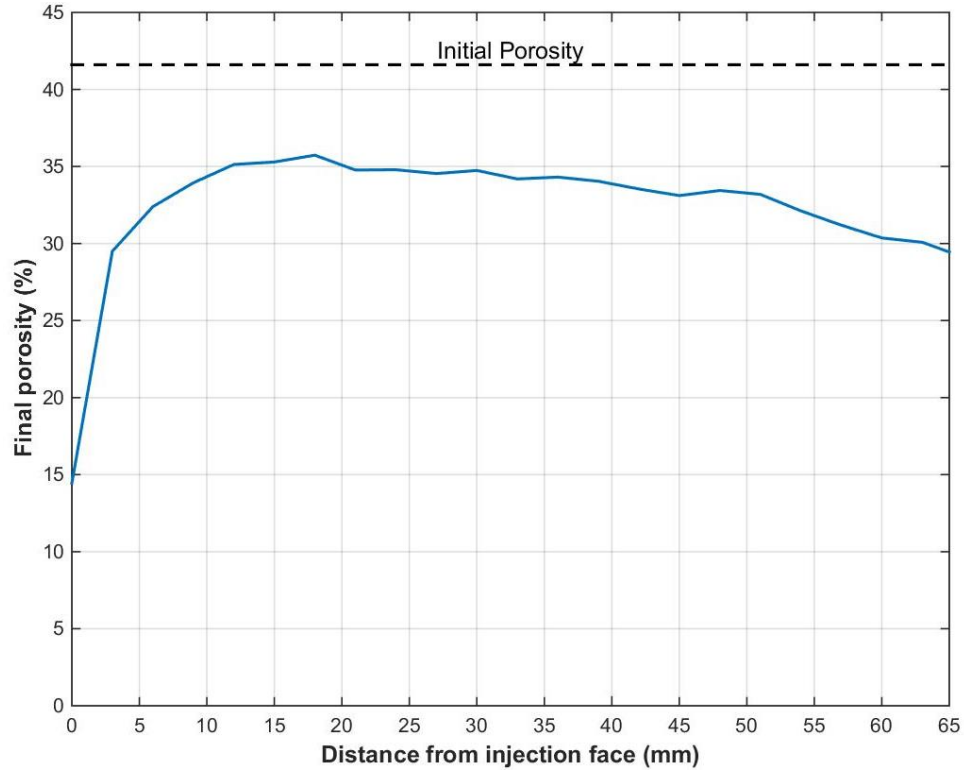
Figure 4 - 3: Final profile measured along the length of the core for F4020 (q = 40 cc/min and total injection concentration of 2%)

Figure 4 - 3 shows the average initial porosity and the calculated final porosity values along the distance from the injection face. The final porosity is calculated by subtracting the change in porosity from the average initial porosity.

This sort of profile is expected as the capture sites in the injection face are filled first, resulting in straining and filtering of the rest of the particles.

4.1.2. Injected particle size

Equal concentrations of two sizes out of 25, 50 and 100 µm beads were used in each experiment set. The total mass over time of injected particles was kept constant for all experiments.

4.1.2.1. Experiment set B (25/100 µm mixture)

The first set of experiment had a mixture of 25 and 100 µm particles.
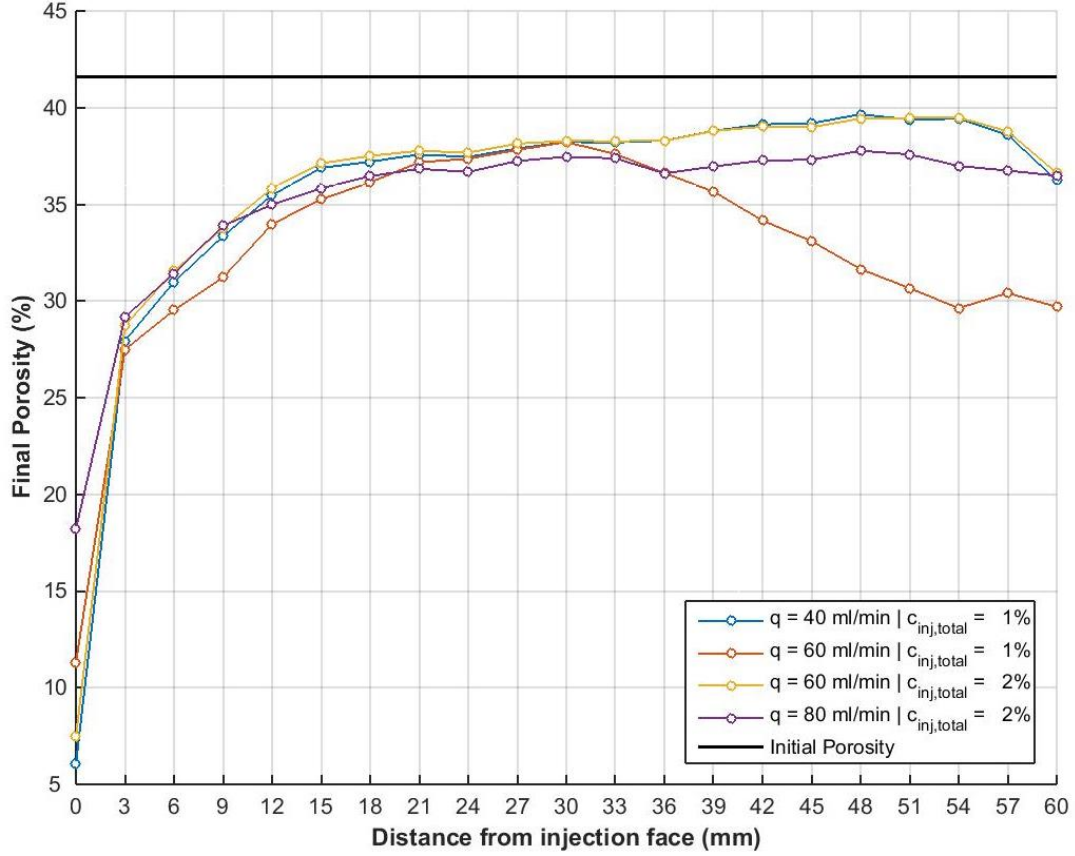
Figure 4 - 4: Final porosity profile for experimental set B (25/100 micron injected particle size)

For all the cases, a large drop in porosity is initially observed at 3 mm. The porosity then rises steadily for all the cases until halfway inside the core. The porosity is almost stabilized, or increases moderately for all cases except B6010 (q = 60 cc/min and total injection concentration = 1%). B6010 sees a sharp fall in the porosity value, suggesting that the injected beads penetrated deeper inside the core.

The lowest porosity observed is for the case B6010 with 27% porosity at the injection face.

4.1.2.2. Experiment set F (50/100 μm mixture)

This set of experiment had a mixture of 50 and 100 μm particles.

For all the cases, the final porosity value right after the injection face (3 mm) is the lowest porosity achieved. The porosity increases steadily showing a negative exponential profile for all except 402 (q = 40 cc/min and total injection concentration = 2%). F4020 tapers off after peaking

at 18 mm, reaching a low of 30% at the end of the core. This again suggests that the particles penetrated deeper inside the core. For all the cases, a prominent filter cake was observed (Figure 4 - 6) at the end of the flow period.

The lowest porosity observed is for the case F4020 with 29% porosity at the injection face.
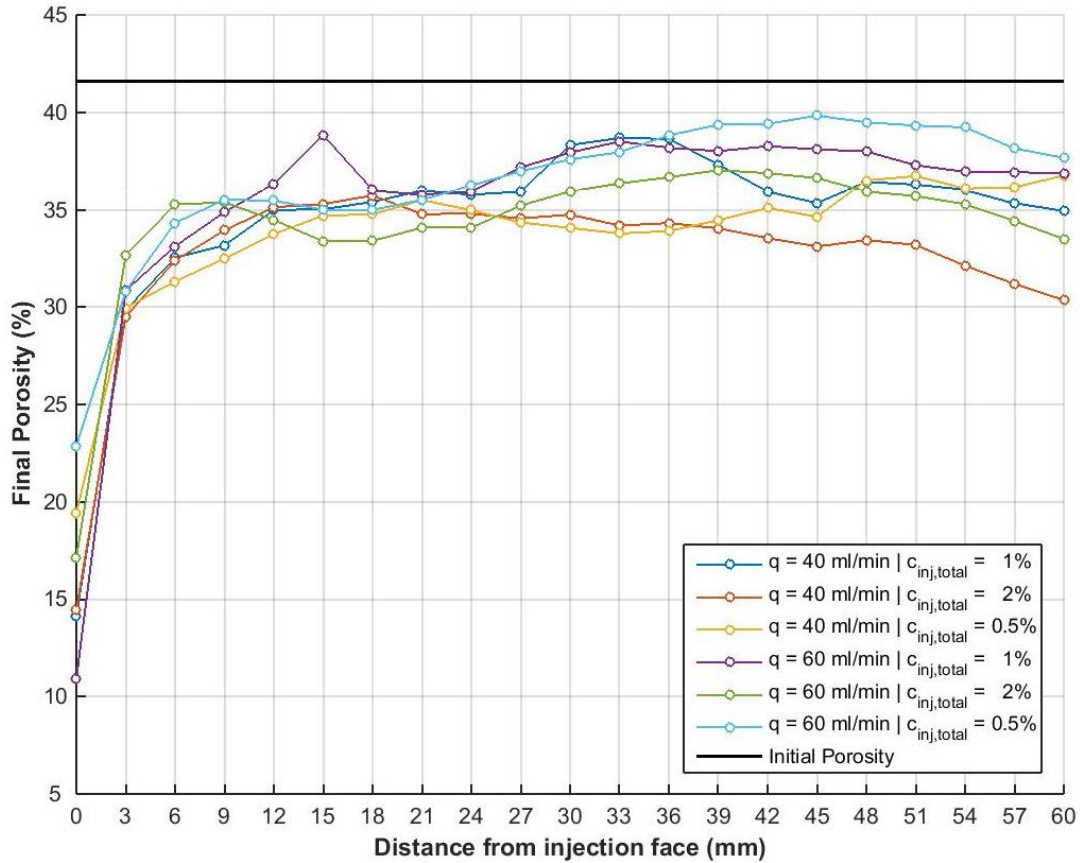
Figure 4 - 5: Final porosity profile for experimental set F (50/100 micron injected particle size)

4.1.2.2. Experiment set R (25/50 μm mixture)

The last set of experiments had a mixture of 25 and 50 μm particles.

For all cases except R4005 (q = 40 cc/min and total injection concentration = 0.5%), a slight change in porosity is observed due to the injection of particles. Most of the particles have completely passed through the core, and were collected as the effluent. This observation was complemented by the collecting the effluent, and filtering out the injected particles. The ratio of total mass of particles in the effluent to the injected particles is close to unity, suggesting that

majority of the particles have completely passed through the system (Table 4 - 1). Furthermore no filter cake was observed for any of the cases in this experimental set, unlike a prominent filter cake seen in the previous cases (B and F).
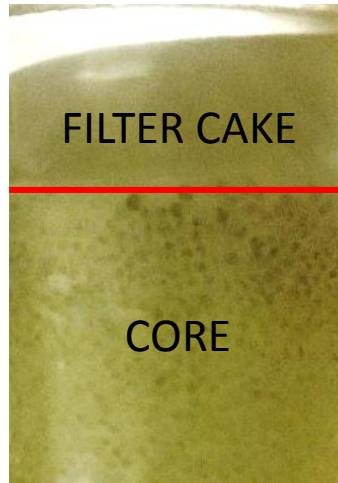
Figure 4 - 6: Filter cake for case F1 (q = 60 cc/min and total injection concentration = 2%)

For the case R4005, a prominent drop in porosity in the near injection face is observed. It then increases following a logarithmic profile, and steadies after 36 mm. This profile is radically different from the other profiles in this set.

The lowest porosity observed is for the case R4005 with 34% porosity at the injection face.

Table 4 - 1: Ratio of mass of effluent to injected particles (R4005 means q = 40 cc/min and total injection concentration = 0.5%)

Experiment case	$\dfrac{Mass\ of\ effluent\ particles}{Mass\ of\ injected\ particles}$
R4005	0.72
R6005	0.88
R4010	0.99
R6010	0.99
R4020	0.98
R6020	0.98
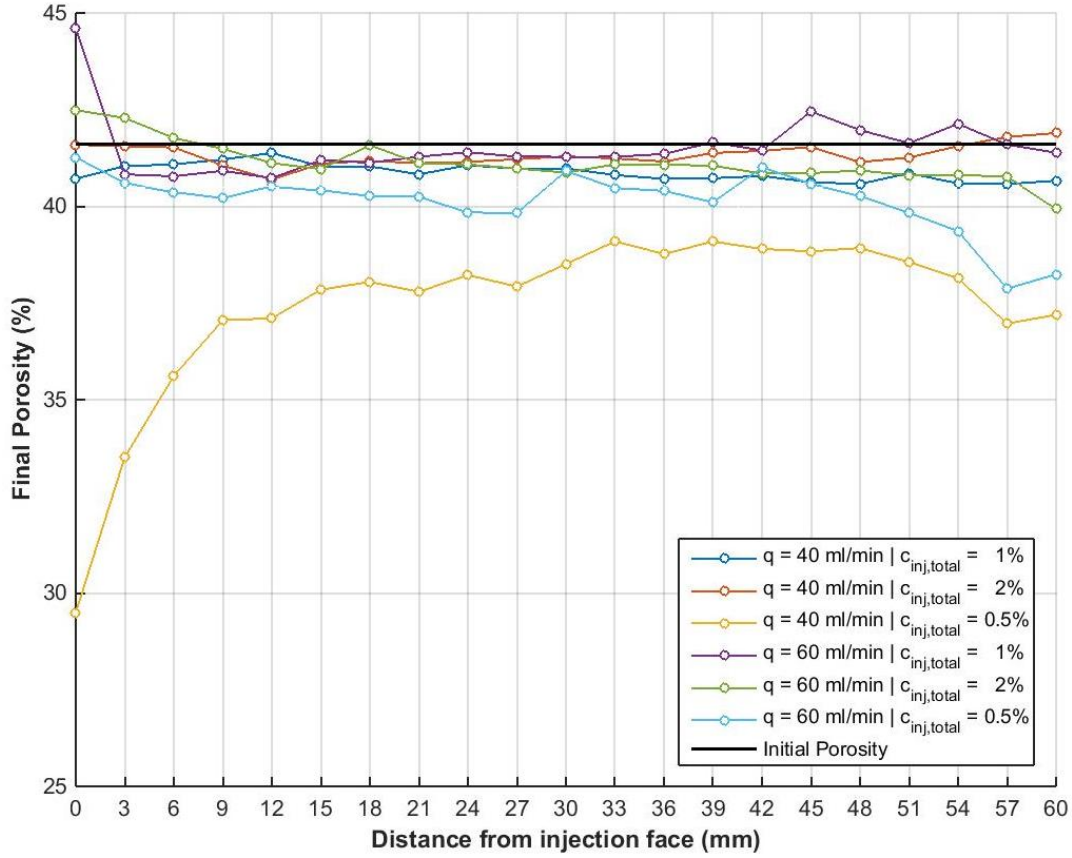
Figure 4 - 7: Final porosity profile for experimental set R (25/50 micron injected particle size)

4.1.3. Fluid flow rate

Two flowrates, 40 and 60 cc/min have been prominently used in the experiment set. 80 cc/min is used briefly in experiment set B (25/100 µm injected particles).

4.1.3.1. Flow rate 40 cc/min

Two prominent profiles can be identified in Figure 4 - 8 above. The first profile (for two cases of experimental set R – 25/50 µm particles) can be observed which shows almost no decline in the porosity over the length of the core. The second prominent profile shows a logarithmic increase in the porosity for the first 10 mm of the core, and then it stabilizes. Case R4005 is part of the second profile.
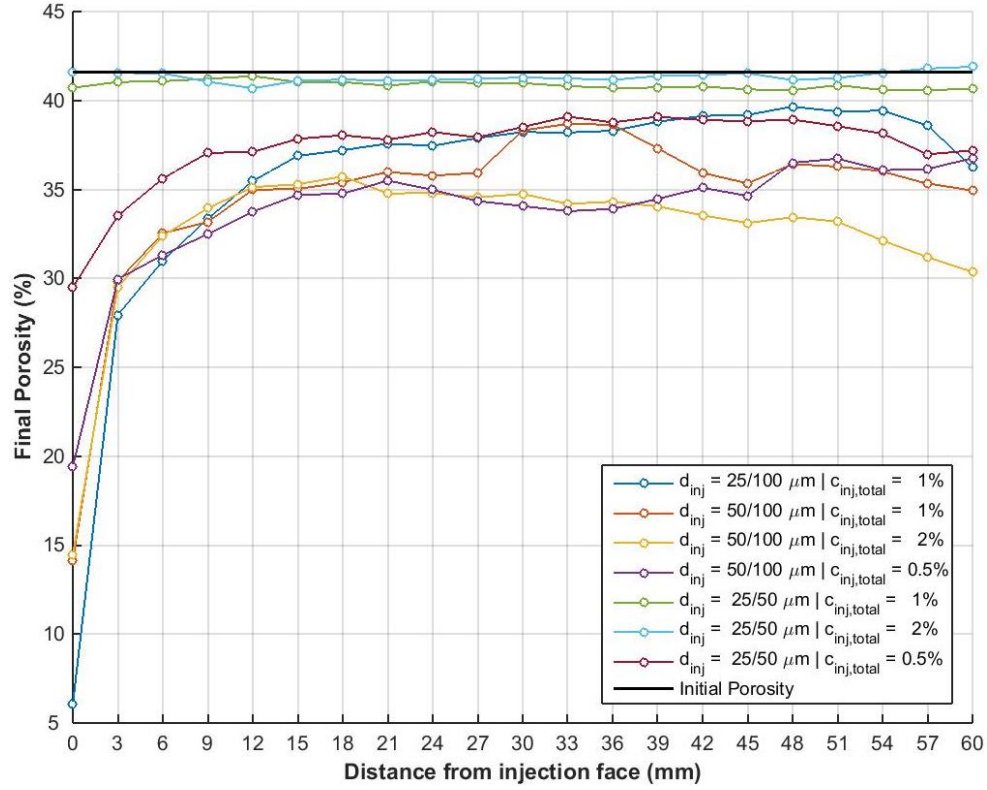
Figure 4 - 8: Final porosity profile for flow rate = 40 cc/min
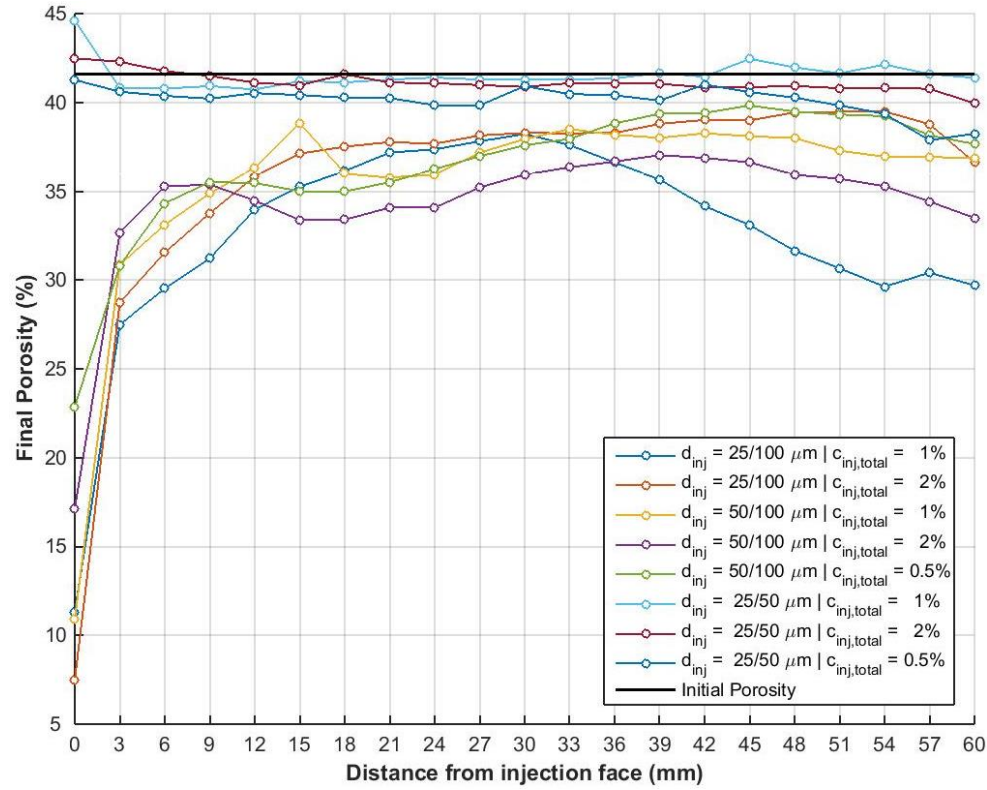
Figure 4 - 9: Final porosity profile for flow rate = 60 cc/min

4.1.3.2. Flow rate 60 cc/min

Again, two prominent profiles can be observed in below. Experimental case R (25/50 µm particles) shows almost no change in porosity over the length of the core. The other two cases (25/100 and 50/100 µm particles) show a logarithmic profile that stabilizes after 20 mm. Case B6010 shows a unique profile in the latter part of the core, where the porosity plummets from 37% at 30 mm to 30% at the end of the core.

4.1.4. Total injection particle concentrations

Three concentrations (0.5%, 1% and 2% by weight) of injected particles were chosen for the experiments. Since the cases run are bimodal, the weight ratio of the two particles is kept as unity for all the cases. The total mass of injected particles was kept constant to make the comparison between the different experimental cases, hence the flow time was different for all cases.

4.1.4.1. Total concentration 0.5%

Case R6005 shows a small depreciation in the final porosity value over the length of the core. The other cases show a negative exponentially increasing profile, with the value in the near injection face being the lowest.

4.1.4.2. Total concentration 1%

Two prominent profiles can be seen in . The first shows no or slight change in porosity over the length of the core and consists of experiments from set R (25/50 µm particles). The second profile shows a logarithmic profile that stabilizes 30 mm inside the core. Case B4010 shows a dip in the porosity after the 30 mm mark inside the core.
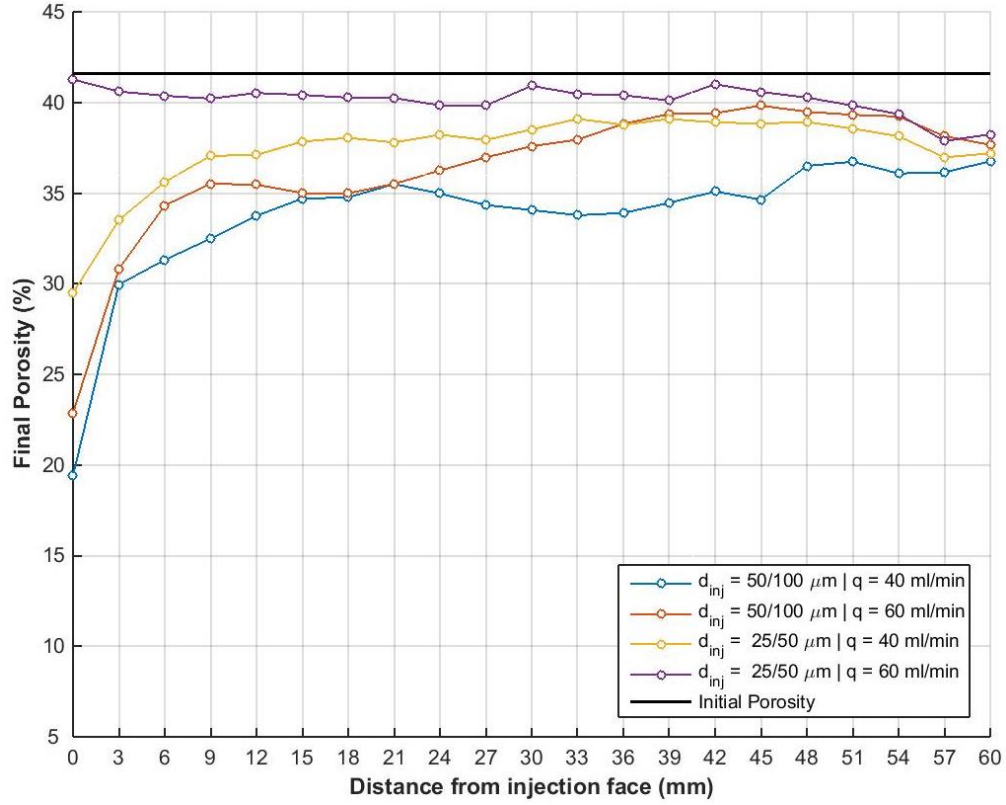
Figure 4 - 10: Final porosity profile for total injection concentration = 0.5%
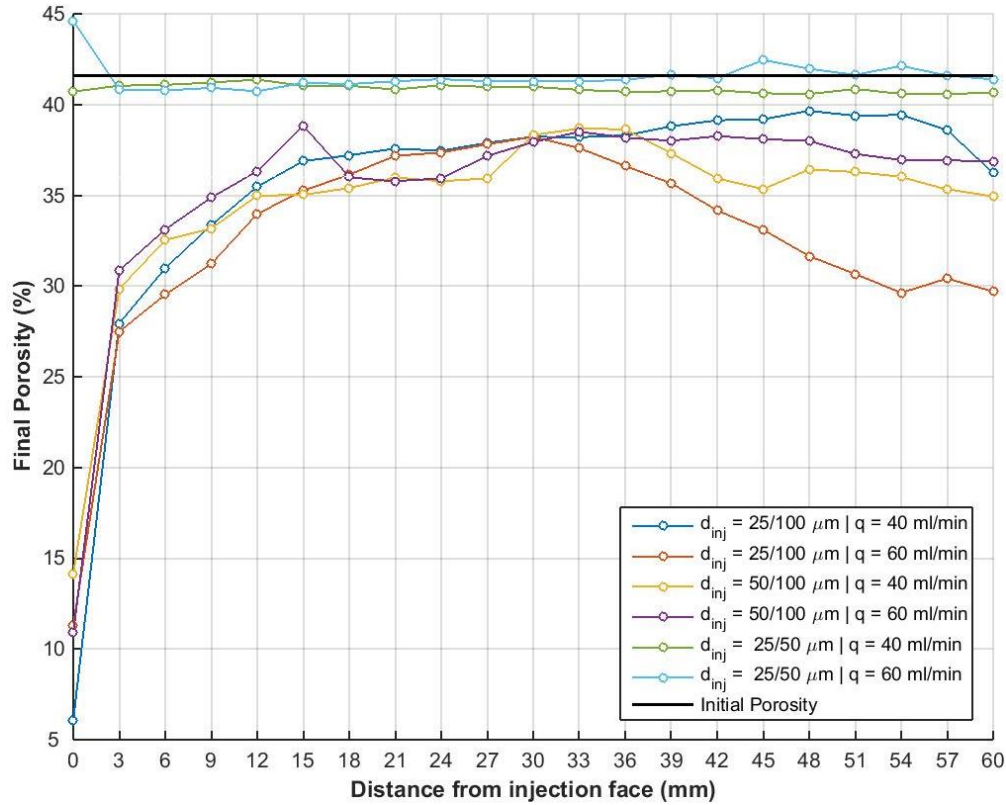
Figure 4 - 11: Final porosity profile for total injection concentration = 1%

4.1.4.3. Total concentration 2%

Two prominent profiles can be seen in Figure 4 - 12. The first shows no or slight change in porosity over the length of the core and consists of experiments from set R (25/50 µm particles). The second profile shows the same initial values for the first 12 mm, following a logarithmic profile. The different cases then stabilize at different values. The profiles are parallel to some extent in the latter part of the core. Case R6005 (q = 60 cc/min and total injection concentration = 0.5%) is a modification of the second profile where the final porosity in the near injection face region
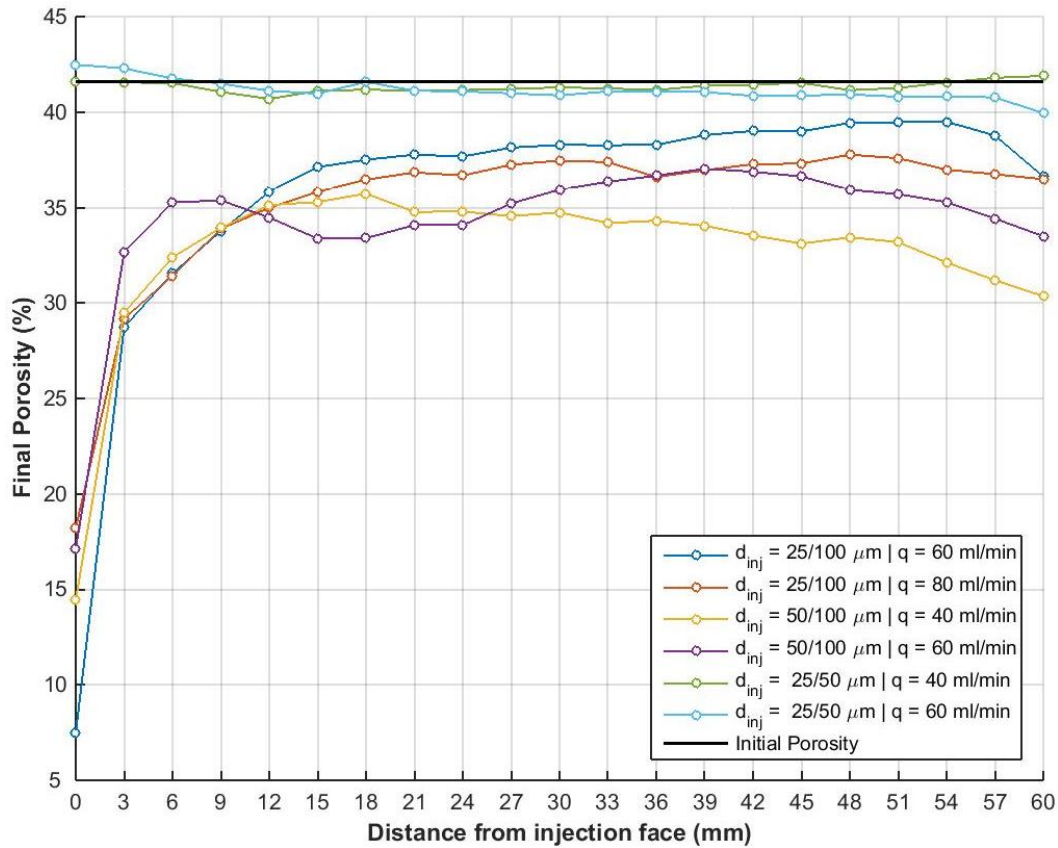
Figure 4 - 12: Final porosity profile for total injection concentration = 2%

4.2. Pressure measurements

4.2.1. Overview

As detailed in the previous chapter, a voltage plot is generated from the pressure transducers. The voltage output (V) is linearly related to the pressure (psi) by a factor of 5. The pressure data set has mechanical vibrations and other high frequency noise embedded in it. These are eliminated using a 4-th order Butterworth filter. Figure 4 - 13 shows the unfiltered (top) and filtered pressure plot.

The pressure was ultimately converted to permeability measurement using Darcy's law. To allow comparison between the different sets of experiments, the permeability and injection time have been made dimensionless. The permeability is normalized with respect to the initial permeability of the core and called normalized permeability, while the time has been normalized with the total time to inject 1.2 PV of suspended particles and called dimensionless volume (DV). Figure 4 - 14 shows a plot for the case F4020 (q = 40 cc/min, total injected particle concentration = 2% for 50/100 µm particles).
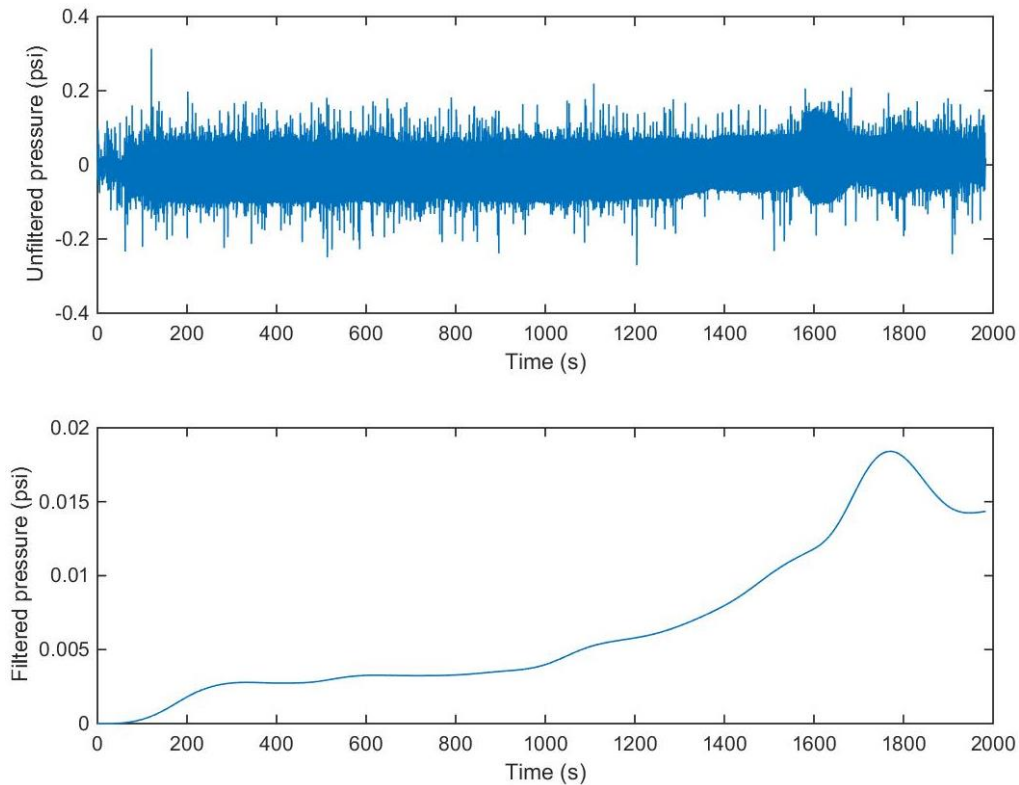
Figure 4 - 13: Unfiltered (top) and filtered (bottom) pressure response for top zone in F4005 (q = 40 cc/min, total injection concentration = 2% for 50/100 µm particles
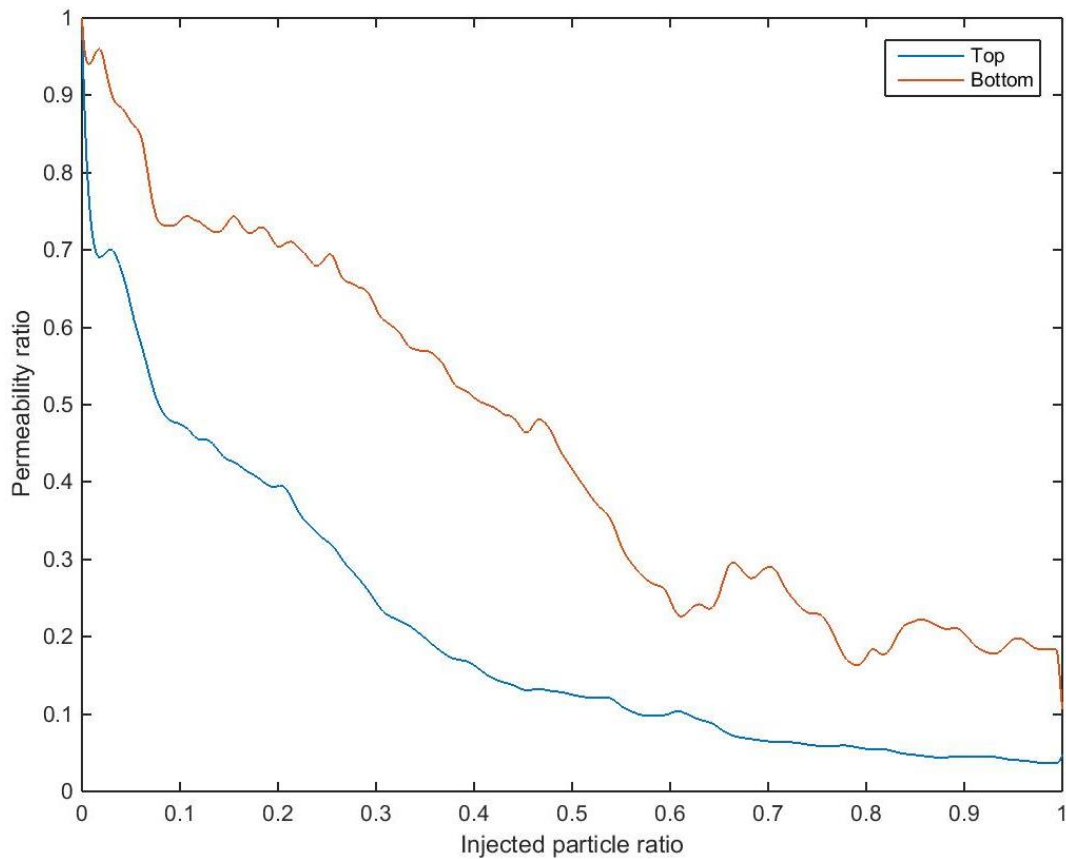
Figure 4 - 14: Top zone permeability over time for F4005 (q = 40 cc/min, total injection concentration = 2% for 50/100 μm particles

A sharp declining trend in permeability is initially observed for the first hundred seconds in Figure 4 - 14. This drop can be attributed to the plugging of the deposition sites on the surface of the core. The formation of external filter cake can also contribute to this effect. The drop is then halted and a slight build up in permeability is noticed. Two theories are suggested for explaining this phenomena:

1. The plugging of the surface sites cause a localized surge in pressure. If this pressure increases to more than the retention pressure, the particle is freed to move again. The freeing of the particle creates room for the fluid suspension to move easily, hence resulting in a drop in pressure: ultimately resulting in an increase in the permeability.

2. Fingering is taking place in the large particles that form the external filter cake. The fingers create a new and less resistance path for the fluid to take hence resulting in the drop in pressure (or increase in permeability). A bigger sized particle or multiple bridged

particles shut-off the finger after a while which results in the normal decline in the permeability.

As done in the previous section, the results of different cases have been arranged by particle size, fluid flow rate and the total injection concentration.

4.2.2. Injected particle size

The total mass of particles injected was kept constant for all the study cases.

4.2.2.1. Experiment set B (25/100 μm mixture)

The first set of experiment had a mixture of 25 and 100 µm particles.
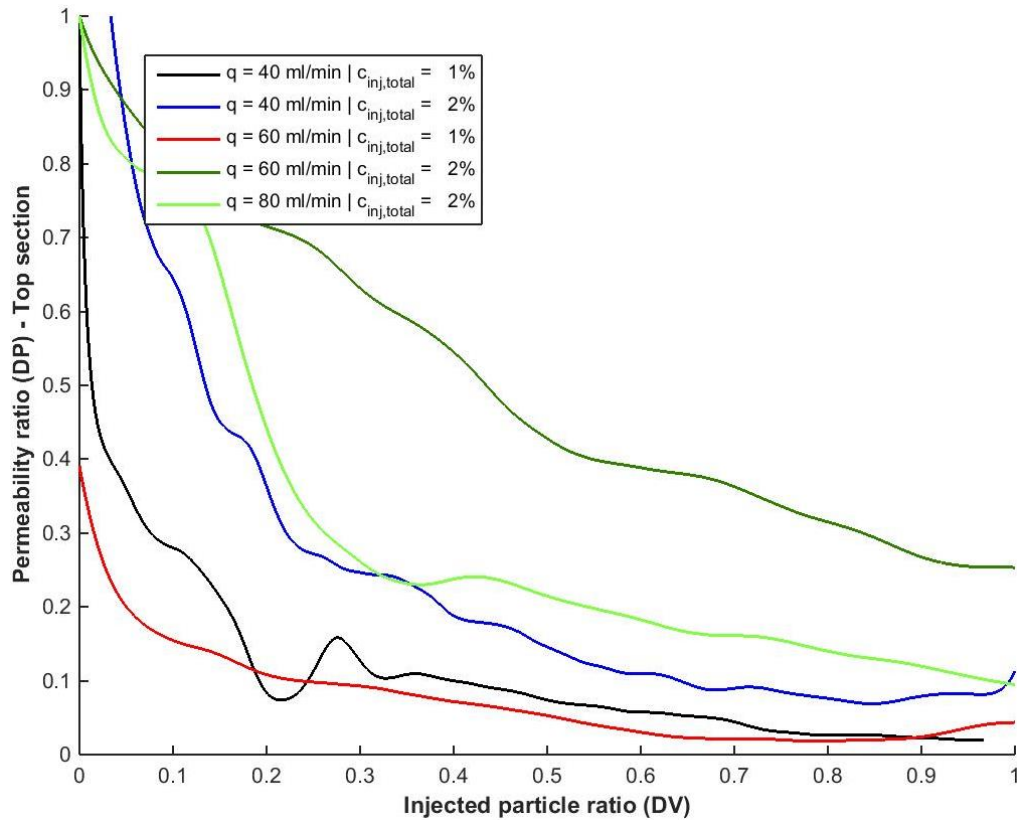
Figure 4 - 15: Top zone permeability ratio for experimental set B (25/100 μm particles). DP is normalized permeability.

A wide range of permeability drops are observed in the top section of the core. A large decrease in the permeability in the first 0.2 DV is observed in all cases, except B6020 (q = 60 cc/min and total injection concentration = 2%). B6020 shows a steady decline in the permeability.

In the bottom section, the maximum permeability change observed is 40%. B402 (q = 40 cc/min and total injection concentration = 2%) shows a very late change in permeability in the bottom section of the core, after 0.85 DV.

4.1.2.2. Experiment set F (50/100 µm mixture)

This set of experiment had a mixture of 50 and 100 µm particles.

A similar profile can be observed for all the cases in the top section of the core. The permeability drops drastically by 60% in the first 0.01 DV, and then steadies down to 0.15 ± 0.05 normalized permeability. The initial drop can be explained by trapping of the larger sized particles by the formation. This immediately forms a filter cake and creates new trapping site for the smaller sized particles. This coupled blocking reduces the flow inside the formation.

For the same time period, the permeability in the bottom section only drops by 20% - 30%. The permeability then declines to ± 0.65 normalized permeability for all the 60 cc/min cases. Permeability in F4020 and F4005 continues to decrease to 0.1 normalized permeability over the course of the injection.

Case F6020 (q = 60 cc/min and total injection concentration = 2%) is an outlier. In the top section, the permeability drops to about 0.12 normalized permeability in less than 0.04 DV, then it decline steadies to reach 0.03 normalized permeability by the end of injection. This corresponds to the permeability change in the bottom section, which shows no change until after 0.34 DV.

4.2.2.3. Experiment set R (25/50 µm mixture)

The last set of experiment had a mixture of 25 and 50 µm particles.

As expected from the porosity profile above, the permeability changes slightly for all the cases. The maximum drop in permeability is by 30% in the top and bottom section of the core.

Case R4005 is again a standout case as it shows almost no change in permeability in the bottom section until after 0.34 DV.
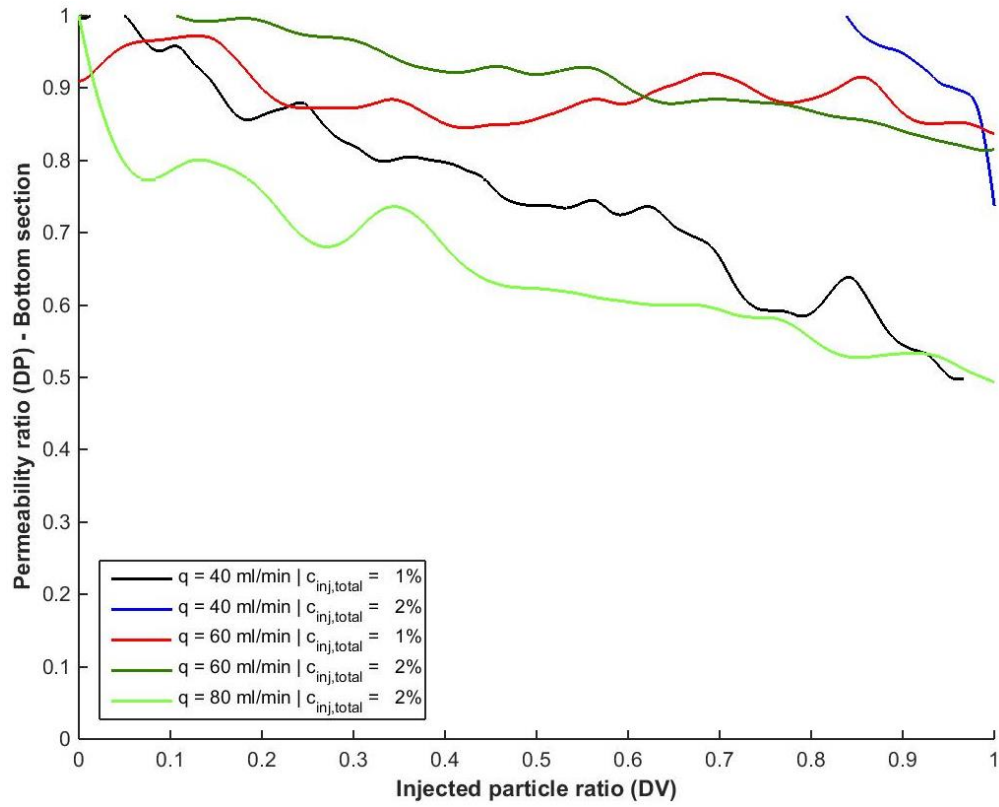
Figure 4 - 16: Bottom zone permeability ratio for experimental set B (25/100 µm particles). DP is normalized permeability.
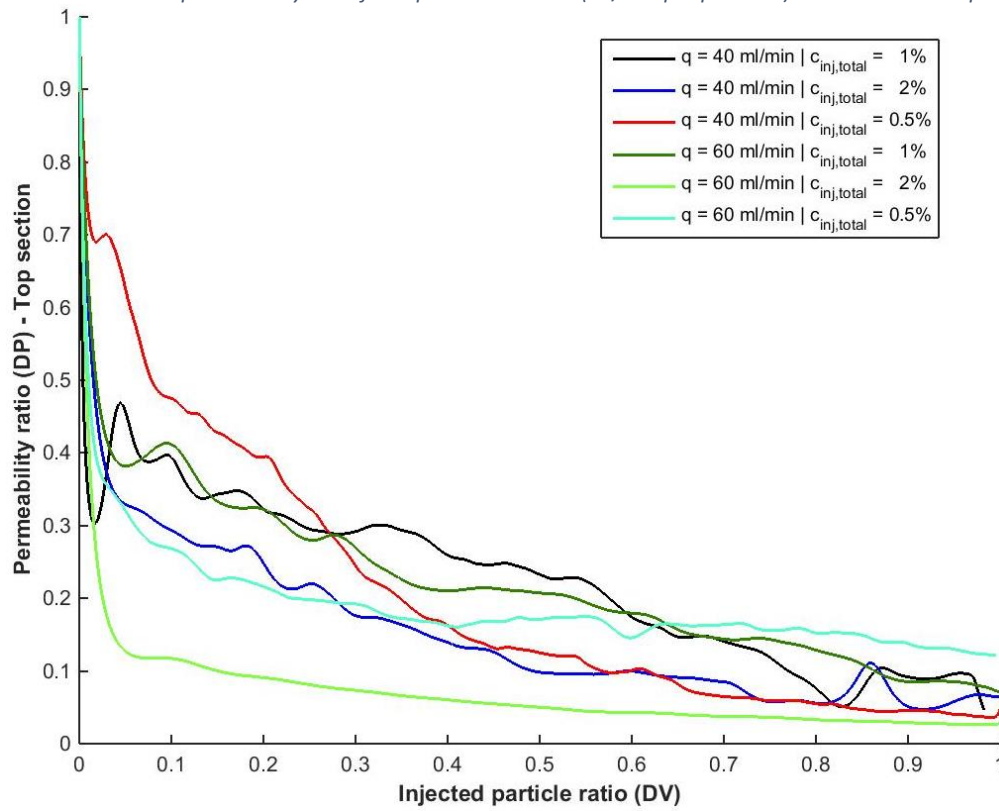
Figure 4 - 17: Top zone permeability ratio for experimental set F (50/100 µm particles). DP is normalized permeability.
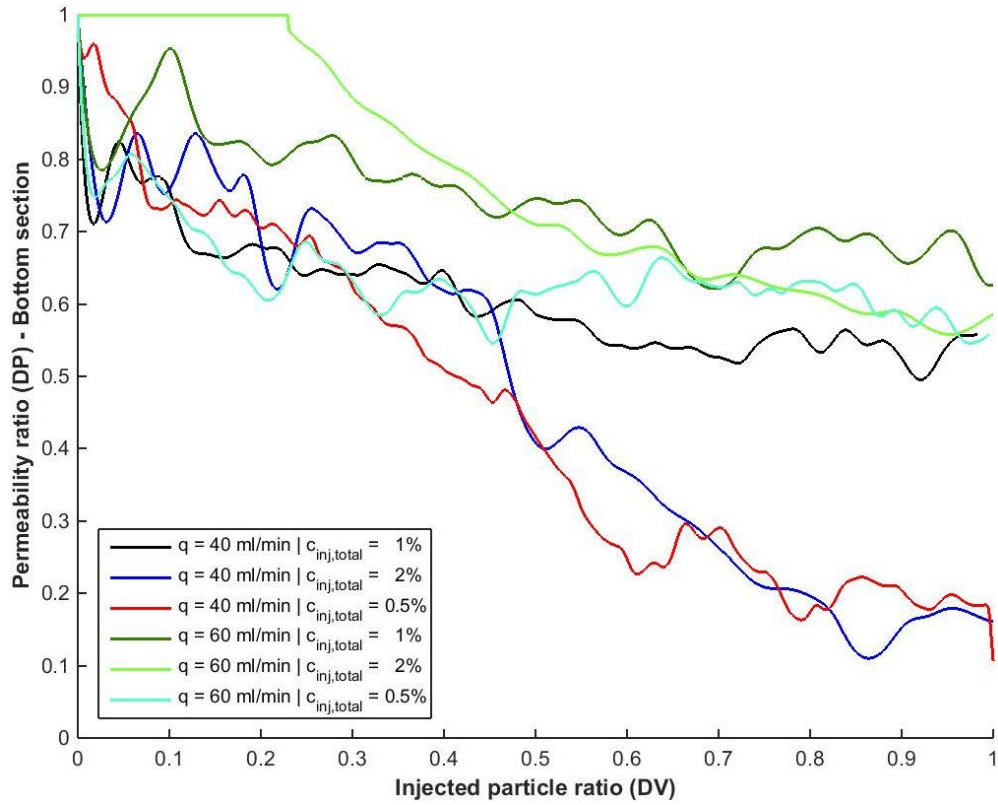
Figure 4 - 18: Bottom zone permeability ratio for experimental set F (50/100 μm particles). DP is normalized permeability.
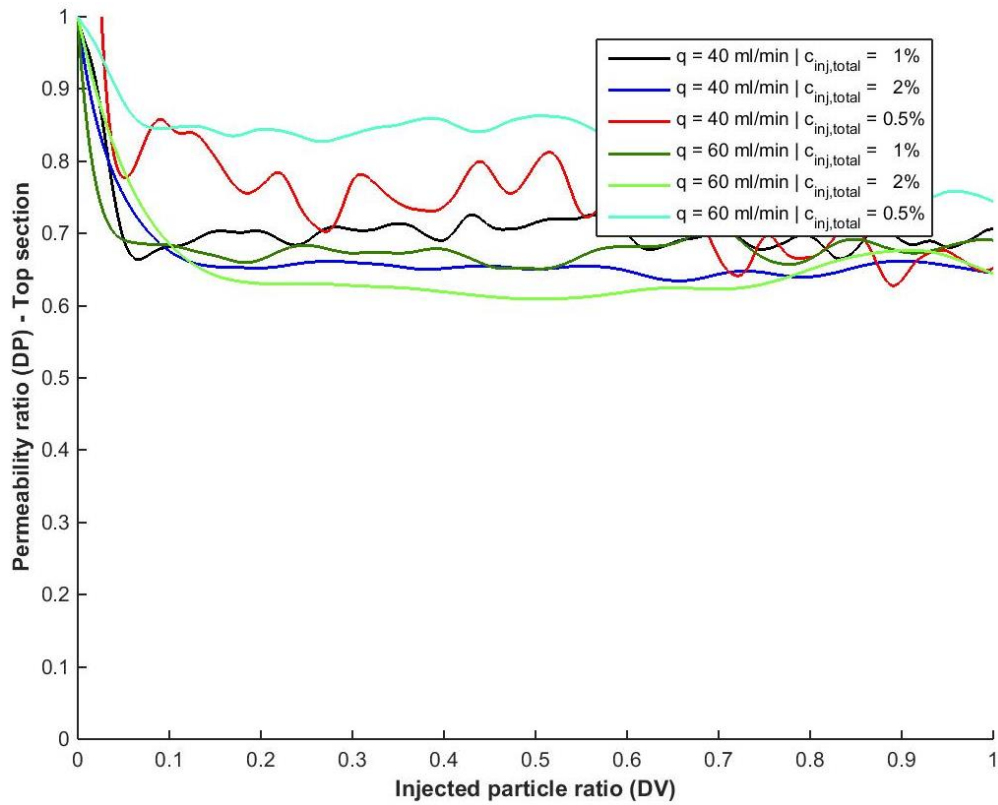
Figure 4 - 19: Top zone permeability ratio for experimental set R (25/50 μm particles). DP is normalized permeability.
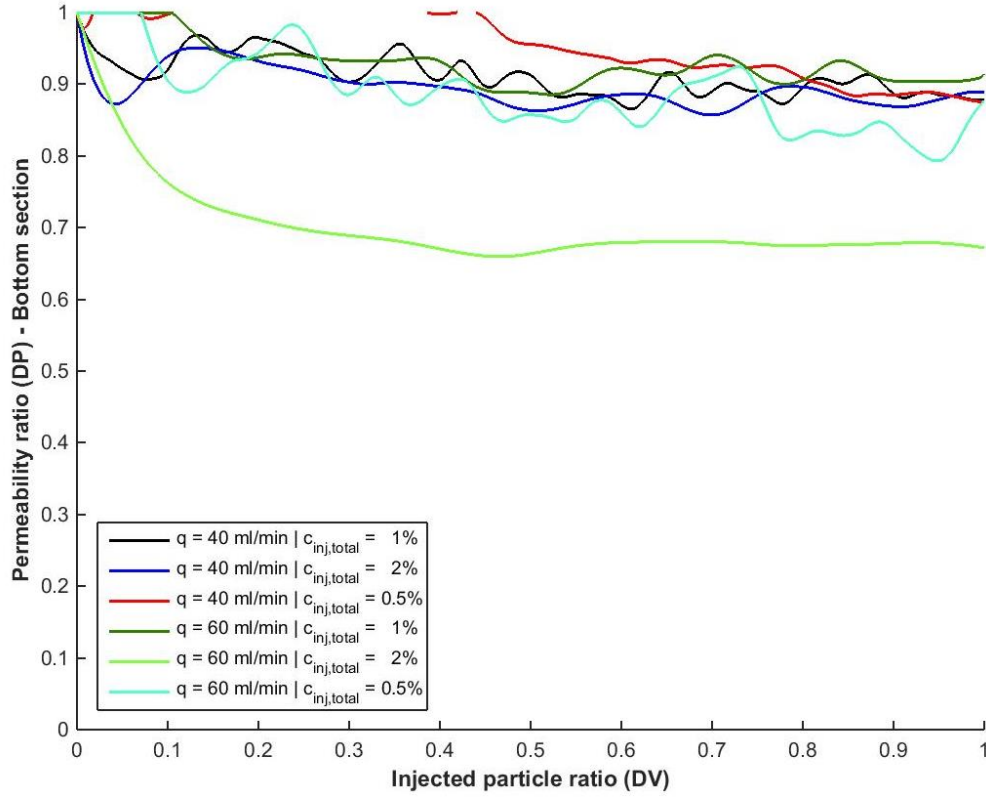
Figure 4 - 20: Bottom zone permeability ratio for experimental set R (25/50 µm particles). DP is normalized permeability.

4.2.3. Fluid flow rate

Two flowrates, 40 and 60 cc/min have been prominently used in the experiment set. 80 cc/min makes a brief appearance in experiment set B (25/100 µm injected particles)

4.2.3.1. Flow rate 40 cc/min

Two prominent profiles can be identified in above. The first profile shows a small decline in the permeability for the first 0.1 DV, and then remains constant at ± 0.7 normalized permeability. This profile is exclusively shown by the experimental set R (25/50 µm injected particles). The second prominent profile shows an exponential decay in permeability to reach ± 0.05 normalized permeability by the end of injection. This profile is showed for the other two experimental cases.
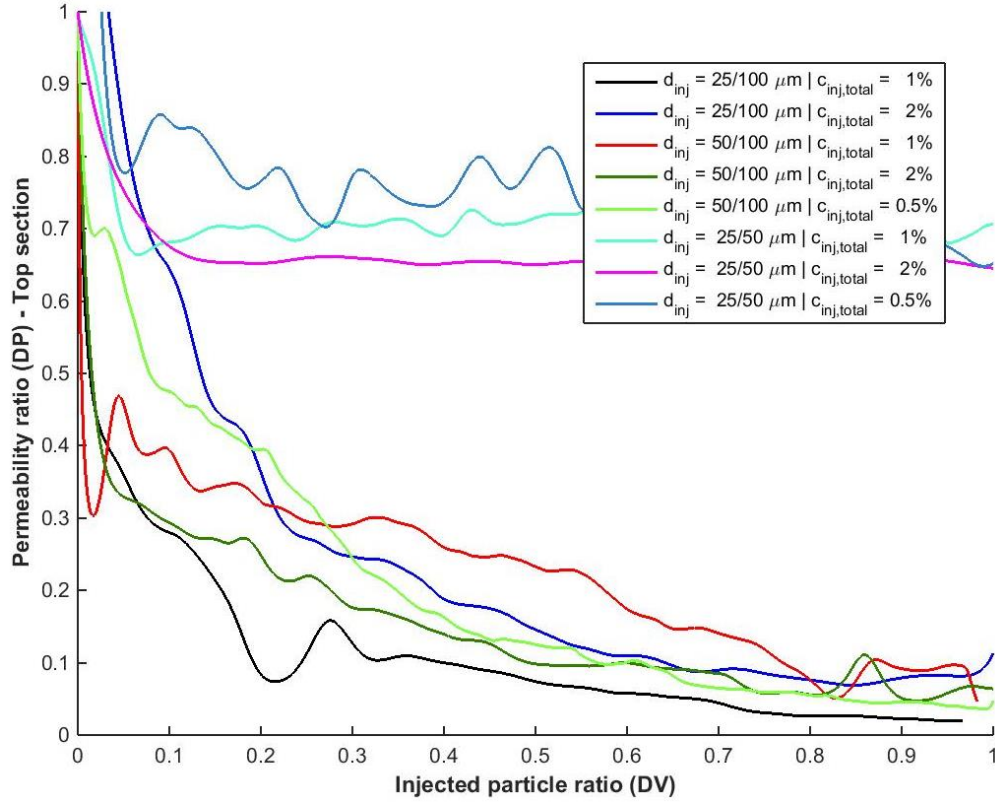
Figure 4 - 21: Top section permeability ratio for flow rate = 40 cc/min. DP is normalized permeability.
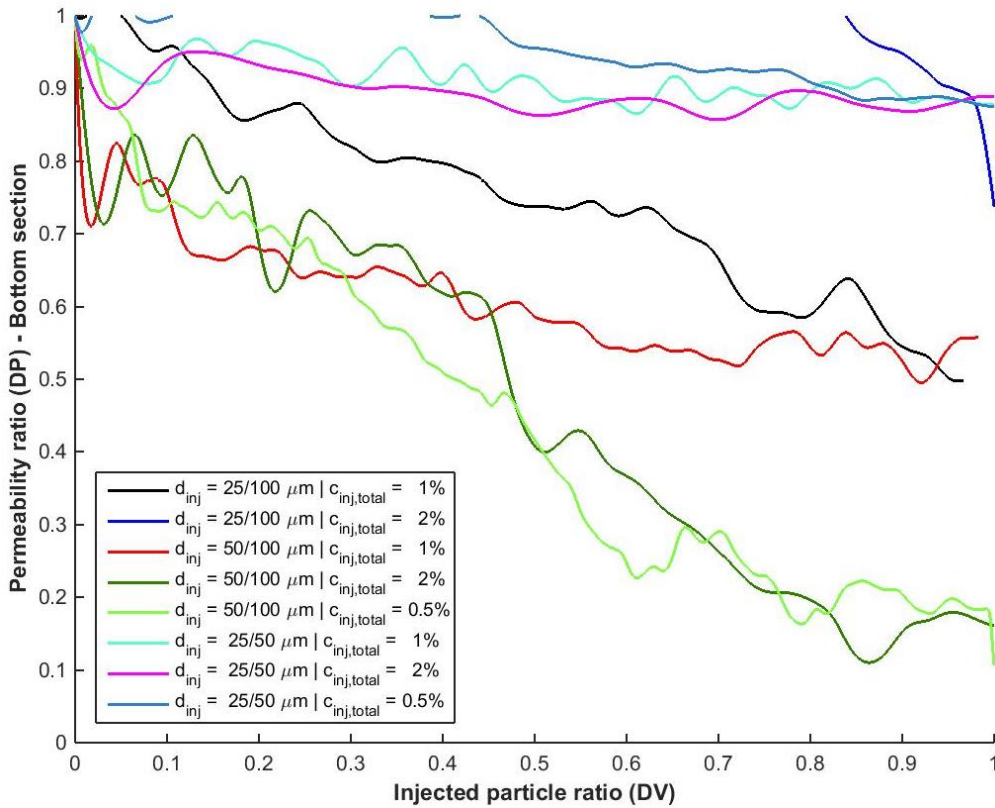
Figure 4 - 22: Bottom section permeability ratio for flow rate = 40 cc/min. DP is normalized permeability.

55

Though the case of the smallest sized particles (experimental case R – 25/50 µm injected particles) shows a very small change in permeability, the same profiles cannot be identified in the bottom section of the core (Figure 4 - 22).

The experimental case with the two biggest sized particles (experimental case F – 50/100 µm injected particles) shows the maximum decline, showing a linear decrease in permeability over time.

4.2.3.2. Flow rate 60 cc/min

Again, two prominent profiles can be observed in Figure 4 - 23 below. The first profile, for experimental set R (25/50 µm injected particles), shows a rapid decline in the permeability initially. It remains fairly constant after 0.1 DV at ± 0.7 normalized permeability. The second prominent profile shows an exponential decay in permeability to reach ± 0.05 normalized permeability by the end of injection. This profile is showed for the other two experimental cases. An outlier in this instance is case B6020 (q = 60 cc/min and total injection concentration = 2%) which shows a two separate linear decreases, changing gradient at 0.5 DV.

Overall, this figure is quite similar to Figure 4 - 21 in appearance implying that flow rate does not have much effect in the top zone.

Figure 4 - 24 shows the permeability in the bottom section of the core. The maximum permeability drop observed is at 40%, and that is for the two largest sized particles (experimental set F – 50/100 µm injected particles). The cases show a smaller change in porosity, on the order of 20%. This implies that set F has a deeper penetration in the core amongst all the cases.

4.2.4. Total injection particle concentrations

Three concentrations (0.5%, 1% and 2% by weight) of injected particles were chosen for the experiments
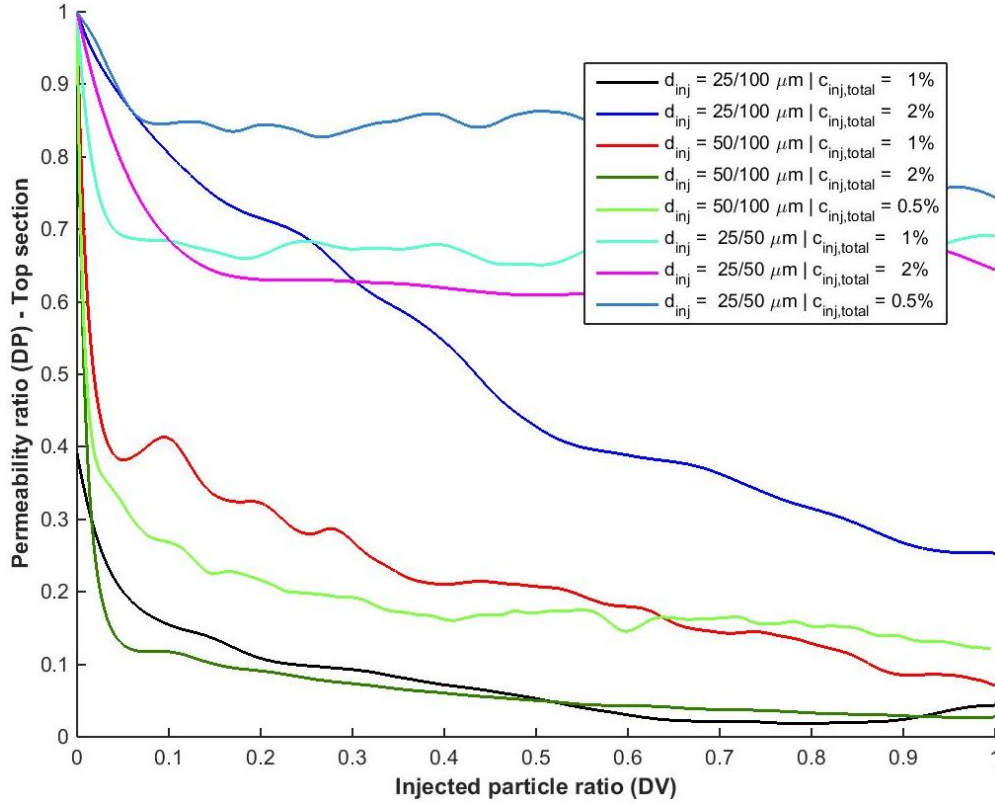
Figure 4 - 23: Top section permeability ratio for flow rate = 60 cc/min. DP is normalized permeability.
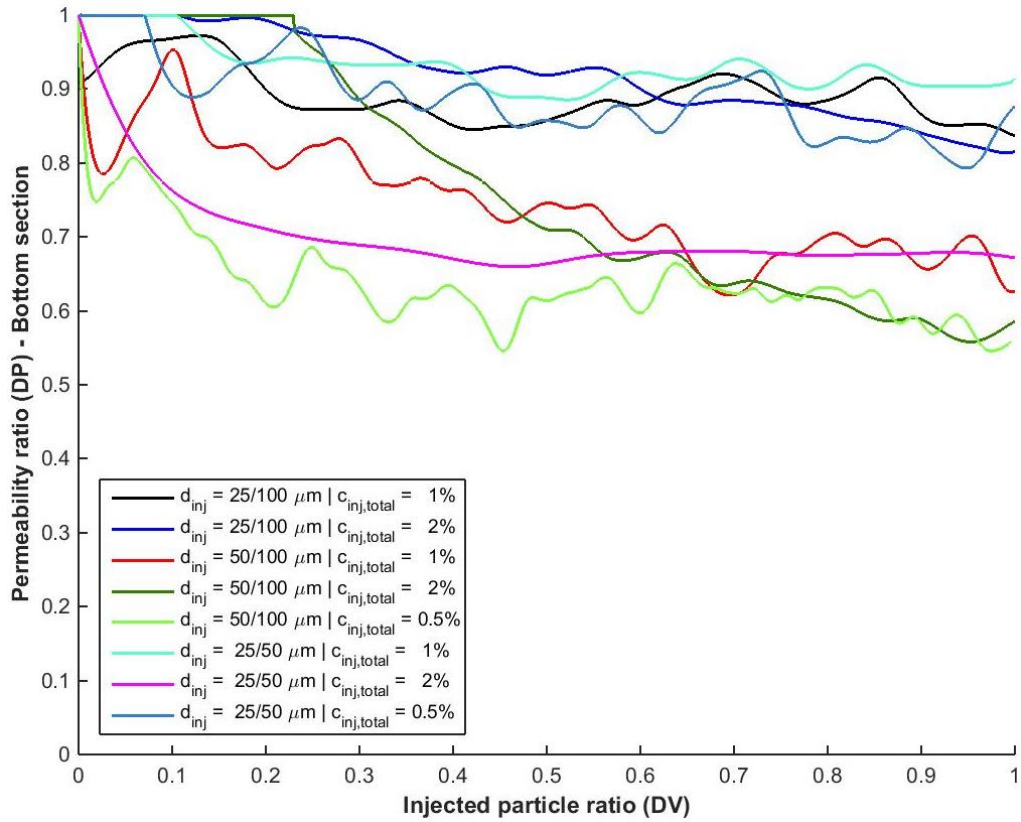
Figure 4 - 24: Bottom section permeability ratio for flow rate = 60 cc/min. DP is normalized permeability.
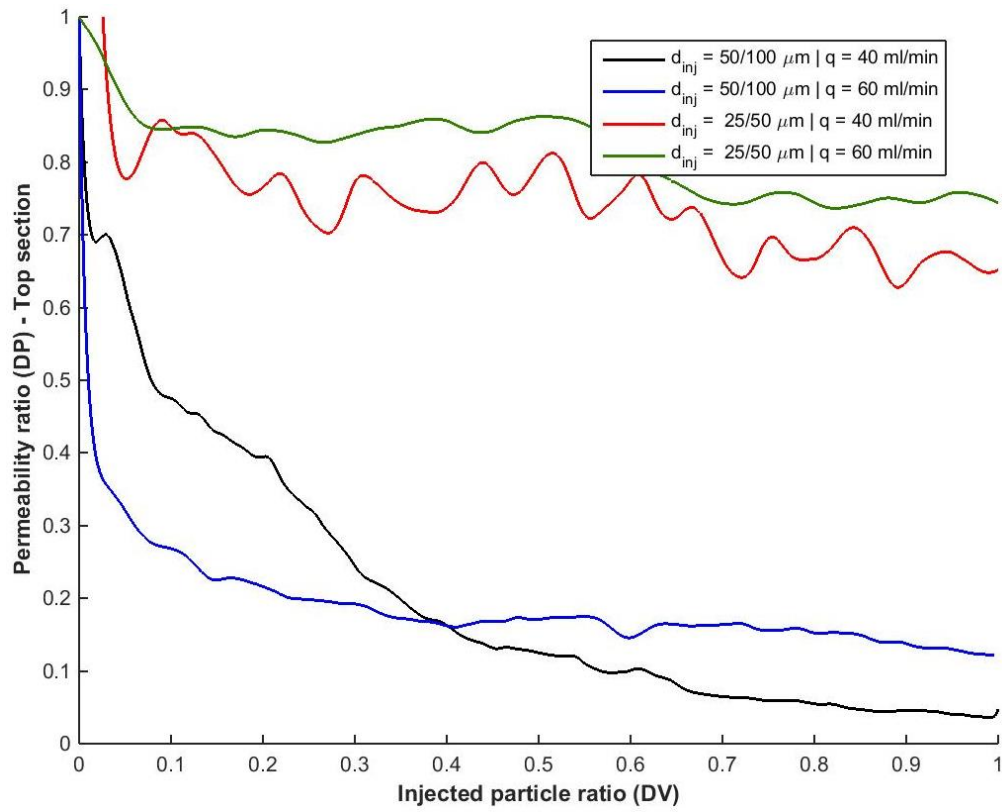
Figure 4 - 25: Top section permeability ratio for total injection concentration = 0.5%. DP is normalized permeability.
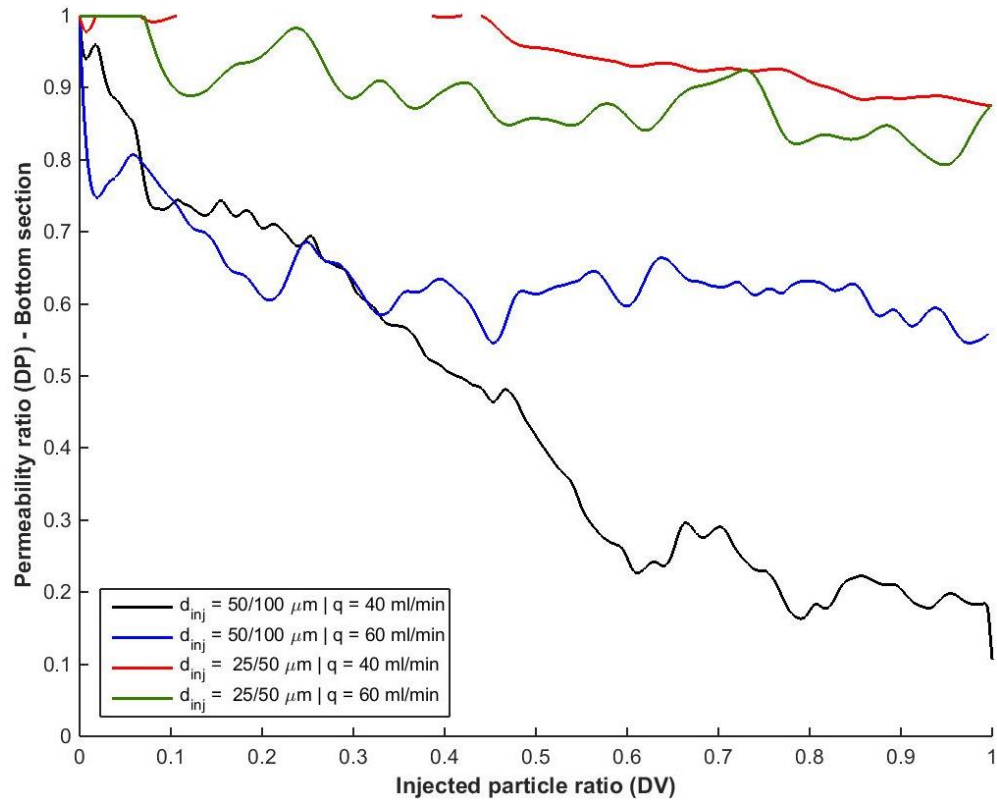
Figure 4 - 26: Bottom section permeability ratio for total injection concentration = 0.5%. DP is normalized permeability.
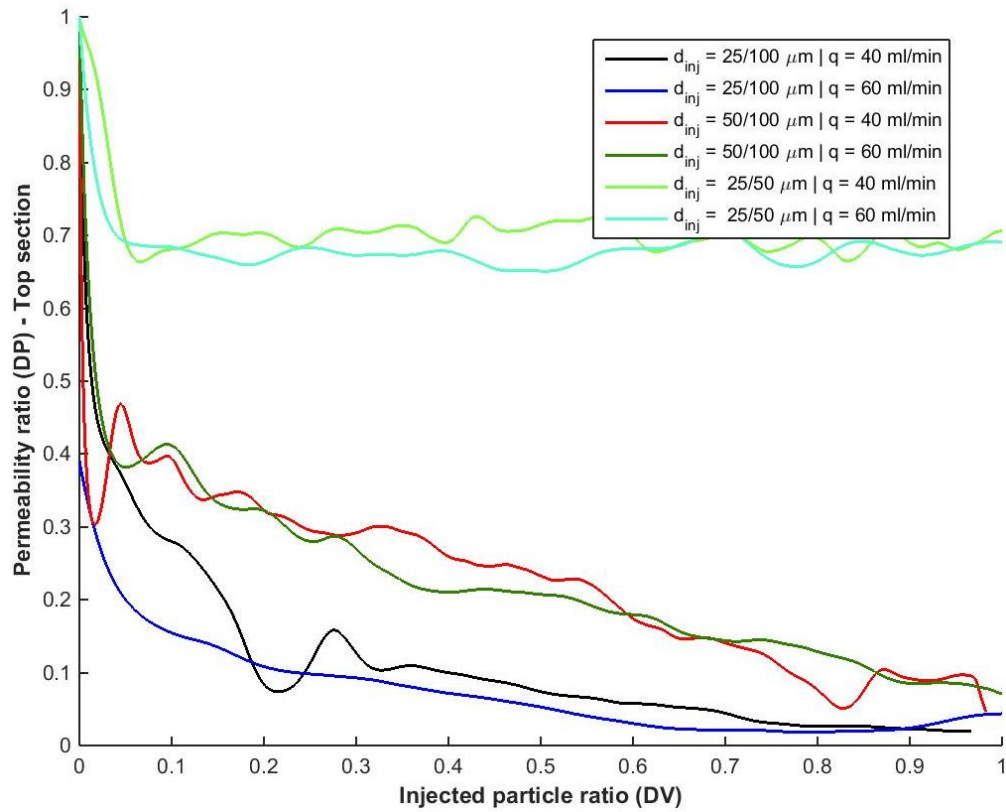
Figure 4 - 27: Top section permeability ratio for total injection concentration = 1%. DP is normalized permeability.
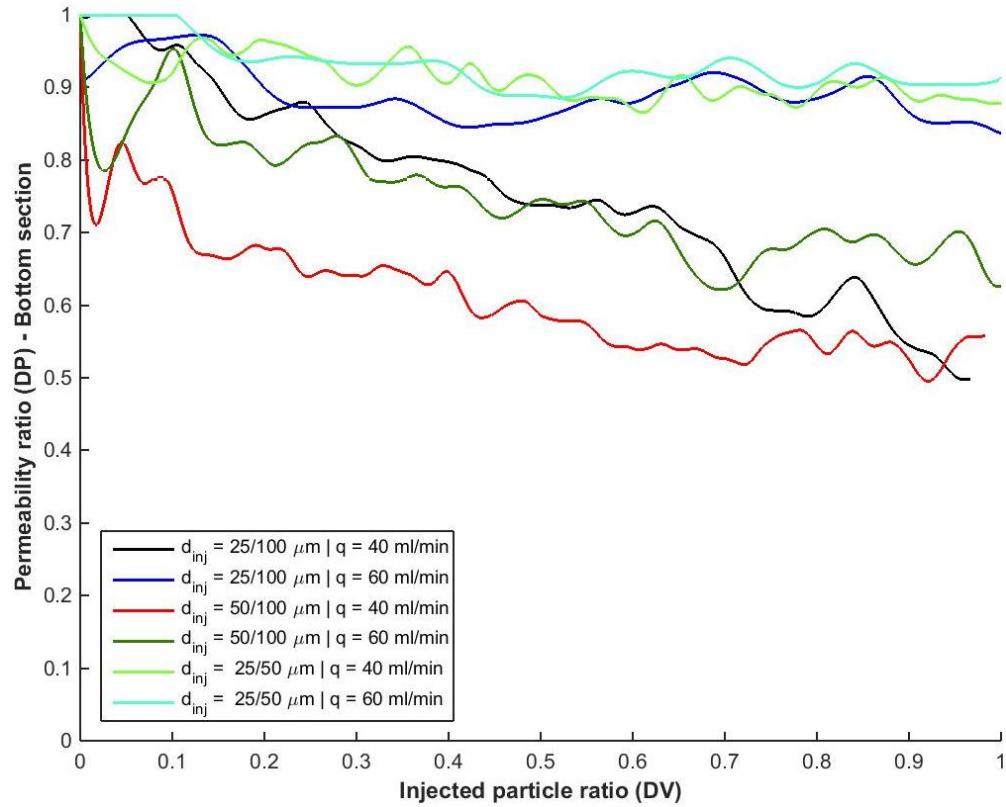
Figure 4 - 28: Bottom section permeability ratio for total injection concentration = 1%. DP is normalized permeability.

4.2.4.1. Total concentration 0.5%

Two distinct profiles are observed in Figure 4 - 25. The largest sized particles (experimental case F – 50/100 μm injected particles) show an exponential decay in permeability while the smallest sized particles (experimental case R – 25/50 μm injected particles) shows an initial quick drop in permeability to 0.85 normalized permeability, and then a linear slow drop to ± 0.7 normalized permeability during the course of the injection.

The bottom section (Figure 4 - 26) shows a similar behavior. Experimental case F shows a larger drop in permeability. Case F4005 shows a linear decrease in permeability while F6005 shows a large drop initially for 0.1 DV, and then a gradual fall during the course of the flooding. Experimental case R again shows a small change in permeability, following a gentle linear profile.

4.1.4.2. Total concentration1%

Two prominent profiles can be identified in Figure 4 - 27 above. The first profile shows a small decline in the permeability for the first 0.05 DV, and then remains constant at ± 0.7 normalized permeability. This profile is exclusively shown by the experimental set R (25/50 μm injected particles). The second prominent profile shows an exponential decay in permeability to reach ± 0.05 normalized permeability by the end of injection. This profile is showed for the other two experimental cases.

Figure 4 - 28 shows the change in permeability in bottom section of the core. All cases show a small change in permeability. The experimental case with the two smallest sized particles (experimental case R – 25/50 μm injected particles) shows almost no decline in permeability. The other two cases show a gradual linear decrease in permeability, reaching a minimum value of 0.6 normalized permeability over the course of injection.
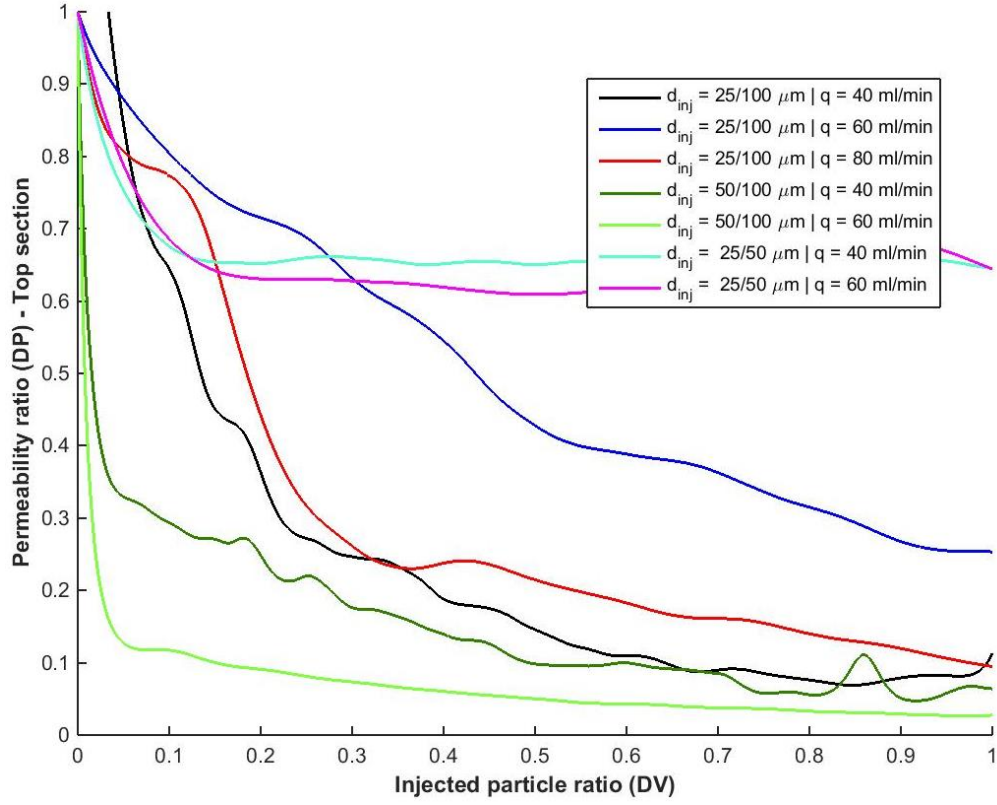
Figure 4 - 29: Top section permeability ratio for total injection concentration = 2%. DP is normalized permeability.
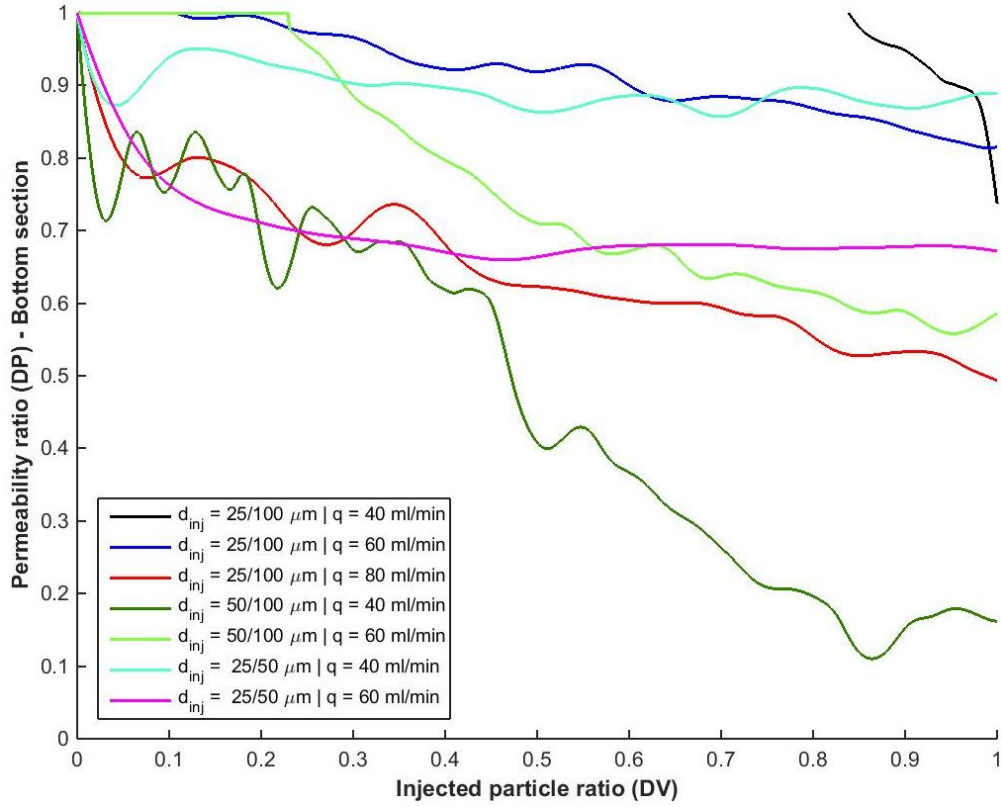
Figure 4 - 30: Bottom section permeability ratio for total injection concentration = 2%. DP is normalized permeability.

4.1.4.3. Total concentration 2%

Two prominent profiles can be seen in Figure 4 - 29.

The first shows no or slight changes in permeability over the course of the experiment and consists of experiments from set R (25/50 µm injected particles). The minimum value observed for these cases is 0.6 normalized permeability. The second profile shows an exponential decay and reaches values of ± 0.01 normalized permeability. Case B6020 is an outlier and shows a steady linear decline in permeability. These profiles are quite similar to Figure 4 - 27.

4.3. Discussion

This section compares the effects of different particle size on the deposition profile, and then moves to see the effect of flow rate on the profiles.

4.3.1. Size effects

4.3.1.1. Experimental case R (25/50 µm particles)

The experimental set consisting of the two smallest sized particles (experimental set R - 25/50 µm particles), shows less than 1% loss in porosity (Figure 4 - 7) for all values of flow rate and concentrations. The same is observed for the permeability profiles in the top (Figure 4 - 19) and bottom sections of the column (Figure 4 - 20).

This implies that the size of the particles are smaller than the capture sites, and the particle falls through without getting strained. The size of the pore throat can be estimated using the Pittman equation (Equation 4.2) for a case above with an average permeability of 100 Darcy and porosity of 41.6%.

$$\log R50 = 0.778 + 0.626 \log k_{air} - 1.205 \log \phi \quad \ldots\ldots\ldots\ldots\ldots\ldots\ldots\ldots \text{(Equation 4.2)}$$

The 50th percentile of pore throat size is *90.6 µm*. This value is almost double the size of the largest particle being injected and hence should allow easy passage to the injection medium. The little change in permeability that we see is due to a thin external filter cake formed around the top of the core. Changing the fluid flow rate and the concentrations seem to have no sizeable effect on the permeability profiles.

An outlier to the data is case R4005 (q = 40 cc/min and total injection concentration = 0.5%) with a large initial drop in porosity but no change in top section permeability. Since each of the bead packs are individually sintered, the bead pack used for R4005 has a different value of permeability (225 Darcy with the same porosity). This leads to a slightly different pore throat distribution and hence different sizes of the capture sites at the surface of the core. This ultimately results in slight changes in the final porosity profile for the case R4005. The top zone shows no difference in the permeability profile from the other cases for the same injected particle sizes, but the lower zone shows a delayed start in the permeability change (particle deposition starts at roughly 0.4 DV). This implies that all the injected particles that are of size larger than the capture sites are caught at the top zone, and the smaller sized particles filter through. These are unable to be retained, or even if retained, they cause no change in the permeability profile as equally viable alternate flow paths are available.

4.3.1.2. Experimental case B (25/100 µm particles)

For experimental set B (25/100 µm injected particles), a logarithmic profile (Figure 4 - 4) is observed for the porosity. In addition, the top section of the core (Figure 4 - 15) shows a rapid decline in the permeability ratio. This is complemented by visual observation of an external filter cake formed at the injection face. The lower section of the core shows a minor decrease in the final porosity, which is complemented by a lower change in permeability (Figure 4 - 16).

The external filter cake is expected to be significant for this experimental set as the mean size of the larger injected particle is greater than pore throat value deduced from the Pittman equation above (100 µm compared to 90.6 µm).

The concentration does not seem to play an important role in the porosity profile, but a disparity is observed between the permeability profiles of the top section at different concentrations. The difference is quite significant at q = 60 cc/min (Figure 4 - 23), with the final permeability difference being ±0.25 normalized permeability for the two cases. Going from 1% to 2% also changes the extent of damage caused by different flow rates. At 1% total concentration, 40 and 60 cc/min cause almost the same damage in the top section of the core. The difference in the damage is significantly increased when the total concentration increases to 2%. 60 cc/min now causes almost double the damage caused by 40 cc/min. This case is reversed in the bottom

section of the core, where more damage is seen at 1% with 40 cc/min, almost three-fold the damage caused by 60 cc/min.. Increasing the total concentration to 2% neutralizes the effect of flow rate in the bottom section, and similar permeability values are observed at the end of the flow period.

Another interesting point to note is the similarity in case B4010 (q = 40 cc/min and total injection concentration = 1%) and case B6020 (q = 60 cc/min and total injection concentration = 2%). A visual observation shows the similarity in data, and a Pearson's correlation yields a value of 0.9998. But moving onto the permeability plots a significant difference can be seen in the permeability profiles in the top and bottom zone. As suggested before, it is likely that the injected particles in case B4010 (q = 40 cc/min and total injection concentration = 1%) plugged the vital flow path resulting in a drastic fall in permeability compared to case B6020 (q = 60 cc/min and total injection concentration = 2%), even though the final porosity value is almost identical.

4.3.1.3. Experimental case F (50/100 µm particles)

For the largest particle sizes (experimental set F – 50/100 µm injected particles), a negative exponential porosity profile (Figure 4 - 5) is observed. The large initial decline in porosity is congruous with the external filter cake formed at the top of the core (Figure 4 - 6), as was also observed in experimental set B (25/100 µm injected particles).

The shape of the porosity plot is quite similar to the profile observed for experimental set B (25/100 µm injected particles), bar the final porosity values which are higher by 3 – 4%. This difference can be explained by the fact that experimental set has 50 µm as the smallest injected particle compared to 25 µm for experimental set B. The chances of 50 µm being entrapped at the top the core (i.e. the filter cake) by size exclusion are higher than those of 25 µm. More trapped particles leads to lesser particles penetrating the core and hence less chances of deposition inside the core. But since the size of injected particles is greater for experimental set F, the chances of it blocking out vital flow paths is comparatively higher. Hence it results in a smaller change in porosity but a drastically larger difference in the top and bottom zone permeabilities (Figure 4 - 15 and Figure 4 - 17).

Like the case B6010 (q = 60 cc/min and total injection concentration = 1%), case F4020 (q = 40 cc/min and total injection concentration = 2%) also shows a decline in the porosity value after the 30 mm mark (Figure 4 - 31). The fall is smaller for the larger sized beads (5% compared to 8% for experimental set B), implying less penetration of the small particles at that point. The top zone of these two cases are show a similar drop in permeability in the early times followed by a similar permeability ratio (± 7 normalized permeability) at the end of the injection. But the difference in the bottom zone permeability profile is remarkable. Permeability for case B6010 cycles at the higher ends of the permeability ratio (Figure 4 - 31), while the permeability for the case F4020 drops continuously to 0.17 normalized permeability by the end of the injection phase. Even though the porosity reduction is greater for B6010 in the latter part of the core, the permeability reduction is lesser. This can be attributed to the small size of the injection particle, which can occupy pore space, and yet not hinder flow.
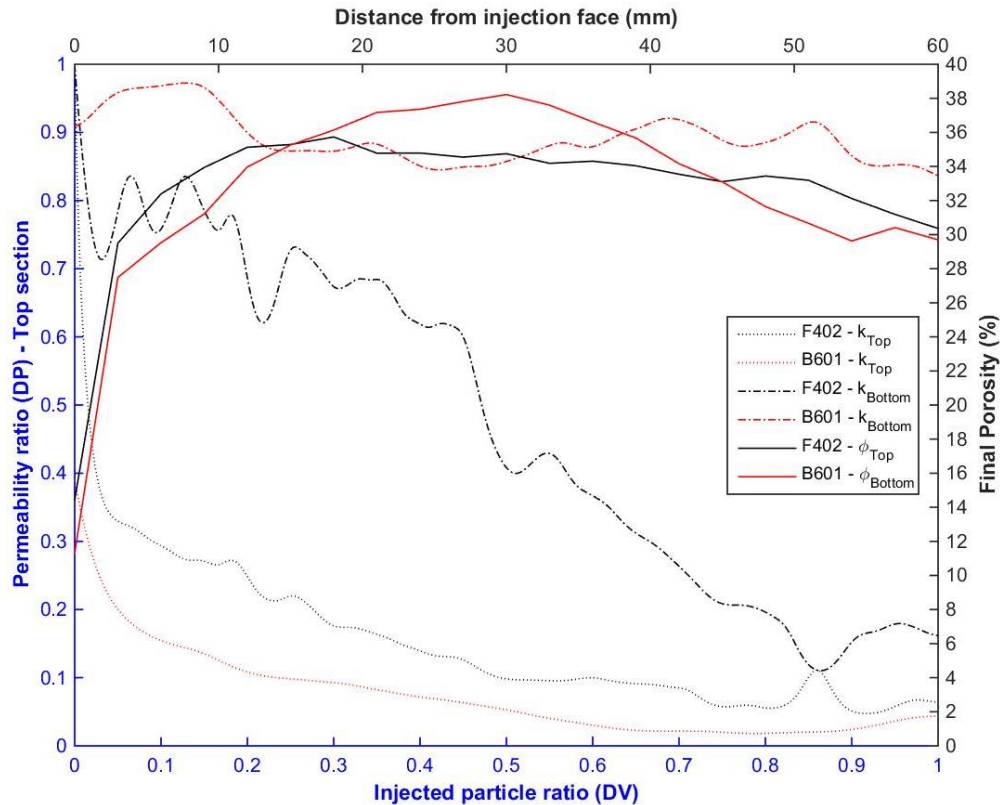
Figure 4 - 31: Comparison of top zone permeability, bottom zone permeability and final porosity for cases F4020 and B6010. DP is normalized permeability.

Another intriguing observation is the relationship between F6005 (q = 60 cc/min and total injection particle concentration = 0.5%) and F4005 (q = 40 cc/min and total injection particle concentration = 0.5%). For the top and bottom zone, the permeability is initially greater for the 60 cc/min flow rate. But as time progresses, 40 cc/min causes more damage and resultantly has a lower permeability ratio at the end of injection (0.35 normalized permeability lower). The turnaround happens at 0.40 DV for the top zone and at 0.32 DV for the bottom zone. Interestingly the porosity profile (Figure 4 - 32) shows similar porosity values at 20 mm and at the end of the core.

For the experimental set F (50/100 µm injected particles), the lower flow rate consistently leads to a greater change in the final porosity (i.e. lower final porosity). This is also observed for the experimental set B (25/100 µm injected particles).
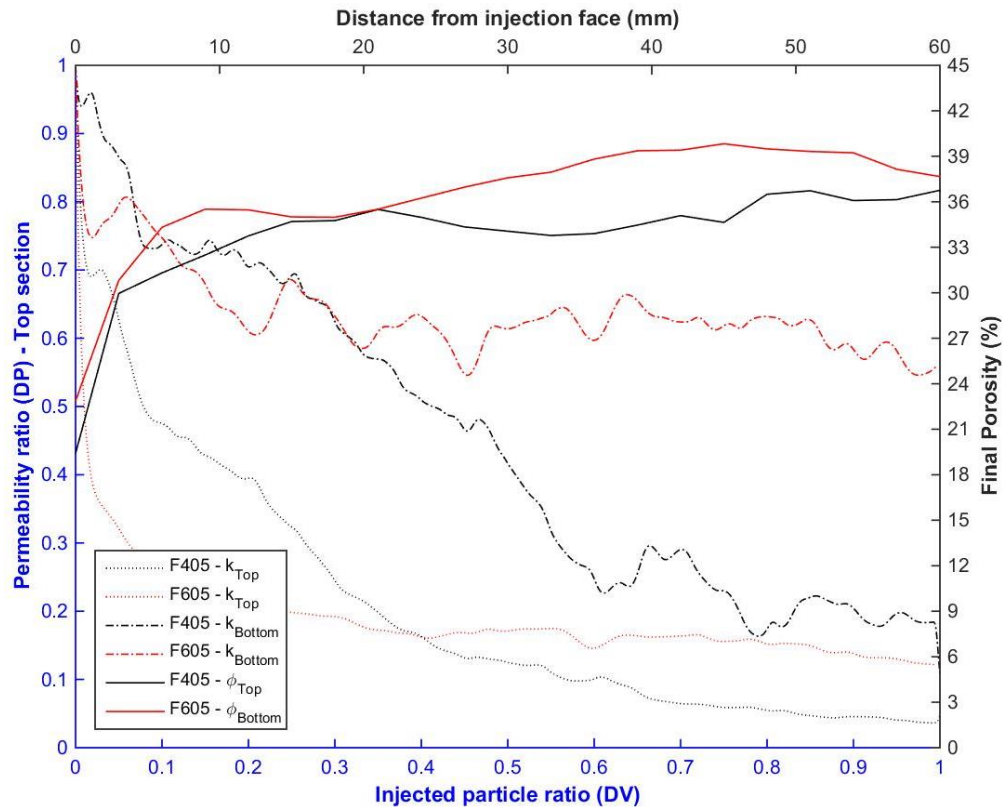
Figure 4 - 32: Comparison of top zone permeability, bottom zone permeability and final porosity for cases F4005 and F6005. DP is normalized permeability.

Meanwhile experimental set R (25/50 µm injected particles) shows the inverse relationship, where a lower porosity leads to a higher final porosity. A point to note is that, for experimental set R, the porosity changes are so small that they lie within the error limits of the porosity calculation[1].

4.3.1.4. Summary of different particle size distributions

In summary, experimental set R (25/50 µm injected particles) shows no significant change in the porosity and permeability over the injection period. Experimental set F (50/100 µm injected particles) shows the most change in permeability, while the second most change in porosity. Experimental set B (25/100 µm injected particles) shows the most change in porosity, while the second most change in permeability.

4.3.2. Rate effects

Experimental set R (25/50 µm injected particles) shows 0.5% total injection concentration to have the lowest damage in top zone at 40 cc/min. This is followed by 1% and 2% respectively. The same trend is observed for a flow rate of 60 cc/min. Experimental set B (25/100 µm injected particles) have the inverse relationship. 2% total injection concentration does less damage as compared to 1% at both the flow rates. Experimental set F (50/100 µm injected particle) shows that at the lower flow rate, 2% total injection concentration does the least damage and 0.5% does the most damage. This is reversed when the flow rate is increased to 60 cc/min.

A possible explanation is that the low flow rate applies less pressure on the external filter cake, and hence does not cause much damage to it. This results in significantly filtering out the larger particles. A higher concentration causes the filter cake to build up quickly, and hence the chances of particles travelling and depositing inside the core are reduced. On the other hand, a lower concentration allows more particles to slip through.

---

[1] – Error limit on the CT scan is 10 CT numbers. Using Equation 4.1 results in a 0.404% porosity change.

$$\phi_{reduction} = \frac{(CT\ Number)_{after} - (CT\ Number)_{before}}{(CT\ Number)_{glass} - (CT\ Number)_{DI\ water}} = \frac{10}{2500 - 25} \times 100 = 0.404\%$$

Increasing the flow rate to 60 cc/min applies an extra stress on the external filter cake, which leaks particles inside the core. Fingers have been created in the external filter cake which give access to the top of the core. A higher concentration at that point leads to higher intrusion of particles and hence a greater reduction in permeability.

Permeability profiles for the lower section of the core show significantly less damage. Damage relationships at each flow rate for each experimental set show the same permeability reduction trend. A unique thing observed for experimental set F (50/100 µm injected particles) at both fluid flow rates was that a similar damage at end of injection was observed at 0.5% and 2% total injection concentration. For 40 cc/min, the permeability ratio profiles for the two concentrations are closely related. The case is significantly different for the higher flow rate, where 2% total injection concentration shows no drop in permeability until 0.23 DV. It then falls linearly to 0.62 normalized permeability. For the higher flow rate, the drop is more constant and at a gentler pace to reach a final value of 0.64 normalized permeability.

Chapter 5: Conclusions and future work

Filtration and surface depositions are two main mechanisms of formation damage by fines migration. Experiments above point to the following conclusions:

1. Injected particle size plays the chief role in formation damage. Larger sized particles have a higher damage as compared to the smaller sized particles. If the injected particle size is very low, the flow rate and concentration have no sizeable effect on the porosity and permeability.

2. Size exclusion (entrapment) causes a larger loss in formation permeability as compared to surface deposition.

3. External filter cake significantly influences the internal filter cake and hence the formation damage. A higher flow rate can cause fingering in the external filter cake and hence change the expected change in porosity and permeability.

4. Small core can have end effects and this can significantly alter the porosity and permeability measurements.

Some ideas to consider for future work, some of which are currently work under progress, are:

1. Model and predict the formation damage for a tighter and longer cores.

2. Fabricate cores similar to vuggy carbonates and model and predict their porosities for different heating profiles.

3. Understand and model the effect of backflow on recovered permeability.

4. Investigate the formation damage in a horizontal core.

5. Measure and quantify the effluent concentrations.

Appendix A – Data Sheets

MO-SCI Specialty Products, L.L.C.
A Subsidiary of MO-SCI Corporation
4040 HyPoint North
Rolla, MO 65401
Telephone: 573-364-2338
Fax: 573-364-9589

GL-0191
DATA SHEET

Appearance

Solid soda-lime glass beads of various colors.

Chemical Composition (by weight)

Silica (SiO_2)	65~75%
Aluminum oxide (Al_2O_3)	0~5%
Calcium oxide (CaO)	6~15%
Magnesium oxide (MgO)	1~5%
Sodium oxide (Na_2O)	10~20%
Iron Oxide (Fe_2O_3)	<0.8%

Physical Properties

Specific Gravity	2.5 (g/cm^3)
Bulk Density of Dry Beads	1.3 g per cm^3 (77 lbs/ft^3)
pH in water @ 25°C	7.8
Softening Temperature	650°C
Thermal Conductivity	0.9-1.3 W/m.K
Coefficient of Thermal Expansion	90×10^{-7}/°C (30-300° C)
Compression Strength	29 kg/mm^2 (39,875 psi)
Vickers Hardness	550 kg/mm^2 (756,250 psi)
Mohs Hardness	6-7
Index of Refraction	1.51(n_D)

Applications

Typical applications of GL-0191 glass spheres include: spacer for gauge control, thermal expansion reduction filler for adhesives and polymers.

Figure A - 1: Data sheet for glass beads

70

S.No.	Author	Type	Size (μ)	Type	Size (μ)	Ratio
1	Sakivadivel	Styron	900	Plastic Ball Spherical	12500	14
			1400		12500	9
2	Maroudas	Spherical Polysterene	125	Model Filter Chanels	3000	24
			390		3000	8
3	Leclerc	Pollen	32	Glass Sphere	500	16
					100	3
4	Herzig	Pollen	31	Glass Sphere	500	16
5	Edwards-Monke	Clay	1	Sand	350	350
6	Heertjes-Lerk	Fe(OH)2	0.1	Glass Sphere	540	5400
					650	6500
					780	7800
			10		540	54
					650	65
					780	78
7	Jorden	Clay	1	Gravel	5500	5500
8	Borchardt, O'Melia	Algae	15	Sand	320	21
					400	27
					525	35
			60		320	5
					400	7
					525	9
9	Eliassen	Fe(OH)3	6	Sand	460	77
			20		460	23
10	Herzig	Alumina	4	Glass Sphere	500	125
11	Ling	Diatomite	10	Sand	350	35
					550	55
12	Smith	Clay	5	Sand	600	120
13	Elimelech; O'Melia	Polysterene	0.046	Glass Bead	200	4348
			0.378		200	529
			0.753		200	266
			0.046		400	8696
			0.378		400	1058
			0.753		400	531
14	Kretzschmar	Monodisperse Polysterene	0.2	Glass Bead	375	1875
15	Phenrat	Reactive Iron (Bimodal)	0.045	Glass Bead	300	6667
			0.325		300	923

S.No.	Author	Type	Size (μ)	Type	Size (μ)	Ratio
16	Saleh	Reactive Nano-Iron (Polymodal)	0.146	Sand	300	2055
			0.066		300	4545
			0.178		300	1685
			0.212		300	1415
17	Vigneswaran	Pollen	26	Sand	2500	96
			12.8		2500	195
18	Mackrle	Fe(OH)2	10	CaCO3	1330	133
19	Ives	Chlorella	0.65	Sand	540	831
			0.44		700	1591
20	Robinson	Quartz Powder	0.57	Anthracite	770	1351
			0.35		1020	2914
21	Gruesbeck; Collins	Glass Bead	7.5	Sand Pack	274	37
22	Bailey; Boek	CaCO3	3.9	Sandstone Core	350	90
			17		350	21
			29		350	12
			41		350	9
			117		350	3
		Barite	22		350	16
23	Gruesbeck; Collins	CaCO3	8	Unconsolidated Sands	840	105
					2000	250
24	Hongyu / Maryam	Glass Bead	100	Glass Bead	1000	10
25	Proposed Work	Glass Bead	50	Glass Bead	1000	20
			25		1000	40

Table A - 2: Ratio of mass of effluent to injected particles (F4005 means q = 40 cc/min and total injection concentration = 0.5%)

Experiment case	$\dfrac{Mass\ of\ effluent\ particles}{Mass\ of\ injected\ particles}$	Experiment case	$\dfrac{Mass\ of\ effluent\ particles}{Mass\ of\ injected\ particles}$
F4005	0.68	B4010	0.65
F6005	0.74	B6010	-
F4010	0.78	B6020	0.70
F6010	0.84	B8020	-
F4020	0.63		
F6020	0.70		

Appendix B – MATLAB routines for processing CT data

```matlab
function [rawdata_3D, image_num] = Pile_to_mat(file_name)
s = dir (file_name);
filesize = s.bytes;
image_num = floor (filesize/(1024*522))+1;
fid = fopen (file_name);
rawdata_Double = fread (fid,512*512*image_num,'int16','ieee-le');
rawdata_integer = cast(rawdata_Double,'int16');
rawdata_3D2 =rawdata_integer;
rawdata_3D = reshape(rawdata_3D2,512,512,image_num);
temp = 'slice';
dir_name = strcat(file_name);

for i=1:image_num;

    slice = rawdata_3D(:,:,i);
    mkdir(['MAT\',num2str(file_name(end))])
    name = strcat( num2str(file_name(end)),'\',temp,int2str(i),'.mat');
    save([cd,'\MAT\',name],'slice');

end
```

```matlab
% The purpose of this program is to cut a circle from each image of a pile
% file.
% The user is asked to enter the number of images existing in the pile file
% Then the user is asked to pick three points on the circle of interest for
the first image.
% calculated radius for this image will be considered as constant radius for
all images.
% The program will ask the user to modify the position of the circle for
% every image.
% each slice is reduced to a (2*rad) by (2*rad) matrix of ct data that may
have different positions
% in each slice. Then a mask is created that masks out the data outside the
circle.
% finally the CT data inside the circle of interest of each image is saved
% in a new mat file.

% the number of images is calculated in pile_to_tif and pile_to_mat
% programs

num_slices=input('please enter the number of slices------>  ');
top_sand=input('please enter the image number related to top sand----->');

% each original mat file is loaded and the ct data inside the circle of
% interest is saved in a new mat file

 for ii=top_sand:num_slices
```

```matlab
    % for the first image the radius and center position of the circle of
    % interest will be specified.

    if ii==top_sand

        % Load the file
    str_ii = num2str(ii);
    com=strcat('Pick slice',str_ii);
    [filename, pathname] = uigetfile('*slice*.mat', com);
    totalname = [pathname filename];
    load(totalname);
    evalstr=('slice_w=slice;');
    eval(evalstr);
    clear('slice');

%          creates the a new directory processes
    newpath = [pathname,'processed'];
    mkdir(newpath);
    dir_name=strcat(pathname,'processed/')

        % display image
        figure
        hold on
% choose three points on the edge, draw the circle that passes through the
% points
I_p = [];
while (size(I_p,1) ~= 3)
    clear x_r y_r
    h1 = imshow(slice_w,[1000 1400]);
    title('First Slice');
    h = questdlg('Choose three points on the edge of the circle (last point
is with a right click)','Circle Selection','OK','OK','OK');
    [x_r(:,1),y_r(:,1),P] = impixel;
    I_p = [x_r y_r];
    if size(I_p,1) == 3
        [circ1,circ2,circ3] = circle_eq(I_p(1,:),I_p(2,:),I_p(3,:));
        circ(1) = round(circ1);
        circ(2) = round(circ2);
        circ(3) = round(circ3);
        I_cen = [circ(1) circ(2)];% center
        rad = circ(3); % radius (this will be fixed)
        circ_pixels = circlepoints(I_cen(1),I_cen(2),rad); % find
circle_pixels
        hold on
        % now display circle
        h2 = plot(circ_pixels(:,1),circ_pixels(:,2),'g.','markersize',2);
        title_str = ['x = ' num2str(circ(1)) ...
            '; y = ' num2str(circ(2)) ...
            '; rad = ' num2str(circ(3))];
        title('title_str')
    else
        errordlg('Need three and only three points','Error');
    end
end

% now check if the user wants it adjusted
```

```matlab
reply = questdlg('Circle Check','Circle OK?','Yes','No','No');

while strcmp(reply,'No')
    prompt = {'Adjust x-center?','Adjust y-center?', 'Adjust radius?'};
    dlg_title = 'Adjust circle?';
    num_lines = 1;
    def = {num2str(I_cen(1)),num2str(I_cen(2)),num2str(rad)};
    answer = inputdlg(prompt,dlg_title,num_lines,def);
    I_cen(1) = str2num(char(answer(1)));
    I_cen(2) = str2num(char(answer(2)));
    rad = str2num(char(answer(3)));
    h1 = imshow(slice_w,[750 1500]); title('First Slice');
    hold on
    circ_pixels = circlepoints(I_cen(1),I_cen(2),rad); % find circle_pixels
    h2 = plot(circ_pixels(:,1),circ_pixels(:,2),'g.','markersize',2);
    reply = questdlg('Circle Check','Circle OK?','Yes','No','No');
end

    else
    str_ii = num2str(ii);
    filename=strcat('slice',str_ii,'.mat');
    totalname = [pathname filename];
    load(totalname);
    evalstr=('slice_w=slice;');
    eval(evalstr);
    clear('slice');

% display images from 2 to num_slices

tittle_slice=strcat('slice',str_ii);
h3 = imshow(slice_w,[750 1500]);
title(tittle_slice);
hold on
h4 = plot(circ_pixels(:,1),circ_pixels(:,2),'g.','markersize',2);
reply = questdlg(' Check circle position','Circle OK?','Yes','No','No');

% Adjust the center of the circle

while strcmp(reply,'No')
    prompt = {'Adjust x-center?','Adjust y-center?'};
    dlg_title = 'Adjust circle?';
    num_lines = 1;
    def = {num2str(I_cen(1)),num2str(I_cen(2))};
    answer = inputdlg(prompt,dlg_title,num_lines,def);
    I_cen(1) = str2num(char(answer(1)));
    I_cen(2) = str2num(char(answer(2)));

    h1 = imshow(slice_w, [750 1500]); title('First Slice');
    hold on
    circ_pixels = circlepoints(I_cen(1),I_cen(2),rad); % find circle_pixels
    h2 = plot(circ_pixels(:,1),circ_pixels(:,2),'g.','markersize',2);
    reply = questdlg('Circle Check','Circle OK?','Yes','No','No');
end

    end
```

```matlab
    % make the binary mask file
    mask = int16(imcircle(2*rad+1));
    BW_mask = (mask == 1); %binary mask

    % filter the silices
    slice_w=medfilt2(slice_w, [5 5]);

    % throw out the edges and mask the slice
    x_range = I_cen(1)-rad : I_cen(1)+rad;
    y_range = I_cen(2)-rad : I_cen(2)+rad;
    slice_m = slice_w(y_range,x_range).*mask;
    I_cen_vec(ii,:)=I_cen;% save the center position of each slice
    % save data
    outfile_name = strcat(dir_name,'slice',str_ii,'_modified','.mat');

    save(outfile_name, 'slice_m', 'I_cen','rad');
    clear slice*
end

 % save the position and radius of the center for all imgaes in a mat file
  outfile_name = strcat(dir_name,'Circles_position','.mat');
  save(outfile_name,'I_cen_vec','rad');
```

```matlab
function [x_center y_center radius]=circle_eq (P1, P2, P3)
m1=-1*(P1(1)-P2(1))/(P1(2)-P2(2));
m2=-1*(P3(1)-P2(1))/(P3(2)-P2(2));
x_center=(m1*(P1(1)+P2(1))/2-m2*(P2(1)+P3(1))/2+(P3(2)-P1(2))/2)/(m1-m2);
y_center=(P1(2)+P2(2))/2+m1*(x_center-(P1(1)+P2(1))/2);
radius=sqrt((P1(1)-x_center)^2+(P1(2)-y_center)^2);
end
```

```matlab
function y = imcircle(n)

% Draw a solid circle of ones with diameter n pixels
% in a square of zero-valued pixels.
% Example: y = imcircle(128);

if rem(n,1) > 0,
   disp(sprintf('n is not an integer and has been rounded to
%1.0f',round(n)))
   n = round(n);
end
if n < 1      % invalid n
   error('n must be at least 1')
elseif n < 4 % trivial n
   y = ones(n);
elseif rem(n,2) == 0,   % even n
   DIAMETER = n;
   diameter = n-1;
   RADIUS = DIAMETER/2;
   radius = diameter/2;
```

```matlab
    height_45 = round(radius/sqrt(2));
    width = zeros(1,RADIUS);
    semicircle = zeros(DIAMETER,RADIUS);
    for i  = 1 : height_45
        upward = i - 0.5;
        sine = upward/radius;
        cosine = sqrt(1-sine^2);
        width(i) = ceil(cosine * radius);
    end
    array = width(1:height_45)-height_45;

    for j = max(array):-1:min(array)
        width(height_45 + j) = max(find(array == j));
    end
    if min(width) == 0
       index = find(width == 0);
       width(index) = round(mean([width(index-1) width(index+1)]));
    end
    width = [fliplr(width) width];
    for k  = 1 : DIAMETER
        semicircle(k,1:width(k)) = ones(1,width(k));
    end
    y = [fliplr(semicircle) semicircle];
else   % odd n
    DIAMETER = n;
    diameter = n-1;
    RADIUS = DIAMETER/2;
    radius = diameter/2;
    semicircle = zeros(DIAMETER,radius);
    height_45 = round(radius/sqrt(2) - 0.5);
    width = zeros(1,radius);

    for i  = 1 : height_45
        upward = i;
        sine = upward/radius;
        cosine = sqrt(1-sine^2);
        width(i) = ceil(cosine * radius - 0.5);
    end
    array = width(1:height_45) - height_45;

    for j = max(array):-1:min(array)
        width(height_45 + j) = max(find(array == j));
    end
    if min(width) == 0
       index = find(width == 0);
       width(index) = round(mean([width(index-1) width(index+1)]));
    end
    width = [fliplr(width) max(width) width];
    for k  = 1 : DIAMETER
        semicircle(k,1:width(k)) = ones(1,width(k));
    end
    y = [fliplr(semicircle) ones(DIAMETER,1) semicircle];
end
```

```matlab
function pts=circlepoints(xCenter,yCenter,radius)
```

```matlab
% pts=circlepoints(xCenter,yCenter,radius)
%This is a simple function that returns the points in a circle with center
%xCenter,yCenter with radius 'radius'
%This is a function intended to return coordinates of a pixel image
%so it will work well only for integer values of xCenter, yCenter and radius
%Suresh Joel, June 24, 2002
if(nargin<3)
    error('Too few arguements');
end
if(rem(xCenter,1)~=0 | rem(yCenter,1)~=0 | rem(radius,1)~=0)
    warning('Increments are by whole numbers and using non-integers might not
produce desired results');
end
x = 0;
y = radius;
p = 1 - radius;
pts=[];
pt=GetPoints(xCenter, yCenter, x, y);
pts=[pts pt];
while(x<y)
    x=x+1;
    if(p < 0)
        p =p + (2*x + 1);
    else
        y=y-1;
        p = p+ (2*(x-y) + 1);
    end
    pt=GetPoints(xCenter, yCenter, x, y);
    pts=[pts;pt];
end

pts=sortrows(pts);
prevsz=length(pts)+1;          %Dummy number to make it go atleast once through
the loop
while(length(pts)~=prevsz)
    prevsz=length(pts);
    n=1;
    while(n<length(pts)),
        if(pts(n,:)==pts(n+1,:))
            pts(n,:)=[];
        end
        n=n+1;
    end
end
function pt=GetPoints(xCenter,yCenter,x,y)
pt(1,:)=[xCenter + x, yCenter + y];
pt(2,:)=[xCenter - x, yCenter + y];
pt(3,:)=[xCenter + x, yCenter - y];
pt(4,:)=[xCenter - x, yCenter - y];
pt(5,:)=[xCenter + y, yCenter + x];
pt(6,:)=[xCenter - y, yCenter + x];
pt(7,:)=[xCenter + y, yCenter - x];
pt(8,:)=[xCenter - y, yCenter - x];

function [] = plot_CT(filename,pathname)
```

```matlab
% plot CT numbers
files = dir([pathname,'*.mat']);
num_slices = length(files) - 1;
% top_sand=input('please enter the image number related to top sand----->');

% each original mat file is loaded and the ct data inside the circle of
% interest is saved in a new mat file

 for ii=top_sand:num_slices

    % for the first image the radius and center position of the circle of
    % interest will be specified.

    str_ii = num2str(ii);

    if ii==top_sand
    % Load the file
    totalname = [pathname filename];
    load(totalname);

    evalstr=('slice_w=slice_m;');
    eval(evalstr);
    clear('slice_m');
    else
    filename=strcat('slice',str_ii,'_modified','.mat');
    totalname = [pathname filename];
    load(totalname);
    evalstr=('slice_w=slice_m;');
    eval(evalstr);
    clear('slice_m');
    end
index=0;
AAA=size(slice_w);

for i =1:AAA(1)
    for j = 1:AAA(1)
        if slice_w(i,j)==0
            index=index;
        else
            index=index+1;
        end
    end
end
    CT(ii)=mean(slice_w(:));
   CT(ii)=CT(ii)*AAA(1)^2/index;

 end
mkdir('CT Number')
 outfile_name = strcat(pathname(1:68),'CT Number\CT_',num2str(pathname(end-
1)),'.mat');
 save(outfile_name,'CT');
```

```matlab
Porosity_calc.m
clear; clc;
%% Hard Data

CT_glass = 2500;
CT_water = 25;

%% Calculations

myFolder = strcat(cd,'\CT Number\');
files = dir([myFolder,'*.mat']);
files = struct2cell(files);
poro = cell(2,2);

for i = 1:length(poro)
    name = files{1,i};
    load([myFolder,name])
    phi = (CT_glass - CT)/(CT_glass - CT_water);        %fraction [0,1]
    poro{i,1} = name(1:end-4);
    poro{i,2} = phi;
end
d_poro = poro{2,2}-poro{1,2};
save diff_poro.txt d_poro -ascii
```

Appendix C – MATLAB routine for processing pressure measurements

```matlab
clear; clc;
%% Constants

psi2atm = 1/14.696;
phi = 0.413;
mu = 0.899;                                    %cP
h = 5.8;                                        %cm
d = 1.415*2.54;                                %cm
Area = d^2 * pi / 4;                           %cm2
q = 80;                                         %cc/min


File = dir('*.lvm');
FILE = File.name;

%Number of measurements
fprintf('Counting number of measurements...\n')
fid=fopen(FILE);
N=-1;
while(~feof(fid))
    fgetl(fid);
    N=N+1;
end
fclose(fid);

%Import data
fprintf('Reading %d measurements:  0%%\n',N)
press=zeros(N,2);
fid=fopen(FILE);
tline=fgetl(fid);
perc=1;
for k=1:N
    tline=fgetl(fid);
    fields=strsplit(tline);
    press(k,1)=str2num(fields{3})/5; % conversion of V to psi
    press(k,2)=str2num(fields{6})/5;
    if k==floor(N*perc/100)
        fprintf('\b\b\b\b\b%3d%%\n',perc)
        perc=perc+1;
    end
end
fclose(fid);
fs=100;
t=(0:N-1)/fs;
PRESS=fft(press);
freq=(0:N-1)/N*fs;

%% Filter
fc=0.005; % manually varied to get the desired output
type='low';
n=4;
[b,a] = butter(n,fc*2/fs,type);
pressf=filter(b,a,press);
```

```matlab
PRESSF=fft(pressf);

%corrections to zero
pressf(:,1) = pressf(:,1);
pressf(:,2) = -pressf(:,2)+0.007;

%Permeability calculation
k1 = q / 60 * mu / Area * h ./ (pressf(:,1) * psi2atm);
k2 = q / 60 * mu / Area * h ./ (pressf(:,2) * psi2atm);

%% Confirmation plot
color1=[0 0.4470 0.7410];
color2=[0.8500 0.3250 0.0980];
xmin = 90; xmax = 1300;

subplot 321
plot(t,pressf(:,1),'color',color1)
xlabel('Time (sec)')
ylabel('Pressure Top (psi)')

subplot 322
plot(t,pressf(:,2),'color',color2)
xlabel('Time (sec)')
ylabel('Pressure Bottom (psi)')

subplot 323
plot(t,k1,'color',color1)
xlabel('Time (sec)')
ylabel('Perm Top (D)')
axis([xmin xmax 0 8000])

subplot 324
plot(t,k2,'color',color2)
xlabel('Time (sec)')
ylabel('Perm Bottom (D)')
axis([xmin xmax 0 8000])

k1norm = k1/k1(fs*(xmin+00));
k2norm = k2/k2(fs*(xmin+00));
k1norm(1:36651) = 1;

subplot 325
plot(t-xmin,k1norm,'color',color1)
xlabel('Time (sec)')
ylabel('Perm Top (D)')
axis([0 xmax 0 1])

subplot 326
plot(t-xmin,k2norm,'color',color2)
xlabel('Time (sec)')
ylabel('Perm Bottom (D)')
axis([0 xmax 0 1])

%% Plot 2
mdot  = str2num(FILE(end-6:end-5))*2.5/100*str2num(FILE(end-4));
```

```matlab
subplot 111
plot((t-xmin)/60*mdot/60,k2norm,'color',color1); hold on;
plot((t-xmin)/60*mdot/60,k1norm,'color',color2)
xlabel('Injected particle ratio')
ylabel('Permeability ratio')
axis([0 1 0 1])
legend('Top','Bottom')

print(['C:\Users\hjk622\Google Drive\Masters Report\Permeability plots\',...
    FILE(1),FILE(end-6:end-4)],'-djpeg');

%% Save data
ktop = k2norm(xmin*fs:end);
kbottom = k1norm(xmin*fs:end);
time = (t(xmin*fs:end)-xmin)/60*mdot/60;
save(['C:\Users\hjk622\Google Drive\Masters Report\Permeability
plots\Data\',...
    FILE(1),FILE(end-6:end-4)],'time','ktop','kbottom');
```

References

Bailey, Louise et al. 2000. "Particulate Invasion from Drilling Fluids." *SPE Journal* 5(04): 412–19.http://www.onepetro.org/doi/10.2118/67853-PA

Barkman, J.H., and D.H. Davidson. 1972. "Measuring Water Quality and Predicting Well Impairment." *Journal of Petroleum Technology* 24(07): 865–73. http://www.onepetro.org/doi/10.2118/3543-PA

Bennion, B. 1999. "Formation Damage-The Impairment of the Invisible, By the Inevitable and Uncontrollable, Resulting In an Indeterminate Reduction of the Unquantifiable!" *Journal of Canadian Petroleum Technology* 38(02). http://www.onepetro.org/doi/10.2118/99-02-DA (March 7, 2016).

Bennion, D.B., and F.B. Thomas. 1994. "Underbalanced Drilling of Horizontal Wells: Does It Really Eliminate Formation Damage?" In Society of Petroleum Engineers.http://www.onepetro.org/doi/10.2118/27352-MS

Bishop, Simon R. 1997. "The Experimental Investigation of Formation Damage Due to the Induced Flocculation of Clays within a Sandstone Pore Structure by a High Salinity Brine." In Society of Petroleum Engineers. http://www.onepetro.org/doi/10.2118/38156-MS(March 7, 2016).

Boek, Edo S., Christopher Hall, and Philippe M. J. Tardy. 2011. "Deep Bed Filtration Modelling of Formation Damage Due to Particulate Invasion from Drilling Fluids." *Transport in Porous Media* 91(2): 479–508. http://link.springer.com/article/10.1007/s11242-011-9856-0

Byrne, M. 2012. "Formation Damage – Any Time, Any Place, Any Where." Presented at the Aberdeen Formation Evaluation Society AGM.

http://www.afes.org.uk/uploads/files/Formation%20Damage%20%E2%80%93%20Any%20Time.pdf.

Civan, Faruk, and PhD Civan. 2011. *Reservoir Formation Damage*. 2nd ed. Oxford: Elsevier Science.

Civan, F. 1995. "Modeling and Simulation of Formation Damage by Organic Deposition." *First international symposium in colloid chemistry in oil production: Asphaltenes and wax deposition, JSCOP*95: 26–29.

Delachambre, Y. 1966. "Contribution à L'étude de L'écoulement D'une Suspension à Travers Un Milieu Poreux et Du Mécanisme de La Filtration." Faculté des Sciences et Technologies.

Gruesbeck, C., and R.E. Collins. 1982. "Entrainment and Deposition of Fine Particles in Porous Media." *Society of Petroleum Engineers Journal* 22(06): 847–56.

http://www.onepetro.org/doi/10.2118/8430-PA.

Heertjes, PM, and CF Lerk. 1967. "The Functioning of Deep Bed Filters, Part II, The Filtration of Flocculated Suspensions." *Transactions of the Institution of Chemical Engineers* 45a: 138–45. http://archive.icheme.org/cgi-bin/somsid.cgi?record=1045&type=header.

Herzig, J. P., D. M. Leclerc, and P. Le. Goff. 1970. "Flow of Suspensions through Porous Media— Application to Deep Filtration." *Industrial & Engineering Chemistry* 62(5): 8–35. http://dx.doi.org/10.1021/ie50725a003

"ISO 14688-1:2002 - Geotechnical Investigation and Testing -- Identification and Classification of Soil -- Part 1: Identification and Description." *ISO*.

http://www.iso.org/iso/iso_catalogue/catalogue_tc/catalogue_detail.htm?csnumber=25260 (May 1, 2016).

Ives, K.J., and J. Gregory. 1966. "Surface Forces in Filtration." *Proc. Soc. Water Treat. Exam.* 15(2).

Khan, Hasan et al. 2016. "Comparative Study of Formation Damage due to Straining and Surface Deposition in Porous Media." In Society of Petroleum Engineers. http://www.onepetro.org/doi/10.2118/178930-MS

Khan, H.J. 2016. "Particulate straining in simple porous media." Digital Rocks Portal.

http://dx.doi.org/10.17612/ P7K01C

Maroudas, Alice, and Paul Eisenklam. 1965. "Clarification of Suspensions: A Study of Particle Deposition in Granular Media." *Chemical Engineering Science* 20(10): 867– 73.http://www.sciencedirect.com/science/article/pii/0009250965800835

Muecke, T.W. 1979. "Formation Fines and Factors Controlling Their Movement in Porous Media." *Journal of Petroleum Technology* 31(02): 144–50

http://www.onepetro.org/doi/10.2118/7007-PA

Patel, Mahesh Chandra, and Aaditya Singh. 2016. "Near Wellbore Damage and Types of Skin Depending on Mechanism of Damage." In Society of Petroleum Engineers. http://www.onepetro.org/doi/10.2118/179011-MS

Sakthivadivel, R. 1966. "Theory and Mechanism of Filtration of Non-Particleal Fines through a Porous Medium." In *HEL 15-5*, Coll. Eng., Univ. California, Berkeley.

Sharma, M. M., and Y. C. Yortsos. 1987a. "Fines Migration in Porous Media." *AIChE Journal* 33(10): 1654–62. http://onlinelibrary.wiley.com/doi/10.1002/aic.690331009/abstract

Sharma, M. M., and Y. C. Yortsos. 1987b. "Transport of Particulate Suspensions in Porous Media: Model Formulation." *AIChE Journal* 33(10): 1636–43.

http://onlinelibrary.wiley.com/doi/10.1002/aic.690331007/abstract

Stranneby, Dag. 2004. *Digital Signal Processing and Applications*. Elsevier.